Spring 5-15-2016

Plate Tectonics Initiation on Earth-Like Planets: Insights From Numerical and Theoretical Analysis of Convection-Induced Lithospheric Failure

Teresa Wong
Washington University in St. Louis

WASHINGTON UNIVERSITY IN ST. LOUIS

Department of Earth and Planetary Sciences

Dissertation Examination Committee:
Slava Solomatov, Chair
Ramanath Cowsik
William McKinnon
Philip Skemer
Douglas Wiens

Plate Tectonics Initiation on Earth-Like Planets: Insights From Numerical and Theoretical Analysis of Convection-Induced Lithospheric Failure

by

Teresa Wong

A dissertation presented to the
Graduate School of Arts and Sciences
of Washington University in
partial fulfillment of the
requirements for the degree
of Doctor of Philosophy

May 2016

Saint Louis, Missouri

Contents

List of Figures

List of Tables

Acknowledgements

First of all I would like to thank my advisor, Slava Solomatov, who made this work possible. I am deeply grateful for his guidance, patience, understanding, and encouragement. I also thank the members of my research committee, Bill McKinnon, Phil Skemer, and Doug Wiens, for meaningful discussions and keeping me on track in my graduate studies. My thanks also go to Ramanath Cowsik for taking part in my defense.

I would like to thank Washington University and the Department of Earth and Planetary Sciences for the financial support through fellowships, teaching and research assistantships. I also acknowledge NASA for travel grants to attend meetings.

I would not have survived graduate school without my fellow graduate students, especially the geophysics group. Special thanks to Kelsi Singer, Chris Orth, Aubreya Adams, and Marcia Holleran for their advice and friendship.

Last but not least I have to thank my family for their support and encouragement, keeping me physically and mentally healthy at a distance, and always reminding me to be open-minded.

Dedicated to my grandmother.

ABSTRACT OF THE DISSERTATION

Towards Understanding the Initiation of Plate Tectonics on Earth-Like Planets: Insights from Numerical and Theoretical Analysis of Convection-Induced Lithospheric Failure

by

Teresa Wong

Doctor of Philosophy in Earth and Planetary Sciences

Washington University in St. Louis, 2016

Professor Slava Solomatov, Chair

Plate tectonics is central to many aspects of the geology and evolution of terrestrial planets, yet it is only observed on the Earth while all other known planets are covered with a stagnant lithosphere. Plate motions on the Earth are mostly driven by the pull of subducting slabs, therefore understanding the initiation of subduction is crucial to understanding plate tectonics initiation. On a one-plate planet which lacks the forces due to plate motions, some other mechanisms will have to cause the first episode of subduction to mobilize the surface. Sublithospheric convection has been proposed as a possible mechanism that induce stresses in the lithosphere. The question is whether these stresses can initiate subduction. We develop scaling laws for the criterion of lithospheric failure from single-cell steady-state convection, which has more controlled flow and thus easier to analyze. We show that these scaling laws are applicable to time-dependent convection. We also investigate the time-dependent behavior of convection to understand the factors controlling the timing of lithospheric failure. We find that the variation in timing not only systematically depends on the physical parameters of the convecting mantle; for convective systems with the same set of parameters, small variations in initial conditions result in different structures of the lithosphere.

This changes the stresses in the lithosphere and gives rise to different times of lithospheric failure. This study suggests that it is important to address the question of when plate tectonics can initiate on a planet, in addition to finding favorable conditions for lithospheric failure. We extrapolate the scaling laws to planetary conditions to assess the feasibility of plate tectonics for terrestrial planets, and estimate whether plate tectonics can happen in reasonable planetary lifetimes.

Chapter 1

Introduction

The theory of plate tectonics has provided a framework to explain the geology of the Earth. Plate tectonics is currently understood as a style of convection involving the cold surface boundary layer, which manifests itself as rigid plates on the Earth (e.g., Bercovici et al. 2000; Schubert et al. 2001). However due to the high viscosity of this thermal boundary layer, questions remain on why this layer can participate in convective motions. Plate tectonics is an efficient heat transport mechanism which makes the evolution of the Earth distinct from all other known planetary bodies, on which convection is thought to be in the stagnant lid regime at present. This does not preclude the possibility of plate tectonics in the course of planetary evolution, as the surface expressions on Venus and Mars suggest large-scale deformation in the past that may be related to plate-tectonics processes (e.g., Turcotte 1993; Sleep 1994). The existence of plate tectonics on exoplanets is also of interest, motivated by various reasons including the possibility of finding an Earth-like planet and potential for habitability (e.g., Franck et al. 2000; Lammer et al. 2009).

To evaluate the conditions of a planet to have plate tectonics, we consider the problem of how subduction, which is thought to be the key process for plate motions on the Earth (e.g., Mueller and Phillips 1991), can initiate from a stagnant lid. Sublithospheric convection is one of the likely

mechanism to induce stresses in the lithosphere (often referred to as the lid), thus providing the driving forces to mobilize the lithosphere (e.g., Fowler 1985). In Chapter 2 we focus on developing scaling laws of stresses for subduction initiation. The origin of the lithospheric stresses comes from the lid structure resulting from sublithospheric convection, in particular the thermal thinning of the lid that generates shear stress large enough to overcome the yield stress of the lithosphere and cause large-scale failure. In this chapter we first describe the systematic analysis of convective systems with simple controlled flow to derive scaling laws for the magnitude of lithospheric stresses and the critical yield stress. Our analysis shows that initiation of subduction requires a very weak lithosphere, thus confirming the difficulty of starting plate tectonics on Earth and other planets. However, we find that the width of the convecting cells plays a larger role in subduction initiation than previously thought and speculate that, at least in principle, plate tectonics can start if long cells develop during planetary evolution.

As mantle convection systems are typically chaotic, their evolutionary pathways are random and a multitude of outcomes is possible. We explore this phenomenon and its implications for plate tectonics initiation in Chapter 3. We attempt to understand the variability of outcomes in terms of timing of subduction initiation, and provide a theoretical model to explain this timing. Our study demonstrates that the chaotic nature of time-dependent convection gives rise to different outcomes in terms of the timing of onset of plate tectonics. This highlights the importance of addressing the question of when would plate tectonics initiate, in addition to searching for favorable physical conditions.

Having established a theoretical basis for using scaling laws for subduction initiation, we seek to apply them to terrestrial planets in Chapter 4. To do so we test the applicability of the scaling laws derived from single-cell simulations in Chapter 2 to more complicated time-dependent

convection systems. Noting that there are currently many models of subduction initiation for the Earth, they will be briefly reviewed in Chapter 4. We also discuss the implications of lithospheric stress and critical yield stress estimation for the hypothesis of past episodes of plate tectonics on Venus and Mars, the prevalent surface deformation on Mercury, and predictions for exoplanets. We show that our scaling laws are applicable to more realistic multi-cell time-dependent convective systems. We extrapolate these scaling laws to terrestrial planets to estimate the criterion of lithospheric failure.

Chapter 2

Towards scaling laws for subduction initiation on terrestrial planets: Constraints from two-dimensional steady-state convection simulations

T. Wong and V. S. Solomatov

An edited version of this chapter was published by SpringerOpen.

Wong, T. and Solomatov, V. (2015). Towards scaling laws for subduction initiation on terrestrial planets: constraints from two-dimensional steady-state convection simulations. *Progress in Earth and Planetary Science, 2(1):18*, doi:10.1186/s40645-015-0041-x.

Abstract

The strongly temperature-dependent viscosity of rocks leads to the formation of nearly rigid lithospheric plates. Previous studies showed that a very low yield stress might be necessary to weaken and mobilize the plates, for example, due to water. However the magnitude of the yield stress remains poorly understood. While the convective stresses below the lithosphere are relatively small,

sublithospheric convection can induce large stresses in the lithosphere indirectly, through thermal thinning of the lithosphere. The magnitude of the thermal thinning, the stresses associated with it and the critical yield stress to initiate subduction depend on several factors including the viscosity law, the Rayleigh number and the aspect ratio of the convective cells. We conduct a systematic numerical analysis of lithospheric stresses and other convective parameters for single steady-state convection cells. Such cells can be considered as part of a multi-cell, time-dependent convective system. This allows us a better control of convective solutions and a relatively simple scaling analysis. We find that subduction initiation depends much stronger on the aspect ratio than in previous studies and speculate that plate tectonics initiation may not necessarily require significant weakening and can, at least in principle, start if a sufficiently long cell develops during planetary evolution.

2.1 Introduction

Plate tectonics is central to many aspects of the geology and evolution of terrestrial planets. While Earth is the only planet where plate tectonics is observed, its driving mechanism and timing of initiation are still poorly understood. Subduction is thought to be the fundamental process for plate tectonics initiation, because the slab pull of subducting slab contributes most to the forces that drive plate movements. On the Earth, initiation of subduction is greatly facilitated by tectonic forces associated with plate motions *already occurring elsewhere* (Mueller and Phillips 1991; Hall et al. 2003)). Various models for subduction initiation has been proposed (e.g., McKenzie 1977; Turcotte 1977; Ogawa 1990; Mueller and Phillips 1991; Kemp and Stevenson 1996; Toth and Gurnis 1998; Stern 2004; Solomatov 2004b; Ueda et al. 2008; Nikolaeva et al. 2010), many of which involve

existing plate boundaries or weak zones. Incipient subduction zones are often found near transform faults or fracture zones because of their physical weakness (e.g., Mueller and Phillips 1991; Gurnis et al. 2004).

On one-plate planets such as Venus and Mars, the absence of plate tectonics is likely to be due to the difficulty of subduction initiation in the absence of forces due to plate motions. In other words the problem of plate tectonics initiation can be viewed as the problem of the very first occurrence of subduction. Due to the high sensitivity of viscosity to temperature, the lithosphere acts as the cold rigid thermal boundary layer that has a very high strength. On these planets, mantle convection is likely to be in the stagnant lid regime (e.g., Morris and Canright 1984; Fowler 1985; Solomatov 1995). One possible mechanism for the very first episode of subduction is due to the lithospheric stresses generated by mantle convection (Ogawa 1990; Fowler and O'Brien 2003; Solomatov 2004b). The magnitude of these stresses is relatively small compared to the lithospheric strength suggested by laboratory and field observations (e.g., Kohlstedt et al. 1995; Gurnis et al. 2004) and thus it is usually believed that to initiate subduction some weakening mechanisms must be present in the lithosphere.

Much effort has been devoted to understand the weakening mechanisms of the lithosphere. Several studies showed that the frictional shear stress resisting subduction at transform faults and fracture zones have to be less than 10 MPa for subduction to occur (Toth and Gurnis 1998; Hall et al. 2003; Gurnis et al. 2004). Stress drop estimates from earthquakes also indicate that fault strength may be $\sim$10 MPa (Kanamori 1994; Kanamori and Brodsky 2004). Models are able to describe global reduction in the lithospheric strength, as well as localized weak zones such that plate-like features can be generated from mantle convection in a self-consistent manner (e.g., Trompert and Hansen 1998; Moresi and Solomatov 1998; Tackley 2000b; Bercovici et al. 2001; Branlund et al.

2001; Regenauer-Lieb et al. 2001; Regenauer-Lieb and Kohl 2003; Regenauer-Lieb et al. 2006; Korenaga 2007; Landuyt et al. 2008). Various approaches have been used to deal with the creation of weak zones (Bercovici et al. 2001; Bercovici and Ricard 2005; Landuyt et al. 2008; Branlund et al. 2001; Regenauer-Lieb and Kohl 2003). The two-phase damage theory with a grain-size dependent rheology was developed to explain the formation of weak plate boundaries and track the evolution of deformation (e.g., Bercovici and Ricard 2005; Landuyt et al. 2008; Bercovici and Ricard 2012). Some studies suggested that water might play an important role in the localization of deformation (Regenauer-Lieb et al. 2001; Regenauer-Lieb and Kohl 2003; Regenauer-Lieb et al. 2006). Water also weakens the lithosphere by lowering the activation energy (Regenauer-Lieb et al. 2001; Regenauer-Lieb and Yuen 2004; Regenauer-Lieb et al. 2006), and increasing the pore fluid pressure (Kohlstedt et al. 1995).

One approach to quantify the weakening of lithosphere is to set a yield value to the rheology of the lithosphere to simulate brittle behaviour (Fowler 1993; Trompert and Hansen 1998; Moresi and Solomatov 1998; Richards et al. 2001; Tackley 2000a,b; Fowler and O'Brien 2003; Solomatov 2004b; Stein et al. 2004; O'Neill et al. 2007; Stein and Hansen 2008). The yield stress can be regarded as a simplification of mechanisms that describe the strength of the lithosphere. Convection with yield stress is usually categorized into 3 regimes: mobile lid regime, transitional regime with some episodic failure, and stagnant lid regime (Moresi and Solomatov 1998; Tackley 2000a; Stein et al. 2004). Stein and Hansen (2008) further subdivided the transitional regime into episodically mobile and stable plate mobilization regimes. To access the conditions of a planet to have plate tectonics, some researchers presented regime diagrams in terms of Rayleigh number, viscosity contrast, and yield stress (e.g., Stein et al. 2004; O'Neill and Lenardic 2007).

A number of studies attempted to derive scaling relations for convective stresses and yield

stress to extrapolate to planetary conditions (e.g., Moresi and Solomatov 1998; Fowler and O'Brien 2003; Solomatov 2004b,a; O'Neill et al. 2007; Valencia and O'Connell 2009; Korenaga 2010b; van Heck and Tackley 2011; Stamenkovic and Breuer 2014). Yet the accurate description of these convection-induced stresses inside the lithosphere and thus the yield stress is lacking.

This study seeks to understand the stress distribution of the steady-state convecting cell with respect to various convective parameters using the pseudoplastic rheology as a first step. The goal of this study is to find a scaling law for the lithospheric stress (hereafter referred as lid stress) and the critical yield stress, which is the highest yield value at which the stagnant lid could be mobilized. Note that an alternative and, perhaps, more intuitive approach would be to assume that the yield stress is known and to try to figure out under what dynamic conditions it can be reached. However, (a) the "normal" yield stress is so high that it is nearly impossible to reach and (b) given the uncertainties in the weakening mechanisms and thus the actual magnitude of the yield stress, it should be treated as an unknown.

In this study we first examine the stress structure in steady-state stagnant lid convection, and explore scaling relationships between convective parameters especially in relation to aspect ratio to develop a scaling theory for lid stress and critical yield stress. We then compare the theoretical scaling laws with numerical results. In addition we investigate the accuracy of the Frank-Kamenetskii approximation for modeling the initiation of plate tectonics.

2.2 Rheology

Viscous creep governs the flow in the mantle as it has high temperatures and low stresses. It can be described by a constitutive relation (Hirth and Kohlstedt 2003), which is an Arrhenius

function of temperature T, activation energy E, pressure P, and activation volume V with power law dependences on stress τ (second invariant of stress tensor), grain size d, water fugacity $f_{\mathrm{H_2O}}$, and an exponential function of melt fraction ϕ:

$$\eta = A\tau^{1-n} d^m f_{H_2O}^{-r} \exp(-\alpha\phi) \exp\left(\frac{E+PV}{RT}\right), \tag{2.1}$$

where A and α are constants, R is the gas constant, and m, n, r are exponents for grain size, stress, and water fugacity respectively. Depending on the temperature, grain size, stress, pressure, and composition, the dominating deformation mechanism in the mantle would be different (Karato and Wu 1993; Karato et al. 1995; Hirth and Kohlstedt 2003). In the lithosphere, the major factor controlling the viscosity is temperature. Thus the viscosity function to investigate subduction initiation is often written as:

$$\eta = A' \exp\left(\frac{E}{RT}\right). \tag{2.2}$$

2.2.1 Frank-Kamenetskii approximation

Many numerical studies used use a relatively low viscosity contrast to observe plate behavior, which has limited applications to realistic planetary situations. Moresi and Solomatov (1998) investigated the convective regimes with viscosity contrast ranging from 3×10^4 to 3×10^7, and in Tackley (2000b) the viscosity contrast was limited to 10^4, whereas Richards et al. (2001) and Stein and Hansen (2008) used viscosity contrast on the order of 10^5. The viscosity contrast across the terrestrial lithosphere is many orders of magnitude higher.

The low viscosity contrast is used because high viscosity contrasts are difficult to treat in numerical calculations (Moresi and Solomatov 1995). Thus the Arrhenius function is often approxi-

mated by the Frank-Kamenetskii function, which reduces the viscosity contrast by many orders of magnitude compared to Arrhenius viscosity function. This makes the problem of convection with strongly temperature-dependent viscosity more computationally tractable.

Frank-Kamenetskii approximation originated from the combustion theory. Frank-Kamenetskii pointed out that since the activation energy E is large, we can consider the rate of reaction only in a narrow range of temperature around the combustion temperature (Frank-Kamenetskii 1969)). The equation for the rate of reaction is similar to the strain rate in the constitutive relations, which also has an Arrhenius form $\exp(-E/RT)$. Since convection mostly takes place in the interior of the cell where the temperature is close to the interior temperature T_i, we use the same approximation by expanding the exponent E/RT in the Arrhenius form so that the viscosity can be expressed as an exponential function of temperature only:

$$\eta = B\exp(-\gamma T), \tag{2.3}$$

where B and γ are constants. In the interior:

$$\eta_{i,\mathrm{Arr}} = \eta_{i,\mathrm{exp}}, \tag{2.4}$$

$$\left(\frac{d\eta_{i,\mathrm{Arr}}}{dT}\right)_{T=T_i} = \left(\frac{d\eta_{i,\mathrm{exp}}}{dT}\right)_{T=T_i}, \tag{2.5}$$

where η_{Arr} and η_{exp} are the interior viscosities of the Arrhenius function and that of Eq. 2.3 (hereafter referred as exponential viscosity) respectively. Eqs. 2.4 and 2.5 give γ in terms of

activation energy and interior temperature:

$$\gamma = \frac{E}{RT_i^2}. \tag{2.6}$$

This method of expanding the terms in the exponent preserves the interior viscosity and the change of viscosity with temperature close to T_i, where convection actively takes place. Some studies expanded the terms inside the exponents differently (e.g., King 2009). However, it is important to use Eq. 2.4 and 2.5 to ensure the asymptotic accuracy of Frank-Kamenetskii approximation (Morris 1982; Morris and Canright 1984; Fowler 1985; Frank-Kamenetskii 1969).

Frank-Kamenetskii approximation was shown to be sufficiently accurate for the interior of the convective layer with large viscosity contrast (Solomatov and Moresi 1996; Ratcliff et al. 1997; Reese et al. 1999). Recent studies have examined convection with Arrhenius rheology and suggested slightly different scaling laws compared to convection with Frank-Kamenetskii viscosity (Korenaga 2009; Stein and Hansen 2013). Here we assess the accuracy of the Frank-Kamenetskii approximation in predicting the values of critical yield stress.

2.2.2 Pseudoplastic rheology and plastic yielding

The brittle behavior of the lithosphere can be simplified with a viscoplastic rheology that causes yielding when the convective stresses exceed a plastic yield stress τ_y (Moresi and Solomatov 1998; Trompert and Hansen 1998; Tackley 2000a; Fowler and O'Brien 2003). The yield stress can be defined by Byerlee's law (Byerlee 1978):

$$\tau_y = \tau_0 + \mu\rho g z, \tag{2.7}$$

where τ_0 is the yield stress at the zero hydrostatic pressure, μ is the frictional coefficient, and $\rho g z$ is the hydrostatic pressure. Viscous deformation occurs according to Eq. 2.3 when stresses are less than the yield stress. Above the yield stress, the deformation follows a plastic flow law defined by a non-linear effective viscosity:

$$\eta_{\text{eff}} = \frac{\tau_y}{\dot{e}}, \tag{2.8}$$

where $\dot{e}$ is the second invariant of the strain rate tensor. The yield stress defines a change on deformation mechanism based on the second invariant of the deviatoric stress tensor, which corresponds to the Von Mises yield criterion. In this study we consider two types of yield stress: a constant yield stress τ_y, or a depth-dependent yield stress with a constant gradient τ_y'.

2.3 Formulation of the problem

2.3.1 Equations of thermal convection

The equations of thermal convection of an incompressible fluid in Boussinesq approximation and infinite Prandtl number are:

$$\frac{\partial u_i}{\partial x_i} = 0, \tag{2.9}$$

$$\alpha \rho g_i T' - \frac{\partial p'}{\partial x_i} + \frac{\partial \tau_{ij}}{\partial x_j} = 0, \tag{2.10}$$

$$\frac{\partial T'}{\partial t} + u_i \frac{\partial T'}{\partial x_i} = \kappa \frac{\partial^2 T'}{\partial x_i^2}, \tag{2.11}$$

where ρ is density, p' and T' are pressure and temperature perturbations, g_i is the gravity vector, α is the thermal expansivity, $\kappa = \frac{k}{\rho c_p}$ is the thermal diffusivity, k is the thermal conductivity, and c_p is the isobaric specific heat. τ represents the elements of the stress tensor according to the following

equation:

$$\tau_{ij} = \eta \left(\frac{\partial u_i}{\partial x_j} + \frac{\partial u_j}{\partial x_i} \right), \tag{2.12}$$

where i, j, are indices of the coordinate axes.

The boundary conditions are as follows. For a cell with only base heating, the top and bottom surfaces are isothermal. The temperature of the top surface T_0 and that of the bottom surface T_1. The temperature difference is $\Delta T = T_1 - T_0$. The vertical boundaries are thermally insulated. All surfaces are free-slip. The velocity normal to a cell boundary is zero.

2.3.2 Non-dimensionalization

The above equations are non-dimensionalized as follows:

$$\bar{x_i} = \frac{x_i}{d},\ \bar{u_i} = u_i \frac{d}{\kappa},\ \bar{\eta} = \frac{\eta}{\eta_1},\ \bar{\tau} = \tau \frac{d^2}{\kappa \eta_1},\ \bar{t} = t \frac{\kappa}{d^2},\ \bar{T} = \frac{T}{\Delta T}, \tag{2.13}$$

where d is the layer depth, t is time, η_1 is the reference viscosity (at the bottom of the convective layer), and ΔT is the temperature drop across the layer. The Rayleigh number can then be used to characterize the system:

$$Ra = \frac{\alpha \rho g \Delta T d^3}{\kappa \eta_1}. \tag{2.14}$$

The Arrhenius viscosity is non-dimensionalized as:

$$\bar{E} = \frac{E}{R \Delta T}, \tag{2.15}$$

$$\bar{\eta} = \eta_{r,\mathrm{Arr}} \exp \frac{\bar{E}}{\bar{T_0} + \bar{T'}}, \tag{2.16}$$

while the dimensionless exponential viscosity is:

$$\bar{\eta} = \eta_{r,\exp} \exp(-\theta \bar{T}'), \tag{2.17}$$

where the pre-factors $\eta_{r,\mathrm{Arr}}$ and $\eta_{r,\exp}$ are chosen to ensure that the viscosity is equal to unity at $\bar{T}' = 1$ and the Frank-Kamenetskii parameter θ is the non-dimensionalized form of the constant γ (Eq. 2.6):

$$\theta = \gamma \Delta T. \tag{2.18}$$

In this case, the viscosity contrast is characterized by only one parameter (θ):

$$\Delta\eta = e^{\theta}, \tag{2.19}$$

The non-dimensional yield stress is:

$$\bar{\tau_y} = \bar{\tau_0} + \bar{\tau'}_y \bar{z}, \tag{2.20}$$

where

$$\bar{\tau_0} = \frac{d^2}{\kappa \eta_1} \tau_0 \tag{2.21}$$

is the non-dimensional yield stress at the surface and

$$\bar{\tau'}_y = \frac{\rho g d^3}{\kappa \eta_1} \mu \tag{2.22}$$

is the non-dimensional yield stress gradient. The dimensionless pseudoplastic viscosity is:

$$\bar{\eta}_{\text{eff}} = \frac{\bar{\tau}_y}{\bar{\dot{e}}},\ \bar{\dot{e}} = \frac{d^2}{\kappa}\dot{e}. \tag{2.23}$$

In the following discussion all parameters are assumed to be non-dimensionalized and the bar sign will be dropped. The non-dimensional forms of Eqs. 2.9-2.11 are:

$$\frac{\partial u_i}{\partial x_i} = 0, \tag{2.24}$$

$$RaT'\mathbf{e}_i - \frac{\partial p'}{\partial x_i} + \frac{\partial \tau_{ij}}{\partial x_j} = 0, \tag{2.25}$$

$$\frac{\partial T'}{\partial t} + u_i\frac{\partial T'}{\partial x_i} = \frac{\partial^2 T'}{\partial x_i^2}. \tag{2.26}$$

where $\mathbf{e}_i$ is a unit vector in the direction of gravity.

2.3.3 Matching Arrhenius viscosity and exponential viscosity in non-dimensional form

To compare the two viscosity laws, the Arrhenius viscosity and the exponential viscosity are matched according to Eqs. 2.4 and 2.5:

$$\eta_{\text{r,Arr}} \exp\frac{E}{T_i + T_0} = \eta_{\text{r,exp}} \exp\left(-\theta T_i\right), \tag{2.27}$$

$$\frac{E}{(T_i + T_0)^2}\eta_{\text{r,Arr}} \exp\frac{E}{T_i + T_0} = \theta\eta_{\text{r,exp}} \exp\left(-\theta T_i\right). \tag{2.28}$$

Eqs. 2.27 and 2.28 would yield:

$$\theta = \frac{E}{(T_i + T_0)^2}. \tag{2.29}$$

T_i differs from the bottom temperature T_1 by a rheological temperature difference $\Delta T_{\rm rh}$, which is on the order of θ^{-1}.

Equation 2.29 shows that there are various combinations of E and T_0 that would give the same θ, and they would result in different Arrhenius viscosity contrasts:

$$\Delta\eta_{\rm Arr} = \exp \frac{ET_i}{T_0(T_i + T_0)}. \tag{2.30}$$

Thus the ratio of Arrhenius viscosity contrast to exponential viscosity contrast $\exp\theta$, is:

$$\frac{\Delta\eta_{\rm Arr}}{\exp(\theta)} = \exp \frac{ET_i}{T_0(T_i + T_0)^2}. \tag{2.31}$$

2.4 Steady-state convection

We use the finite element code CITCOM (Moresi and Solomatov 1995)) to simulate convection in a $64a \times 64$ box, where a is the aspect ratio. Several high viscosity cases were ran with $128a \times 128$ resolution for more accurate results. All cases were run until they reached a steady state at which the rate of heat loss is equal to that of heat production. We consider the range of parameters in which convection is in the stagnant lid regime (Solomatov 1995).

The structure of a steady-state convection cell is shown in Fig. 2.1. Due to the temperature-dependent viscosity, the top part of a convective cell forms a stagnant lid and convection only penetrates into the lid by length of δ_{rh} – the rheological layer thickness (e.g., Solomatov 1995). A cold rigid lid, which is often defined by an isotherm, is naturally developed in the top part of the cell sloping downward to the downwelling end. The stress field (Fig. 2.1, right) shows a stress boundary layer near the surface. This is consistent with the analytical solutions of (Fowler 1985).

To compare the stresses in exponential and Arrhenius viscosity, we choose a range of T_0 and calculate their corresponding E that gives the same θ according to Eq. 2.29 with $T_i \approx 1$.

2.4.1 Aspect ratio

The horizontally averaged profiles (Fig. 2.2) show that the lid thickness slightly depend on the aspect ratio of the convective cell but the bulk of the temperature and viscosity profile does not vary much with the aspect ratio. However the stress profile in small aspect ratio cells ($a = 0.25$) is distinctly different from that in larger cells (a = 0.5 to 1).

This difference is more apparent in the 2-D plots (Fig. 2.3). In wider cells the layer with highest stress (red) is approximately symmetric along the half-width of the cell, increasing in depth towards both edges and greater towards the downwelling edge. Below the surface stress boundary layer, the stresses in the middle of the lid are highest as they are not affected by the free-slip boundary conditions at the vertical edges. Although surface stress boundary layer is obvious in horizontally averaged stress profiles, the 2-D stress fields reveal that the surface stress are not always greater than that at depth. Figure 2.3 shows that at mid-width, it is possible that the surface stresses are lower than the interior. The high stress region (orange to lime) roughly correspond to the cold lid shown in the temperature distribution, both having slopes towards the downwelling edge. In the narrowest cell however, this high stress slope deviates from the thermal lid slope. There is a high stress ”core” within the lid where the magnitude of stresses is close to that of the surface stress boundary layer. This implies that steady-state convection in small aspect ratios may be in another regime of plastic failure where the interior stresses reach the yield stress first, such that the plastic zone could initiate at depth while the surface may or may not be plastic, depending on the yield stress.

For cases with high viscosity contrasts and larger aspect ratios, convection is localized to a small part of the cell, or there could be multiple convective cells (Fig. 2.4). These cases might belong to the subcritical convective regime (Solomatov 2012), which has a different behaviour from supercritical convection and therefore not in our scope of study. To stabilize one-cell flow, smaller aspect ratio cases are considered to investigate the dependence of critical yield stress on aspect ratio.

2.4.2 Rayleigh number

Increasing Ra reduces the lid thickness as well as the lid slope (Fig. 2.5). The stresses are larger with higher Ra, as is expected with more vigorous convection.

2.4.3 Viscosity contrast

The effects of viscosity contrast on the interior profile are illustrated in the plots in Fig. 2.6. The conductive lid becomes thicker and the interior temperature is closer with the bottom temperature with increasing θ. In the stagnant lid regime ($\theta > 10$) the stress boundary layer near the surface is more pronounced than in the transitional regime.

The interior viscosity, temperature, and stress for Arrhenius viscosity and exponential viscosity are close. We investigate a range of different Arrhenius viscosity values by varying T_0, noting that at $T_0 = 2.0$ is a rather high surface temperature. As T_0 decreases, the difference in viscosity contrasts calculated by the two viscosity laws becomes larger. However the temperature and the stress profiles are similar, as shown in the horizontally averaged profiles in Fig. 2.7. There is only a slight decrease in thickness of the stress boundary layer as the Arrhenius viscosity contrast increases. The 2-D stress distributions in Fig. 2.8 and 2.9 reflect the small differences in the stress

distribution as viscosity contrast increases, both in exponential viscosity and Arrhenius viscosity. This is contrary to the findings of (Stein and Hansen 2013), which observed a distinctly thinner lid in Arrhenius viscosity and slightly different temperature and viscosity profiles. The small difference that we observe may affect the scaling laws for subduction. The vertical variation in stresses at the downwelling edge may be particularly important. Although the lid thickness is about the same, the contrast in stresses at $x = a$ seems to be greater at low T_0 or high viscosity contrast (Fig. 2.9). Since subduction occurs at the downwelling edge, this may influence the scaling of yield stress.

2.5 Lid stress scaling theory

Fowler (1985) obtained a polynomial expression for the stress in the lid below the surface stress boundary layer in large lid slope approximation, which allows a comparatively simple scaling relation for stress. In order to solve the equations of convection, Fowler took Ra and θ to be asymptotically large, and assumed the magnitude of lid slope to be either on the order of lid thickness or rheological sublayer thickness. For the Earth and some smaller terrestrial planets as well as most numerical simulations, Ra may not be as high as the asymptotic theory require and thus some other theory may be needed for lid stress scaling. Moreover, as we find in this study, the lid slope does not follow either of these two end-member cases and thus needs to be scaled based on numerical simulations.

Fowler also found that the interior flow can be uncoupled from the rheological sublayer, which makes the problem setup akin to a viscous lid gravitationally sliding along a slope. We can therefore estimate the shear stress in the rigid lid τ_{lid} by considering the force balance on the lid (Fig.

2.1):

$$\frac{d\tau}{dy} = \Delta\rho g_x. \tag{2.32}$$

For density changes due to temperature variations, the lid stress can be integrated from Eq. 2.32:

$$\tau_{\text{lid}} = -\alpha\rho_0 \frac{dT}{dy} g \sin\lambda \frac{y^2}{2} + \tau_i, \tag{2.33}$$

where τ_i is the stress at the interior temperature T_i.

There are two assumptions that allow us to simplify Eq. 2.33. The first is that τ_i is negligible since $\tau_i \ll \tau_{\text{lid}}$. The second is the small lid slope approximation. For small λ, $\sin(\lambda)$ is approximately equal to λ. The non-dimensional form of Eq. 2.33 becomes:

$$\tau_{\text{lid}} = -\text{Ra}\frac{dT}{dy}\frac{y^2}{2}\lambda. \tag{2.34}$$

Thus the lid stress is determined by Ra, dT/dy, λ, and y, which will be defined in the following discussion. This scaling is similar to that obtained from the analytical solutions of Fowler (1985).

2.5.1 Lid base temperature

The lid base is often defined by an isotherm:

$$T_L = T_i - C\theta^{-1} \tag{2.35}$$

where C is a constant. We determine the lid base from velocity profile (Solomatov and Moresi 2000) to find the constant C. We first find the greatest velocity gradient at a specific distance x

from the upwelling edge of the cell. This velocity gradient is then extended to the depth at which velocity is zero, as shown in Fig. 2.10. This depth defines the lid thickness. This process is repeated for all x (from 0 to a) to obtain the shape of the lid base across the convecting cell. This velocity gradient-defined lid base is then used to find the thermal lid base defined by Eq. 2.35. The interior temperature T_i is found by averaging the temperature in the middle part of the interior to exclude the boundary effects. The constant C is determined by matching the lid thickness at mid-width ($x = 0.5a$) given by T_L and that defined by the velocity gradient (Fig. 2.11). We choose the value at mid-width because in most cases the two lid bases are closest around the middle of the cell for a large lateral extent. In some cases, especially for narrower cells, the temperature lid base and the velocity lid base may not match, so the mid-width serves as a reference point for consistency in defining the lid base.

Eq. 2.35 allows us to determine the rheological temperature difference $\Delta T_{\mathrm{rh}} = T_i - T_L = C\theta^{-1}$. It varies with Ra, θ, and aspect ratio, and the scaling exponents are summarized in Table 2.1.

2.5.2 Lid slope, lid thickness and plume slope

Gravitational sliding requires a downward dipping slope λ as indicated in Eq. 2.34. In larger aspect ratio cells, although the lid thickness varies horizontally, the lid slope is approximately constant in the middle portion of the cell. This is different for smaller cells, where the lid base could be some function of x instead of a straight line (Fig. 2.12). For example, Fowler suggests that the lid base varies with $x^{0.4}$ (Fowler 1985). For consistency in our scaling analysis, the lid slope is taken to be the slope of the thermal lid base at mid-width.

To check whether the lid slope scales with lid thickness or rheological sublayer thickness

Fowler (1985), we look at the vertical drop δ_{x} (Fig. 2.1) and define the lid slope as δ_{x}/a. If the lid slope scales with the lid thickness, then $\delta_{\mathrm{x}} \sim \delta_{\mathrm{lid}} \sim \mathrm{Nu}^{-1}$, and thus

$$\delta_{\mathrm{x}}/\delta_{\mathrm{lid}} \sim \mathrm{Nu}\delta_{\mathrm{x}} \sim \mathrm{constant}. \tag{2.36}$$

If the lid slope scales with δ_{rh}, then $\delta_{\mathrm{x}} \sim \delta_{\mathrm{rh}}$. As $\delta_{\mathrm{rh}}/\delta_{\mathrm{lid}} \sim \theta^{-1}$, thus $\delta_{\mathrm{x}}/\delta_{\mathrm{lid}} \sim \theta^{-1}$, or

$$\theta\delta_{\mathrm{x}}/\delta_{\mathrm{lid}} \sim \mathrm{Nu}\delta_{\mathrm{x}}\theta \sim \mathrm{constant}. \tag{2.37}$$

We plot $\mathrm{Nu}\delta_{\mathrm{x}}$ and $\mathrm{Nu}\delta_{\mathrm{x}}\theta$ in Fig. 2.13. Neither combination remains constant with θ, with $\mathrm{Nu}\delta_{\mathrm{x}}$ increases with θ and $\mathrm{Nu}\delta_{\mathrm{x}}\theta$ decreases with θ. This suggests that the lid slope is somewhere in between these two extreme cases. Therefore in deriving the scaling laws for stresses, we need to determine the dependence of lid slope on various convective parameters (Table 2.1).

We can limit the aspect ratio of a sub-cell in a multi-cell system by using theoretical constraints based on the end member cases for the magnitude of lid slope in a single-cell convective box (Fig 2.14). The large lid slope case ($\lambda \sim \delta_{\mathrm{lid}}$) prohibits the lid slope to exceed $2\delta_{\mathrm{lid},1/2}/a$, where $\delta_{\mathrm{lid},1/2}$ is the lid thickness taken at mid-width, and the small lid slope case ($\lambda \sim \delta_{\mathrm{rh}}$) dictates that the lid slope should be greater than $2\delta_{\mathrm{rh}}/a$. These theoretical constraints are based on the assumption that both δ_{lid} and δ_{rh} are small enough such that the lid slope can be approximated by these ratios. We compare the lid slopes in our numerical results and the values obtained by these two limits in the single-cell steady-state solutions in Fig. 2.15. We find that the numerically obtained lid slopes are slightly smaller than the lower theoretical limit given by the rheological sublayer ($\lambda \approx 2\delta_{\mathrm{rh}}/a$). Therefore the theoretical constraints seem to support the small lid slope approximation, so the

aspect ratio is limited by $a \approx 2\delta_{\mathrm{rh}}/\lambda$. Since the λ from δ_{rh} is still larger than numerically obtained λ, the aspect ratios could be smaller for theoretical constraints to hold.

The slope of the sinking plume may be another cause of gravitational sliding (Fig. 2.11). The errors of linear regression for the power law coefficient of various parameters with the plume slope are significant that it is difficult to find a scaling law for the plume slope (Table 2.1). Therefore we cannot conclude how much the plume slope contributes to the stresses.

2.5.3 Thermal gradient

The temperature is approximately a linear function of depth and the thermal gradient in the lid is about constant with depth. At mid-width ($x = 0.5a$) it is approximately equal to the Nusselt number, which is the non-dimensional horizontally averaged surface temperature gradient. Since we are looking at temperature changes from the interior to the bottom of the lid which includes the rheological sublayer, we also check the thermal gradient in the rheological sublayer $\Delta T_{\mathrm{rh}}/\delta_{\mathrm{rh}}$ to note any difference in the scaling relations. As before, we choose the values $\Delta T_{\mathrm{rh}}/\delta_{\mathrm{rh}}$ at the mid-width to exclude boundary effects for scaling purposes.

In previous theories, $\Delta T_{\mathrm{rh}}/\Delta T \sim \theta^{-1}$ and $\delta_{\mathrm{rh}}/\delta_{\mathrm{lid}} \sim \theta^{-1}$. The determination of C follows the description in the previous section on lid base temperature, and it is found to be dependent on aspect ratio and θ. Therefore $\Delta T_{\mathrm{rh}}/\Delta T$ and $\delta_{\mathrm{rh}}/\delta_{\mathrm{lid}}$ will also have a dependence on a and θ, and their scaling relations are summarized in Table 2.1.

2.5.4 Stress scaling

Eq. 2.34 can now be expressed in a non-dimensional form with the definitions of various parameters in the previous discussion. At the bottom of the lid at δ_{rh} from the interior, where the

temperature difference is $\Delta T_{\rm rh}$, the stresses are:

$$\tau_{\rm lid} \sim {\rm Ra}\frac{\Delta T_{\rm rh}}{\delta_{\rm rh}}\lambda y^2. \tag{2.38}$$

Further into the lid, the non-dimensional temperature gradient is the Nusselt number. Therefore Eq. 2.34 can be alternatively scaled as:

$$\tau_{\rm lid} \sim {\rm RaNu}\lambda y^2. \tag{2.39}$$

As shown in Fig. 2.10, there is a slight difference in the thermal gradient in the lid and in the rheological sublayer, therefore Eqs. 2.38 and 2.39 may result in slightly different scaling exponents. We check both scaling relations to see whether the stresses at the lid base and those in the lid can be scaled similarly.

We plot the stress profile according to Eqs. 2.38 and 2.39 and compare with that from numerical solutions (Fig. 2.16). The prefactor of the stress as a function of y calculated from the thermal gradient in the rheological sublayer ($T_{\rm rh}/\delta_{\rm rh}$) is 5.9×10^6, whereas that from the Nusselt number is 9.6×10^6. This demonstrates that the theoretical stress profiles match fairly closely with the numerical one, and the best fit can be obtained with some small adjustments in the coefficient.

All the above parameters depend on Ra, aspect ratio a and θ, thus they can be expressed as ${\rm Ra}^\beta a^\zeta \theta^\alpha$ where β, ζ, and α are scaling exponents. The results are summarized in Table 2.2.

2.6 Convection with yield stress

We use the steady-state solutions as the starting point before imposing a yield stress to simulate plastic yielding. For the yield stress gradient, a small cohesion term (surface yield stress) was introduced to stabilize the solution.

2.6.1 Regimes of convection with constant yield stress or constant yield stress gradient

When a yield stress is present, the regions with stresses that reach the yield value would have an approximately constant stress close to τ_y. These plastic zones develop first at the corners of the cell where the stresses are highest. As τ_y decreases, the plastic zones extend both in depth and horizontally, narrowing the width of the high viscosity part of the lid (Fig. 2.17). If yield stress is too high, the depth of the plastic zone is small or the plastic zone is entirely absent, thus the stagnant lid does not fail. If the yield stress is sufficiently low, the plastic zone extends sufficiently deep so that the stagnant lid is mobilized.

We examine the stress and viscosity profiles at various locations x to see how they change in the presence of a yield stress (Fig. 2.18 and 2.19). At high yield stress or high yield stress gradient, the plastic zone only occurs at shallow depths and the bulk of the stress and viscosity profiles are unaltered from the stagnant lid state. The plastic zone extends deeper as the yield stress or yield stress gradient decreases. As the yield stress approaches the critical value, a small change in yield stress induces a change in plastic depth that is comparable to the change caused by an order of magnitude change in yield stress when it is far from critical. Although subduction does not occur, this implies a change in convection regime from stagnant lid to some sort of transitional regime.

In this transitional regime, the yield stress slightly changes the interior dynamics as can be

seen in various convective parameters of the interior region of the cell. The yield stress increases the lid slope whereas the lid thickness remains approximately the same. When the yield stress is slightly above the critical value, these changes caused by yield stress are negligible and convection remains in the stagnant lid regime. Therefore in deriving the critical yield stress scalings, we refer to the steady-state structure that has a yield stress just above the critical value, so that the scaling relations for various convective parameters (Table 2.1) from steady-state stagnant lid convection can still be used.

2.6.2 Time evolution of lid weakening and failure

When the lid fails, the surface velocity continuously increases and overturn occurs (Fig. 2.20). Figure 2.21 shows the time sequence of stress structures before and during failure. When the surface velocity is still low compared to the bottom velocity (Fig. 2.20, left), the variation in stress structure is not obvious. It is not until the velocity begins to increase drastically that the plastic yield zones from the two corners start to connect in the middle of the cell to form a plastic lid. The weak lid then becomes unstable and starts to subduct.

A possible contribution to the uncertainty in determining the critical yield stress is that at the vicinity of the critical value, the behavior may be difficult to interpret. In some cases that as the yield stress gets close to a critical value, the surface velocity increases slowly and it may take more than 10^5 timesteps to reach a point of overturn, whereas typically it takes less than 10^4 timesteps to a drastic increase in surface velocity (Fig. 2.20 right). This may be due to the behavior of dynamic system near a critical point.

2.7 Critical depth of plastic failure zone

For subduction to occur, the lithosphere has to be sufficiently weak so that it can be mobilized by stresses arisen from mantle convection. As seen in Fig. 2.18 and 2.19, the lid remains stagnant if the plastic yield zone is small. Therefore the question is how deep does this plastic zone have to penetrate for the lid to be mobilized? Previous theories proposed that the plastic zone has to penetrate through some critical depth $\delta_{\rm pl}$ defined by a critical temperature T_c:

$$\frac{\delta_{\rm pl}}{\delta_0} = \frac{T_c - T_0}{T_i - T_0}, \tag{2.40}$$

where $\delta_0 = \delta_{\rm lid} + \delta_{\rm rh}$. The model of Fowler and O'Brien (2003) predicts that $\delta_{\rm pl}$ is defined by the temperature that gives the interior viscosity. For Newtonian rheology, this means that the plastic zone has to extend through the base of the lid. Solomatov (1995, 2004b) suggested that $\delta_{\rm pl}$ only has to penetrate to the isotherm at which the viscosity contrast with the interior viscosity is $e^{4(n+1)}$, where n is the stress exponent for non-Newtonian viscosity.

To examine these hypotheses, we look at the stress profile at the downwelling edge ($x = a$) to determine the depth of the plastic zone, as the stresses at this edge are the highest and this is where subduction starts (Fig 2.22). The depth of the plastic zone is defined by extent of the stress modified by the plastic flow law in Eq. 2.7. The exact value of $\delta_{\rm pl}$ and the stress at this depth are found by the intercept of the stress calculated from linear extrapolation from the top (where stress is determined by the yield stress) and exponential extrapolation from the creep regime just below the plastic depth. The values of $\delta_{\rm pl}$ for constant yield stress cases and that for constant yield stress gradient cases are close. It is noted that the stress at depth $\delta_{\rm pl}$ in constant yield stress gradient cases

is about twice as much as that in constant yield stress cases. The force on the lid is $\delta_{\rm pl}\tau_{y,cr}$ for constant yield stress and $0.5\delta_{\rm pl}\tau'_{y,cr}$ for constant yield stress gradient. This implies that the force on the lid is about the same for both constant yield stress and yield stress gradient.

As we see from the effects of aspect ratio on steady-state stress distribution, the stresses in the interior become comparable or even exceed the surface stresses as the aspect ratio and Ra decrease and viscosity contrast increases. This means that the plastic zone may not propagate from the top but also develop at depths in the lid, and the plastic zone does not span the whole top part of the cell. (Fig. 2.23). This may represent another regime of lid failure. These cases are thus excluded from our scaling analysis.

The depth of the plastic zone is determined from drop in stress by the yield stress. We note that the zone of reduced viscosity due to the yield stress may correspond to the zone of reduced stress as shown in Fig. 2.22. However this does not always hold, especially for cases with higher θ. Figure 2.24 shows that the transition of the plastic zone to creep flow may not correspond to the sharp change in the viscosity. This means that the viscosity at the plastic depth and the maximum viscosity are different, since the reduction in viscosity is not only determined by the yield stress but also by the strain rate.

To find out whether there is a critical viscosity contrast in lithospheric failure, we examine both the viscosity contrast at plastic depth $\Delta\eta_{\rm pl}$ and the maximum viscosity contrast $\Delta\eta_{\rm max}$. The maximum viscosity needs to be determined by extrapolation as the resolution near the point where the viscosity is maximum is not high enough to resolve sharp changes in stress and viscosity. The point of maximum viscosity is found by extrapolating the values from both above and below the maximum point (e.g. Fig. 2.24 right). The viscosity is extrapolated linearly from the two points above the maximum point, and below the maximum point the viscosity is calculated from

temperature. The intersection of these two curves determines the maximum viscosity and its depth. We found that these two viscosity contrasts are mostly within the same order of magnitude. Figure 2.25 shows that the maximum viscosity seems to depend on the original non-yielding viscosity contrast $\Delta\eta$. For exponential viscosity and Arrhenius viscosity cases at low non-yielding viscosity contrast, the maximum viscosity contrast $\Delta\eta_{\max}$ increases with non-yielding viscosity contrast. This may be because they are close to transitional regime. At higher $\Delta\eta$, the increase in $\Delta\eta_{\max}$ seems to decline with increasing $\Delta\eta$, but the spread of data prevents us from concluding that $\Delta\eta_{\max}$ converges towards higher viscosities. As with the maximum viscosity contrast, $\Delta\eta_{\mathrm{pl}}$ also does not display linearity or convergence clearly with either the non-yielding viscosity contrast or θ (Fig. 2.26).

Since the critical viscosity contrast is neither a constant or a function of θ, we look at the depth of the plastic zone to derive scaling relations for the yield stress. We investigate the plastic depth δ_{pl} as a fraction of the lid thickness. For scaling purposes, the lid thickness was previously defined at the middle of the convecting cell. Here, since δ_{pl} is defined at the downwelling edge, we have to determine a lid thickness at the edge $\delta_{\mathrm{lid,max}}$. This is done by extrapolating the mid-width lid slope to the downwelling edge (Fig. 2.10). As shown is Fig. 2.26, the plastic depth is approximately 0.3-0.5 of the lid thickness. We take approximate values for our scaling relations rather than scaling these properties with convective parameters because the trends observed in Fig. 2.26 maybe due to insufficient viscosity contrasts which place convection on the boundary of transitional regime, especially for $\theta = 13$ in which the viscosity is reduced to $\sim 10^4$ by the critical yield stress.

To find the lid stress at δ_{pl} using Eq. 2.34, we also need to determine the distance of the base of the plastic zone from the convective interior y_{pl}. The lid base is at δ_{rh} from the interior, so we express y_{pl} in terms of δ_{rh} to give a sense of distance in relation to rheological sublayer thickness.

While there is a general trend of increasing of $y_{\rm pl}/\delta_{\rm rh}$ with θ, it is difficult to discern a correlation as $y_{\rm pl}/\delta_{\rm rh}$ fluctuates, thus we take $y_{\rm pl} \approx 3\delta_{\rm rh}$ for our scaling relations.

The dependence of $\delta_{\rm pl}$, $y_{\rm pl}$, and $\Delta\eta_{\rm pl}$ on Ra and aspect ratio are very weak and therefore assumed negligible.

2.8 Scaling for critical yield stress and critical yield stress gradient

2.8.1 Critical yield stress scaling theory

In deriving a theoretical scaling for the critical yield stress, we assume an approximate balance between the force generated by the shear stresses acting at the base of the lid and the normal stress acting on the side of the lid and we assume that the latter are largely dominated by the stresses in the plastic zone δ_y (Solomatov 2004b) and Fig. 2.27). Thus we can express the yield stress as:

$$\begin{aligned} \tau_y &\sim \tau_{\rm lid}\frac{a}{\delta_y} \\ &= {\rm Ra}\frac{dT}{dy}\lambda\frac{y_{\rm pl}^2}{2}\frac{a}{\delta_y}. \end{aligned} \tag{2.41}$$

In the case of a constant yield stress gradient ($\tau_y = \tau_y' z$), τ_y' can be scaled as

$$\begin{aligned} \tau_y' &\sim \tau_{\rm lid}\frac{a}{\delta_y^2} \\ &= {\rm Ra}\frac{dT}{dy}\lambda\frac{y_{\rm pl}^2}{2}\frac{a}{\delta_y^2}. \end{aligned} \tag{2.42}$$

In Eqs. 2.41 and 2.42, the yield stress is treated as the normal stress whereas the lithosphere stresses are shear stress. However the magnitude of stresses is expressed in second invariant, and

the yield stress in von Mises criterion also put a limit the second stress invariant. To see which stress component contributes to the second invariant, we plot the normal stress and shear stress profiles in Fig. 2.28. Inside the lid where plastic failure occurs normal stress dominates, whereas shear stress exceeds normal stress below the plastic depth.

The critical yield stress is the stress at $\delta_y = \delta_{\rm pl}$. The critical plastic depth $\delta_{\rm pl}$ is taken to be 0.3 to 0.5$\delta_{\rm lid}$, and $y_{\rm pl}$ is about 2 to 4δ_{rh}.

$$\tau_{\rm lid} \sim C_1 {\rm Ra} \Delta T_{rh} \lambda \delta_{rh}, \tag{2.43}$$

$$\tau_{y,cr} \sim C_2 {\rm Ra} \Delta T_{rh} \lambda a \frac{\delta_{rh}}{\delta_{\rm lid}}, \tag{2.44}$$

$$\tau'_{y,cr} \sim C_3 {\rm Ra} \Delta T_{rh} \lambda a \frac{\delta_{rh}}{\delta^2_{\rm lid}}. \tag{2.45}$$

For $\tau_{\rm lid}$ expressed in terms of Nu (Eq. 2.39), noting that Nu $\sim dT/dy \sim \delta_{\rm lid}^{-1}$,

$$\tau_{\rm lid} \sim C_1 {\rm RaNu} \lambda \delta^2_{rh}, \tag{2.46}$$

$$\tau_{y,cr} \sim C_2 {\rm RaNu}^2 \lambda a \delta^2_{rh}, \tag{2.47}$$

$$\tau'_{y,cr} \sim C_3 {\rm RaNu}^3 \lambda a \delta^2_{rh}. \tag{2.48}$$

where C_1, C_2, C_3 ranges from 4-16, 8-53, and 16-178 respectively.

From the previous sections, since $\Delta T_{\rm rh}/\Delta T$, $\delta_{\rm rh}/d$, $\delta_{\rm lid}/d$, and λ are all scaled in terms of Ra, a, and θ with scaling exponents summarized in Table 2.1. $\tau_{\rm lid}$, $\tau_{y,cr}$, and $\tau'_{y,cr}$ can be scaled in terms of Ra, a, and θ. The results are listed on Table 2.2.

2.8.2 Numerical results for critical yield stress and yield stress gradient: Arrhenius vs exponential viscosity

Figures 2.29 and 2.30 show that both $\tau_{y,cr}$ and $\tau'_{y,cr}$ decrease with increasing θ and total viscosity contrast and might converge to asymptotic values at high viscosity contrasts, although it is difficult to tell from our limited data. To estimate the accuracy of Frank-Kamenetskii approximation in the prediction of critical yield stress, we express the ratio of yield stress for Arrhenius viscosity to that for exponential viscosity $R_\tau = \tau_{y,cr,\mathrm{Arr}}/\tau_{y,cr,\mathrm{exp}}$ and similarly for critical yield stress gradient with $R_{\tau'} = \tau'_{y,cr,\mathrm{Arr}}/\tau'_{y,cr,\mathrm{exp}}$ to look at the dependence of these ratios on θ (Fig. 2.31 and 2.32). Both R_τ and $R_{\tau'}$ increase with θ and the values of yield stress for Arrhenius viscosity and that for Frank-Kamenetskii approximation get closer as the viscosity contrast increases, assuming that $R_\tau < 1$ and $R'_\tau < 1$ at all θ.

For the cases tested at resolution that is doubled, we find that the values for R_τ and $R_{\tau'}$ are within 5% difference. Therefore $64 \times 64a$ resolution is sufficient for our single-cell steady-state convection analysis.

To find the dependence of R_τ and $R_{\tau'}$ on the Arrhenius viscosity contrast $\Delta\eta_{\mathrm{Arr}}$, we consider ratio of Arrhenius viscosity contrast to exponential viscosity contrast ($\Delta\eta_{\mathrm{Arr}}/\exp\theta$). This ratio reflects the difference between Arrhenius viscosity contrast and exponential viscosity contrast: the larger the ratio, the greater the difference. Figure 2.33 shows that values of the two $\tau_{y,cr}$ approach each other as the Arrhenius viscosity gets closer to the exponential viscosity. It also suggests that R_τ and $R_{\tau'}$ are mainly determined by the Frank-Kamenetskii parameter θ but less sensitive to Ra and a. As the difference between the Arrhenius viscosity and exponential viscosity increases, both R_τ and $R_{\tau'}$ appear to approach some asymptotic value.

We also investigate the dependence of critical yield stress and yield stress gradient on aspect ratio (Fig. 2.34 and 2.35). The positive power law coefficient (see Table 2.1) implies that with smaller aspect ratio, the critical yield value is lower and thus more difficult to reach the yielding criterion. Therefore smaller cells are more stable. This may explain the phenomenon where overturning of the cold lid is observed once or a few times but then stabilized after reconfiguring into smaller cells.

Figures 2.36 and 2.37 and Table 2.1 show that $\tau_{y,cr}$ and $\tau'_{y,cr}$ are approximately proportional with Ra.

The plots in Figures 2.29, 2.30, and 2.34–2.37 show that the scaling exponents could have a range of values, and the cases using Arrhenius viscosity may have a bit different values from those with exponential viscosities. Figure 2.38 shows that while the scaling exponent for Ra and a for exponential viscosity cases lie between the range obtained from Arrhenius viscosity cases, the exponent for θ varies with surface temperature T_0, Ra, and a. In general the scaling exponent of θ increases with the viscosity contrast (i.e. lower T_0), a, and moderately with Ra. This may be related to the difference in the stress distribution in the lid in Arrhenius cases, especially towards the downwelling edge, as discussed previously. In the future it will be worthwhile to look in more detail at the stress variations for the Arrhenius viscosity, and to see if there are any relationships between R_τ, $R_{\tau'}$ and T_0 at even lower T_0 (i.e. at higher viscosity contrasts.)

2.9 Discussion and conclusion

2.9.1 Comparison with other studies of stress scaling laws

The studies dealing with convective stress scaling often aim to provide an expression for stress in terms of radius and mass of a planet to predict the likelihood of plate tectonics. They reached various conclusions (e.g., O'Neill and Lenardic 2007; O'Neill et al. 2007; Valencia and O'Connell 2007, 2009; Korenaga 2010a; van Heck and Tackley 2011; Stamenkovic and Breuer 2014). One of the main difficulties in deriving convincing scaling laws for plate tectonics initiation was a poor understanding of lid stresses and how they are related to lid failure. In the present study we have addressed these issues using two-dimensional steady-state convective cell simulations. This is the simplest system to analyze and yet even for this system the derivation of scaling laws proved to be complicated and not well described by the existing asymptotic theories. Below we discuss some differences between our study and previous studies and summarize our scaling laws in a dimensional form.

In some studies (e.g., Moresi and Solomatov 1998; Trompert and Hansen 1998; Tackley 2000a; Fowler and O'Brien 2003), the authors assumed that subduction occurs when the stresses in the convective interior exceed the yield stress. This means that subduction begins when not only the lid but also the interior of the convective cell fails. However, subduction initiation may not necessarily require the failure of interiors but instead may only require failure of just a small portion of the lid. The stresses in the lid are several orders of magnitude higher than the stresses in the interior and also they scale differently. Thus, the assumption regarding what part of the convective cell must fail in order for subduction to begin is critically important. In this study we have investigated this assumption quantitatively, based on a detailed analysis of stresses and other parameters in the

convective cell, and then formulated the critical conditions for subduction initiation.

In agreement with Fowler (1985), we have shown that the lid slope is a key factor the stresses in the lid. However, our model has several important differences from Fowler (1985). The theoretical solution in Fowler (1985) is a similarity solution and does not take into the finite horizontal extent of the lid. Our model has vertical boundaries and thus the structure of the lid in our model is more complex. Also, the solution in Fowler (1985) is an asymptotic solution requiring very high values of parameters, such as Ra and θ, and a satisfaction of certain asymptotic conditions, which are not reached in our simulations and may not necessarily be reached on planets. Thus, our scaling laws are not asymptotic in this sense. Also, solutions in Fowler (1985) are obtained for two end-member cases, the large lid slope case and the small lid slope case. We find that the lid slope behaves in a more complex way between these two end-member cases. We have determined a scaling law for the lid slope numerically and used it to derive the scaling law for the stresses in the lid.

Our analysis suggests that the stresses in the lid increase approximately as a square of the distance from the bottom of the lid (Eq. 2.34 and Fig. 2.16). This agrees with the asymptotic analysis of Fowler (1985) but is different from the stress distribution in Solomatov (2004b). In Solomatov (2004b) the stress distribution was more complex because the convective cell was heated from within rather than from the bottom and the internal heating affected the temperature-induced density distribution in the lid. At Rayleigh numbers higher than those reached in Solomatov (2004b), the lid is expected to become sufficiently thin so that the heat production inside the lid would be negligible compared to the heat flux at the base of the lid. Thus, we expect that for convection with internal heating the stress distribution in the lid should approach the quadratic distribution that we observe for convection with bottom heating.

We find that subduction initiation requires that only a part of the lid undergoes plastic failure,

roughly 0.3 to 0.5 of the total lid thickness. This generally agrees with the analysis in Solomatov (2004b) and confirms that the plastic failure does not have to extend all the way to the bottom of the lid as was assumed in Fowler and O'Brien (2003). However, unlike Solomatov (2004b) we determine the distance to the boundary of the plastic failure zone by measuring it from the base of the lid and scaling it in terms of the rheological boundary layer thickness. We find that such an approach is more appropriate because the mobility of the lid is largely controlled by the viscosity contrast between the zone of failure and the convective interior of the cell, which in turn is scaled with the rheological boundary layer thickness.

2.9.2 Estimates for the Earth

To compare our results with those obtained in Solomatov (2004b,a), we convert the critical yield stress $\tau_{y,cr}$ and critical yield stress gradient $\tau'_{y,cr}$ into their dimensional forms (Eqs. 2.20, 2.22) and estimate the critical yield strength and the critical coefficient of friction μ for subduction initiation on the Earth.

The interior viscosity cannot be reliably estimated from the viscosity law alone and is usually determined from better constrained properties such as lithospheric thickness. Therefore, following Solomatov (2004b) we use the scaling law for δ_0 (Table 2.1) and present the results in terms of the thickness of the thermal boundary layer $\delta_0 \sim 100$ km instead of the mantle viscosity η_1.

The scaling law for the critical yield stress depends strongly on aspect ratio a. Previous studies have scaled the aspect ratio from half-space cooling of lithosphere (Korenaga 2010b; Stamenkovic and Breuer 2014) or estimated from numerical simulations (Solomatov 2004b,a)) whereas it was assumed to be on the order of 1 in Valencia and O'Connell (2009). We use the horizontal width of the convective cells as $l_{\mathrm{hor}} = ad \sim$100 km as a very rough value to compare our estimates

with those in Solomatov (2004b,a). This value was inferred from observational constraints on the present-day horizontal scale of sublithospheric convective structures (Solomatov 2004b).

Using the results in (Table 2.1), we obtain that the dimensional critical yield stress for subduction initiation is

$$\tau_{y,cr} \sim 1.95\alpha\rho g \left(\frac{E}{RT_i^2}\right)^{-1.03} \Delta T^{-0.03}\delta_0^{-0.41} l_{\rm hor}^{1.78} d^{-0.37}. \tag{2.49}$$

For comparison, Solomatov (2004b,a) give:

$$\tau_{y,cr} \sim 13\alpha\rho g \left(\frac{E}{RT_i^2}\right)^{-2} \Delta T^{-1} l_{\rm hor}. \tag{2.50}$$

The critical coefficient of friction μ for subduction initiation is

$$\mu \sim 89\alpha \left(\frac{E}{RT_i^2}\right)^{-1.74} \Delta T^{-0.74}\delta_0^{-1.55} l_{\rm hor}^{1.87} d^{-0.32}, \tag{2.51}$$

and in Solomatov (2004b,a):

$$\mu \sim 50\alpha \left(\frac{E}{RT_i^2}\right)^{-2} \Delta T^{-1}\delta_0^{-1} l_{\rm hor}. \tag{2.52}$$

Using the typical values of various physical parameters (Table 2.3), we estimate that the yield strength for the Earth is 5 MPa which is of the same order of magnitude as 3 MPa obtained by Solomatov (2004b,a). To see how variations in various parameters may affect these estimates it is useful to present the estimates in a different form. Our estimate (Eq. 2.49) can be written as

$$\tau_{y,cr} \sim 5 \left(\frac{100\ {\rm km}}{\delta_0}\right)^{0.41} \left(\frac{l_{\rm hor}}{100\ {\rm km}}\right)^{1.78} \left(\frac{500\ {\rm km}}{d}\right)^{0.37} {\rm MPa}, \tag{2.53}$$

and the estimate from Solomatov (2004b,a) (Eq. 2.50) is

$$\tau_{y,cr} \sim 3 \left(\frac{l_{\rm hor}}{100 \text{ km}} \right) \text{ MPa}, \tag{2.54}$$

from Eq. 2.50.

Our estimates of the critical friction coefficient μ is 8×10^{-3}, which is a factor of 3 larger than 3×10^{-3} obtained in Solomatov (2004b,a). Our estimate can be written as

$$\mu \sim 0.008 \left(\frac{100 \text{ km}}{\delta_0} \right)^{1.55} \left(\frac{l_{\rm hor}}{100 \text{ km}} \right)^{1.87} \left(\frac{500 \text{ km}}{d} \right)^{0.32}, \tag{2.55}$$

and the estimate from Solomatov (2004b,a) (Eq. 2.50) is

$$\mu \sim 0.003 \left(\frac{l_{\rm hor}}{100 \text{ km}} \right) \left(\frac{100 \text{ km}}{\delta_0} \right). \tag{2.56}$$

If we take into account the fact that Frank-Kamenetskii approximation that we used to derive the scaling laws overestimate the critical yield stress and the critical friction coefficient (Fig. 2.33), then both ours and the estimates in Solomatov (2004b,a) should be further reduced by a factor of 2 (Fig. 2.33), depending on the values of the viscosity parameters and the Rayleigh number.

One major difference between our scaling laws and the scaling laws obtained in Solomatov (2004b) is a much stronger dependence of the critical yield stress and critical friction coefficient on the width of the convecting layer $l_{\rm hor}$ – they scale roughly as $\sim l_{\rm hor}^2$ as opposed to the previous scaling $\sim l_{\rm hor}$. This means that the critical values of the yield stress and friction coefficient would increase by 2 to 4 orders of magnitude if the width of the convective cells increased by 1 to 2 orders of magnitude (for example, in the past history of the Earth) and thus, at least in principle,

could reach the experimentally observed values that are on the order of 1000 MPa for $\tau_{y,cr}$ and μ ∼0.6–0.85 (e.g., Byerlee 1978; Goetze and Evans 1979; Kohlstedt et al. 1995; Mei et al. 2010), and values constrained by loading models with in situ stress measurements of Hawaiian Islands (Zhong and Watts 2013) which are 0.25-0.7 for μ and 100-200 MPa for lithospheric stress. This implies that the chances of plate tectonics might be higher than we thought before. Time-dependent calculations and a more realistic formulation of the problem are required to better understand the implications of these results for plate tectonics initiation.

2.9.3 Uncertainties in stress scaling

The scaling laws derived here are applicable to Newtonian rheology, therefore the activation energy for diffusion creep is used in our calculations. However it should be noted that dislocation creep is probably the dominant mechanism in the lithosphere Karato and Wu (1993). For the Earth wet dislocation creep may be preferable (Solomatov and Moresi 2000), while for other terrestrial planets such as Venus might have dry lithosphere. To apply on a wider range of planets including icy bodies, scaling laws based on non-Newtonian rheology will be required.

In previous scaling theories the lid slope is often considered to be small because the lid thickness is assumed to be relatively small. Even in the large lid slope end member case in Fowler's theory, $\delta_{\rm lid}$ is assumed to be small relative to the thickness of the convecting layer. However our simulation indicates that the slope may be significant, so the derivations may need to be modified to take this into account.

Free-slip boundary conditions are often used in solving equations for thermal convection, but this restricts the vertical motion of the surface. Recent studies have used the free-surface boundary conditions, which is closer to natural surface condition as both normal and shear stress on the

surface is reduced to zero (Zhong et al. 1996; Schmeling et al. 2008; Kaus et al. 2010; Crameri et al. 2012; Kramer et al. 2012). It maybe computationally expensive to implement this for the time being, but it could be worthwhile to explore its effect on scaling relations for stresses in the future.

Our numerical results show that $\tau_{y,cr}$ of Arrhenius viscosity approaches that of exponential viscosity as the Frank-Kamenetskii parameter θ increases. This enables us to use exponential viscosity law to extrapolate to high Arrhenius viscosity contrast conditions. Besides the Frank-Kamenestskii approximation, the viscosity contrasts can be reduced in other ways, one of which is to set a cut-off viscosity. The stress structure resulting from the cut-off viscosity will have to be examined. We can then compare accuracy of these approximations and apply them to extrapolate the results to planetary parameters.

Our results generally support previous conclusions that in order for the convective regime on the terrestrial planets in the inner Solar System to change from stagnant lid convection to plate tectonics, the yield stress of the lithosphere should be much smaller (several MPa) than that predicted by laboratory experiments on rock deformation (hundreds of MPa as predicted by Byerlee's law). However, our results suggest a much stronger dependence of the critical yield stress on the horizontal width of the convective cells. This opens a possibility of subduction initiation even for the large, experimentally measured, lithospheric strength provided that a sufficiently long convective cell forms in a time-dependent mantle convection. In the future it would be important to investigate the role of initiation conditions and statistical fluctuations of convective cells for the initiation of subduction in time-dependent convection.

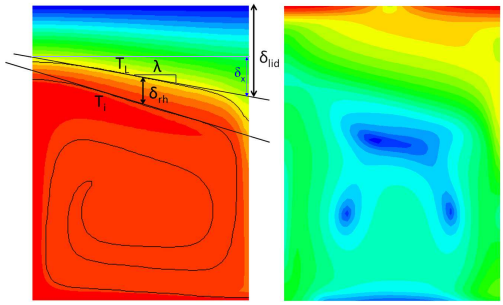

Figure 2.1 Temperature (left) and stress fields (right) of a steady-state convective cell. Color scale goes from high (red) to low (blue). The lid is defined by an isotherm T_L, and the interior temperature T_i is found by averaging the temperature of the convecting interior excluding boundary effects. For scaling purposes, the lid slope λ and rheological sublayer thickness δ_{rh} is taken at mid-width, whereas lid thickness δ_{lid} is extrapolated to the edge from the lid slope in the middle.

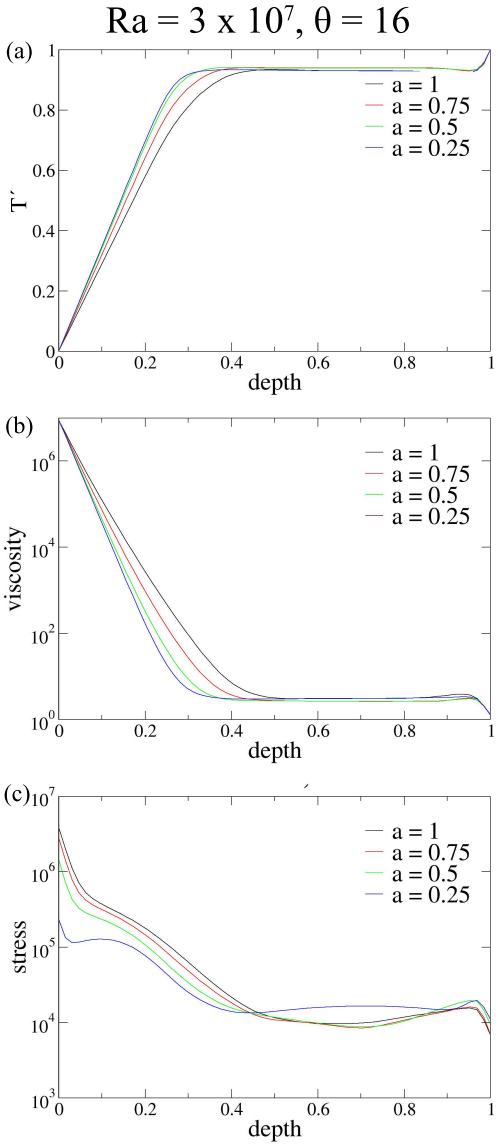

Figure 2.2 Comparison of (a) viscosity (b) temperature (c) stress profiles of exponential viscosities for $\theta = 16$, $Ra = 3 \times 10^7$, and varying a. The somewhat different stress profile of $a = 0.25$ suggests that the surface stress boundary layer is not the region with highest stress.

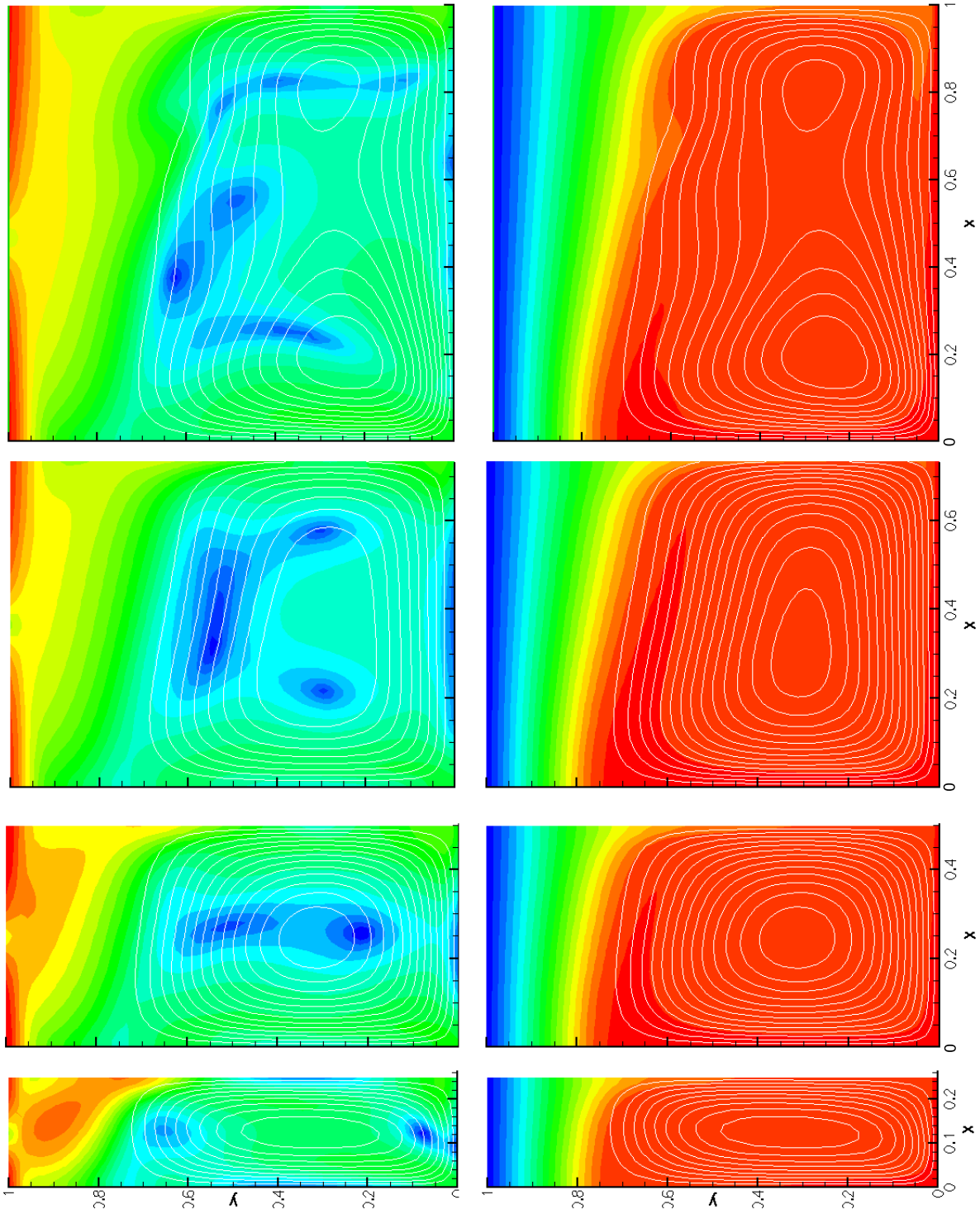

Figure 2.3 Stress (top row) and temperature fields (bottom row) of convecting cells with $Ra = 3 \times 10^7$, $\theta = 16$, and various a.

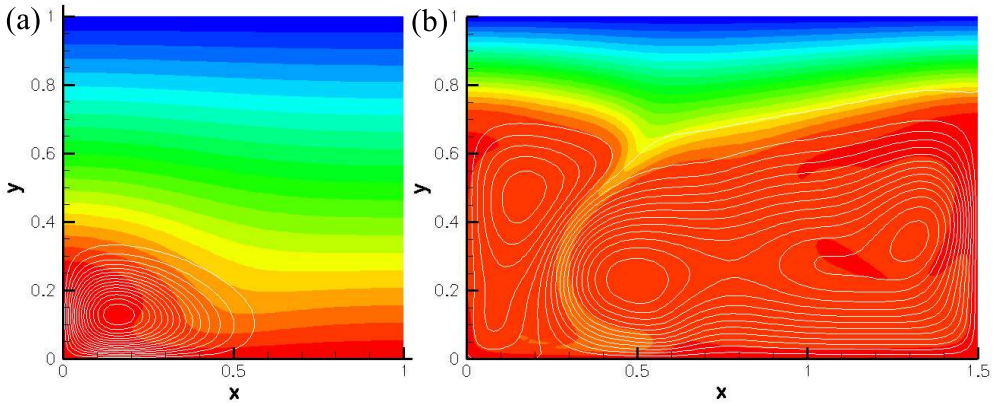

Figure 2.4 Localized convection and multiple subcells in steady-state convection. (a) $\theta = 19$, $T_0 = 0.6$, $a = 1$, $Ra = 1 \times 10^7$. (b) $\theta = 16$, $T_0 = 0.6$, $Ra = 3 \times 10^7$.

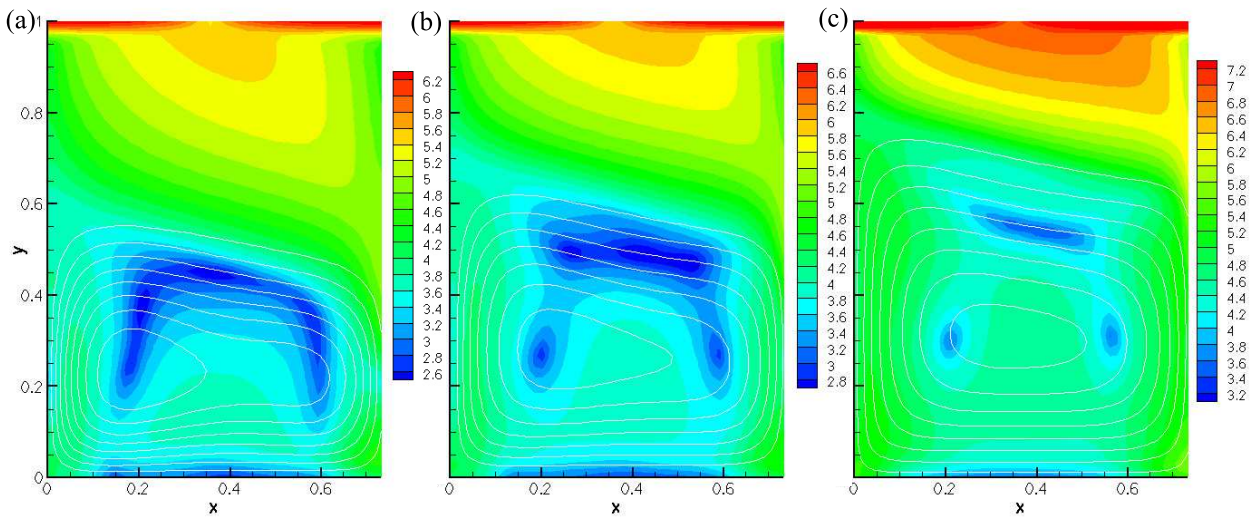

Figure 2.5 Stress structure of steady state cases with $\theta = 16$, $a = 0.75$, $T_0 = 0.8$. (a) $Ra = 10^7$ (b) $Ra = 3 \times 10^7$ (c) $Ra = 10^8$. The area of convecting interior becomes larger as Ra increases and the thickness of the stagnant lid decreases. Scale shows the values of $\log \tau$.

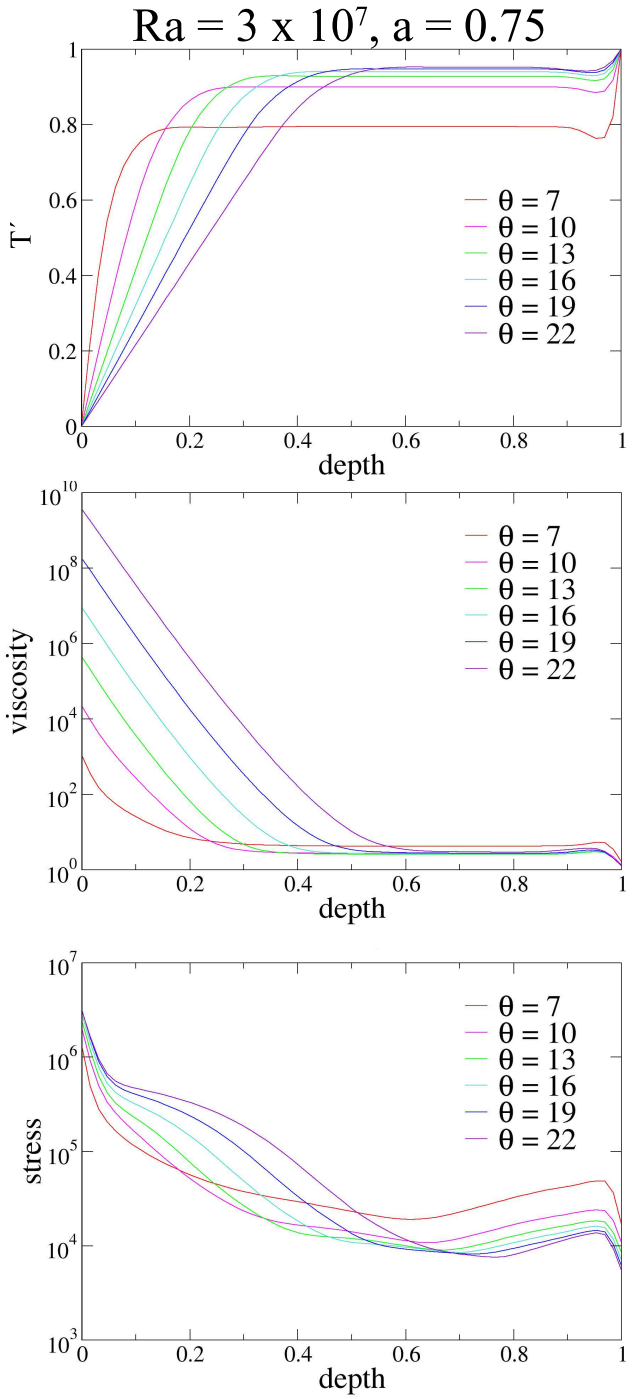

Figure 2.6 Temperature, viscosity, and stress profiles of $Ra = 3 \times 10^7$, $a = 0.75$ and varying Frank-Kamenetskii parameter θ.

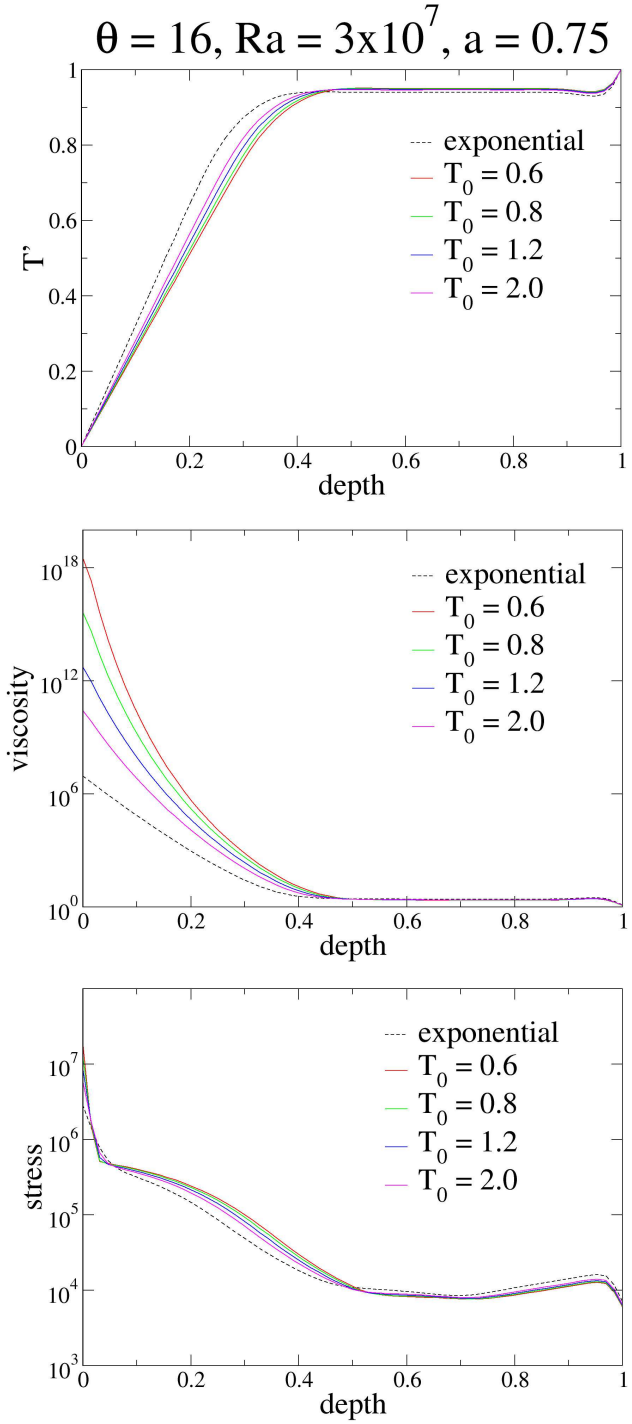

Figure 2.7 Comparison of temperature, viscosity, and stress profiles of Arrhenius and exponential viscosities for $\theta = 16$, $Ra = 3 \times 10^7$, $a = 0.75$ and various T_0.

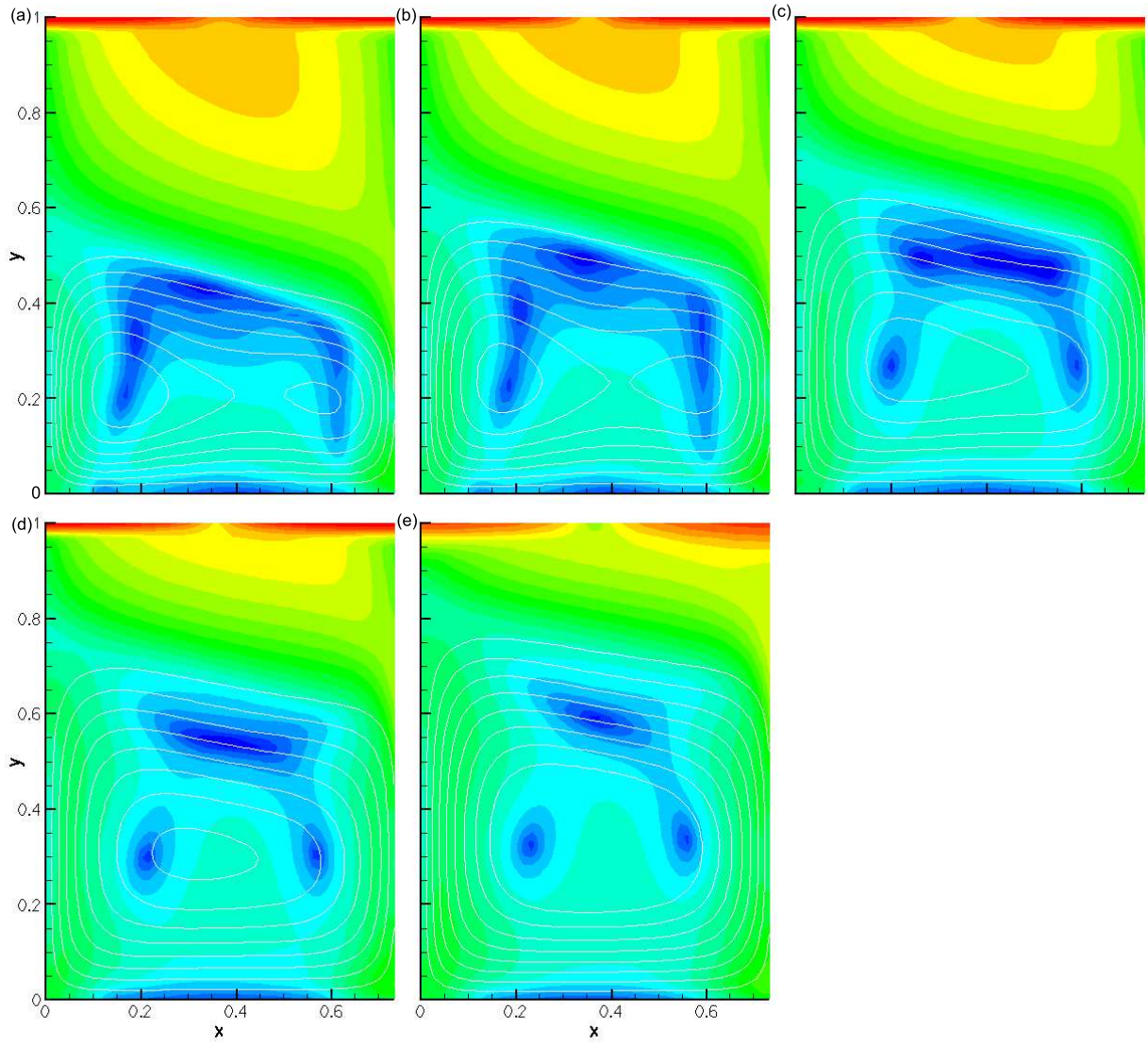

Figure 2.8 Stress structure of steady state cases with $Ra = 3 \times 10^7$, $T_0 = 0.8$, $a = 0.75$. (a)–(d) Arrhenius viscosity with (a) $\theta = 22$, (b) $\theta = 19$, (c) $\theta = 16$, (d) $\theta = 13$, and (e) exponential viscosity with $\theta = 13$. Color scale shows the values of $\log(\tau)$. White lines represent streamlines.

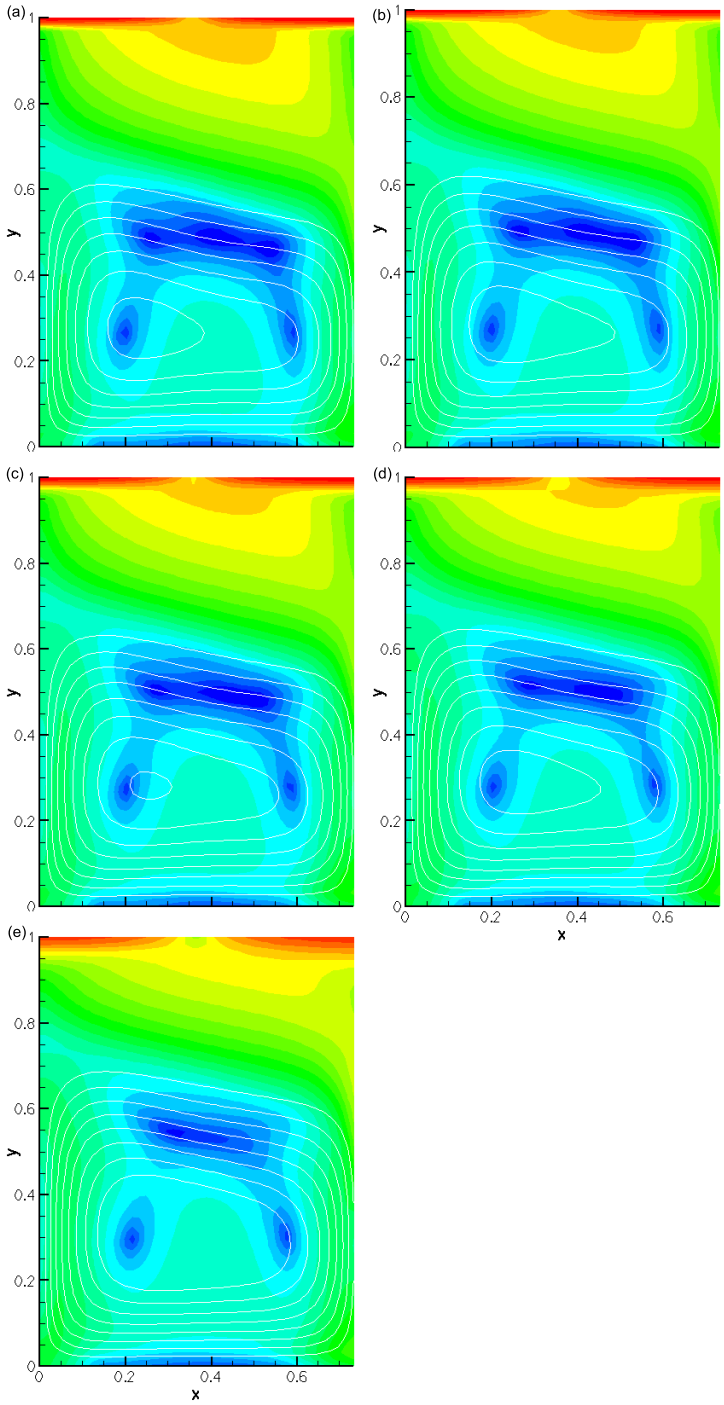

Figure 2.9 Stress structure of steady state cases with $Ra = 3 \times 10^7$, $\theta = 16$, $a = 0.75$. Cases (a)–(d) use Arrhenius viscosity with (a) $T_0 = 0.6$, (b) $T_0 = 0.8$, (c) $T_0 = 1.2$, (d) $T_0 = 2.0$. Case (e) uses exponential viscosity. Color scale shows the values of $\log(\tau)$. White lines represent streamlines.

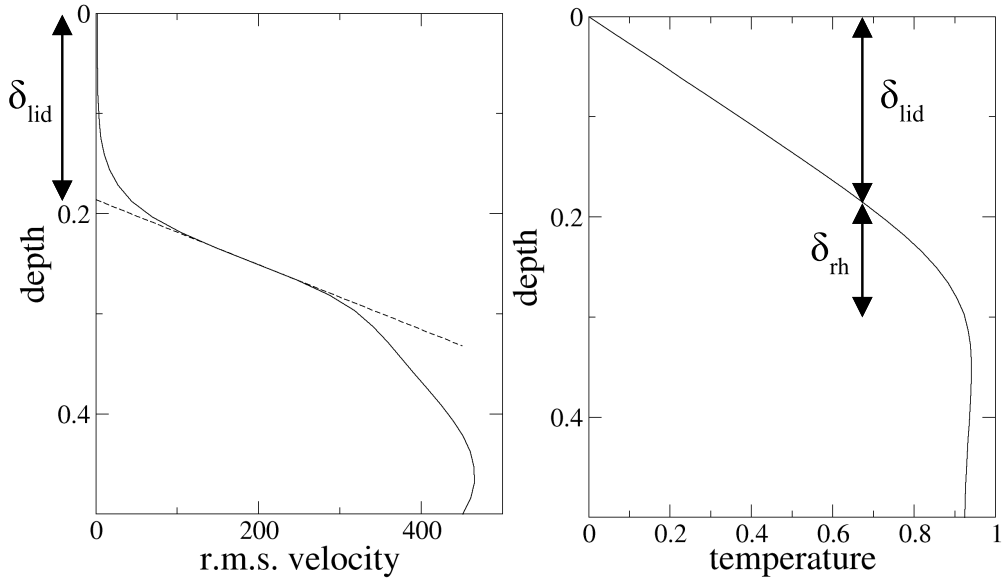

Figure 2.10 Velocity profile taken at mid-width of the cell ($x = 0.5a$). Dotted line is the linear extrapolation of the maximum velocity gradient, and the lid base is marked at the depth at which this line intersect with the vertical axis.

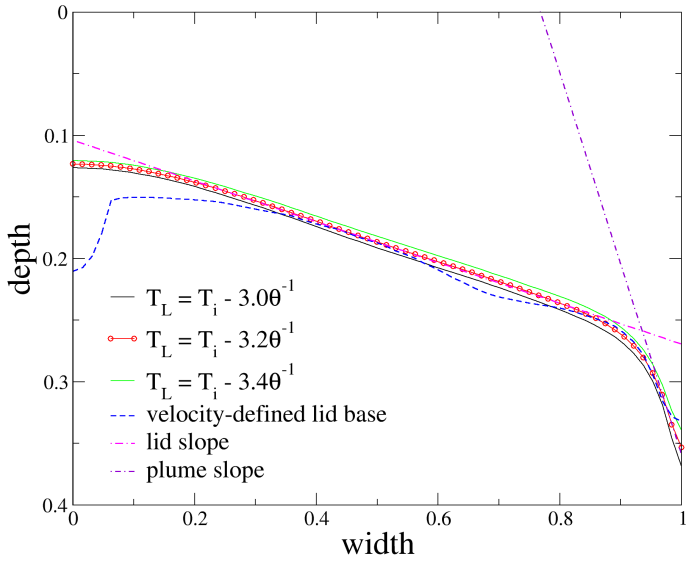

Figure 2.11 Top part of a convective cell showing various definitions of the lid base. The lid base defined by the velocity gradient is shown in dashed line, and it matches the temperature lid base defined at $T_L = T_i - 3.2\theta^{-1}$ at around the mid-point. The lid slope is estimated at the mid-point. The lid slope is taken at the slope in the middle, and the plume slope is taken at the downwelling end.

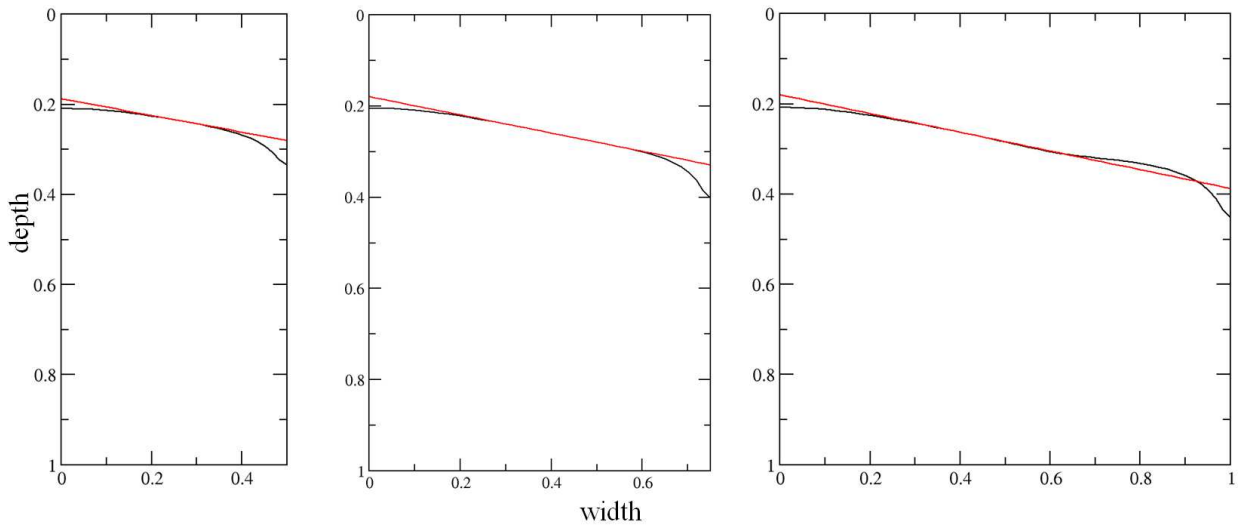

Figure 2.12 The slope of the lid base at various aspect ratios. The lid slope deviates from the linear approximation as the cell aspect ratio and viscosity contrast increase, therefore a non-constant value of the lid slope may affect the scalings.

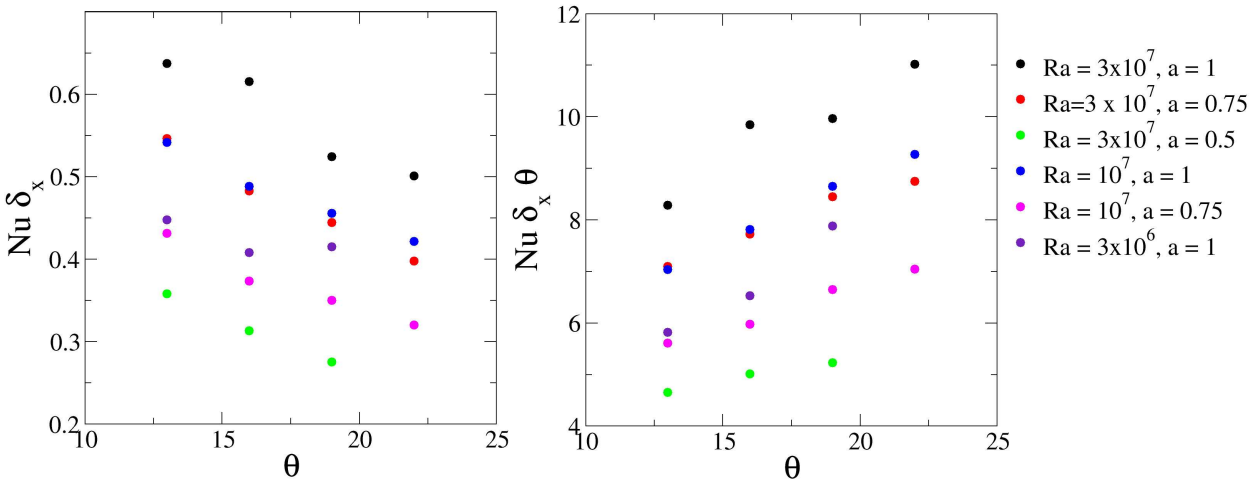

Figure 2.13 Plots of Nuδ_x (or δ_x/δ_{lid}) and Nu$\delta_x\theta$ (or $\theta\delta_x/\delta_{lid}$) as a function of θ.

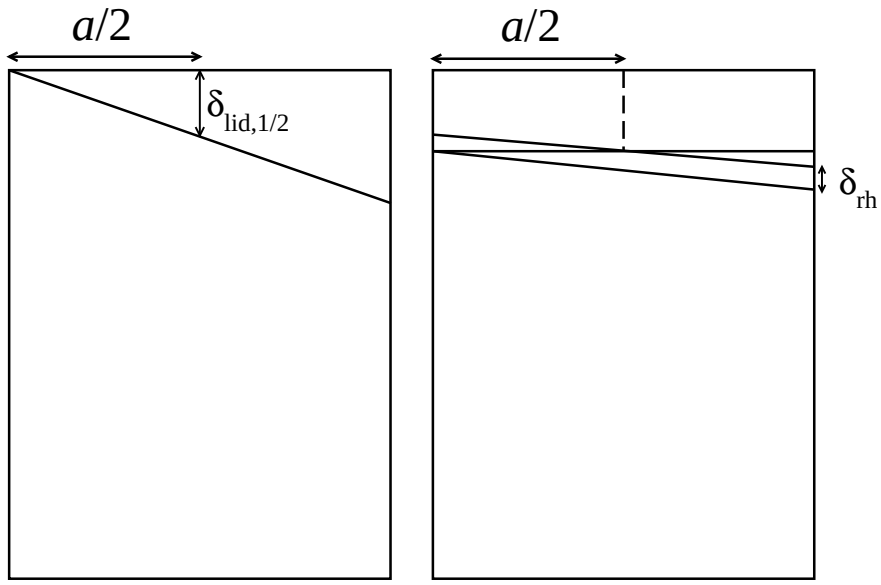

Figure 2.14 Relationship between the aspect ratio and the lid slope. The lid slope cannot be larger than $2\delta_{\mathrm{lid}}/a$ in the large lid slope end member case, and it cannot be larger than $2\delta_{\mathrm{rh}}/a$ in the small lid slope end member case. However it is possible that the lid slope can be smaller than $2\delta_{\mathrm{rh}}/a$.

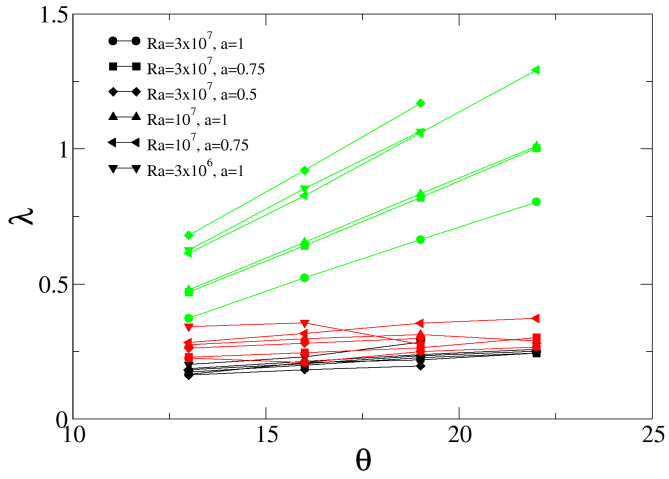

Figure 2.15 Comparison between lid slopes obtained from numerical solutions (black) and those from theoretical constraints (red: small lid slope approximation $\lambda \approx 2\delta_{\mathrm{rh}}/a$; green: large lid slope approximation $\lambda \approx 2\delta_{\mathrm{lid},1/2}/a$).

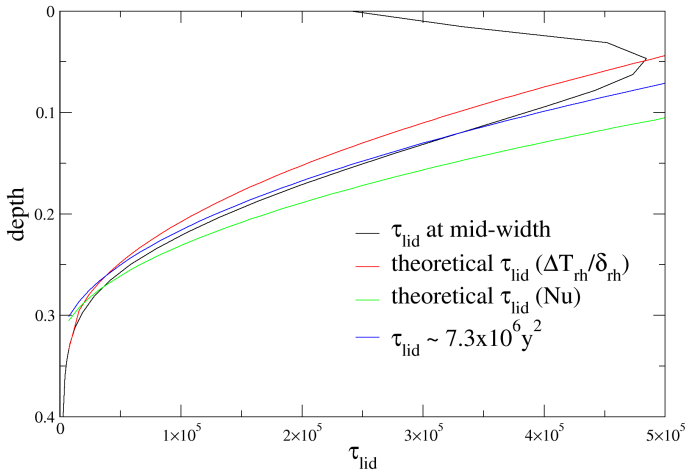

Figure 2.16 Comparison of stress profiles at mid-width obtained from numerical calculations and theory. Blue line represents the best fit to numerical solutions of stresses. The stress profile is taken at mid-width, where the stresses in the surface boundary layer is lower than the interior as shown in the 2-D stress fields.

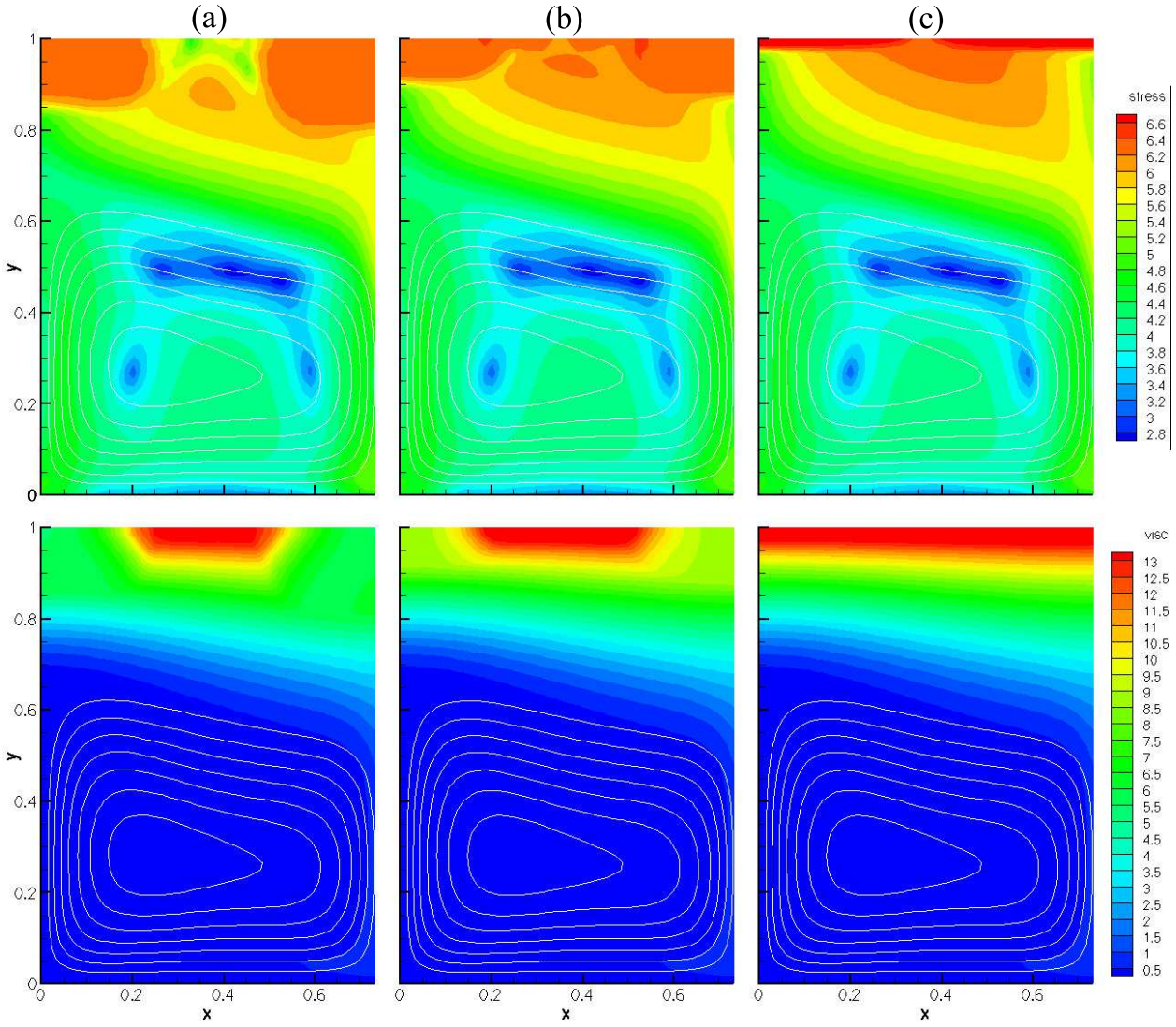

Figure 2.17 Stress (top) and viscosity (bottom) fields of case $Ra = 3 \times 10^7$, $\theta = 16$, $a = 0.75$, $T_0 = 0.8$. (a) $\tau_y = 6.7 \times 10^5$, (b) $\tau_y = 7 \times 10^5$, (c) $\tau_y = \infty$. Failure occurs at $\tau_y = 6.6 \times 10^5$, while the stagnant lid remains at higher τ_y. Color bars show logτ values.

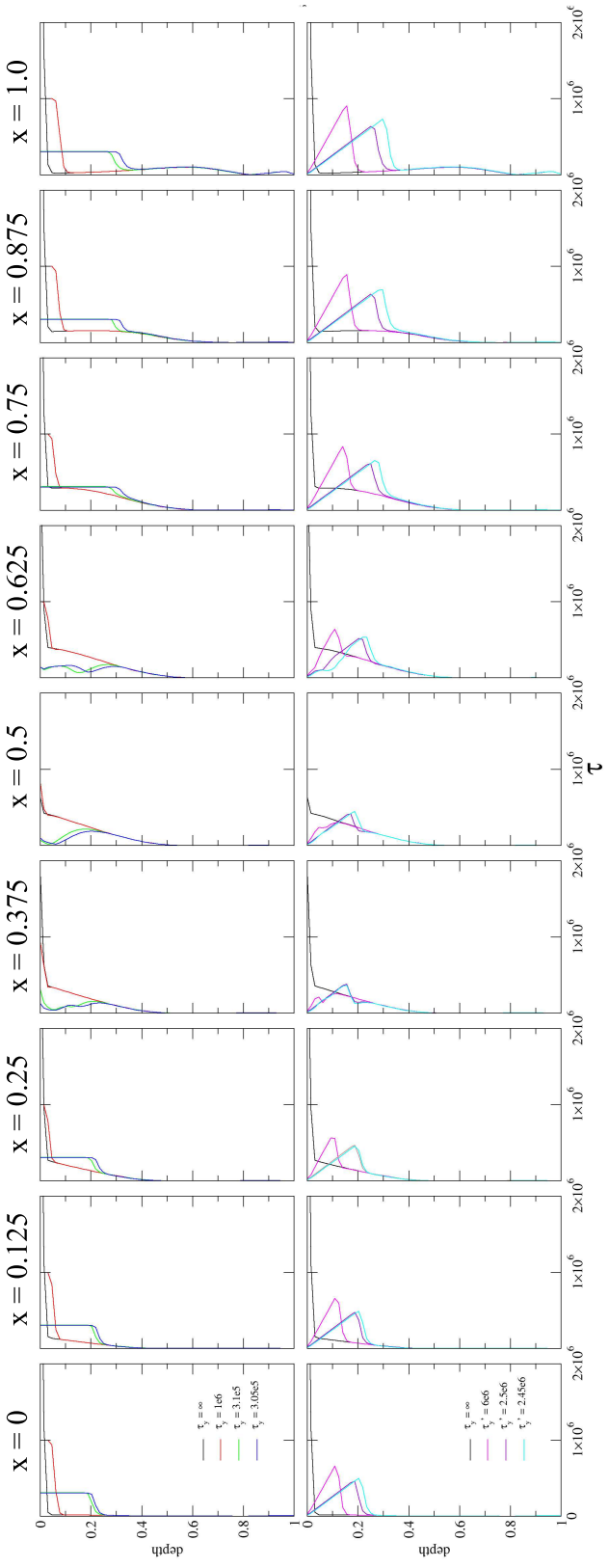

Figure 2.18 Stress profiles at different widths at various yield stress or yield stress gradient.

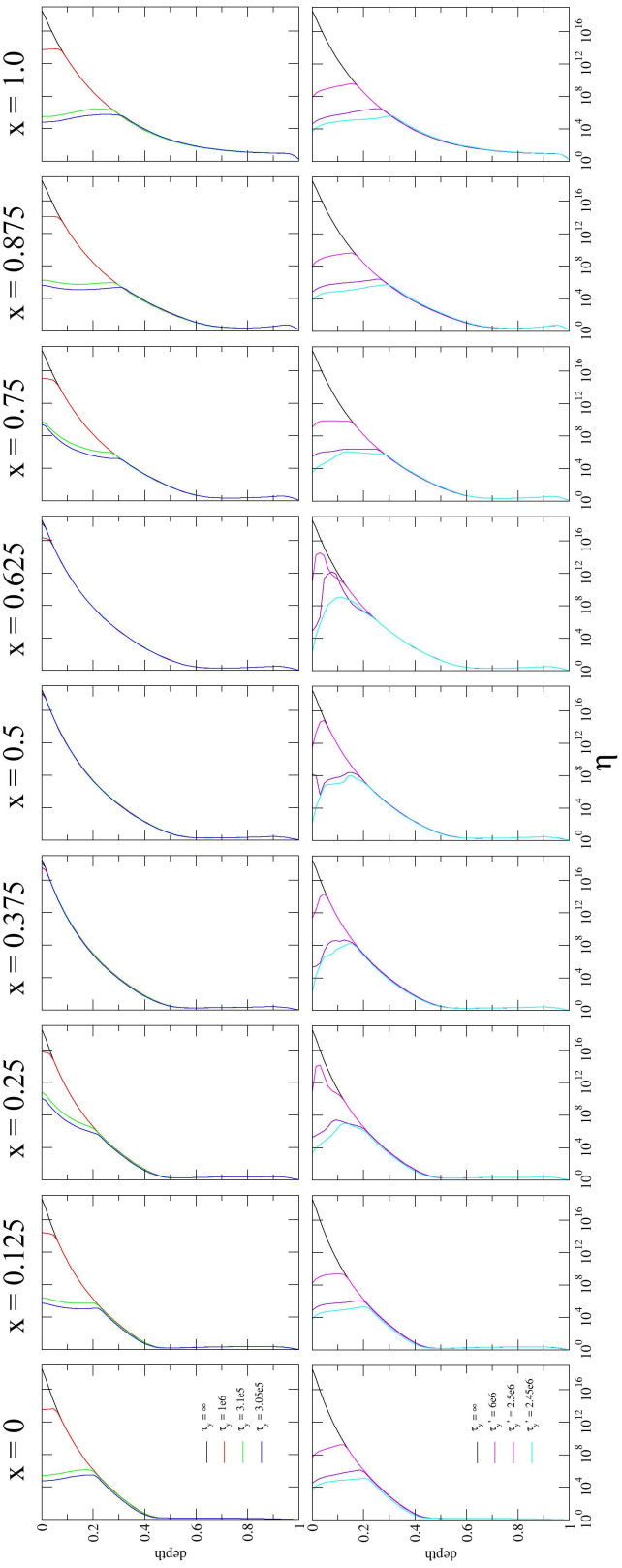

Figure 2.19 Viscosity profiles at different widths at various yield stress or yield stress gradient.

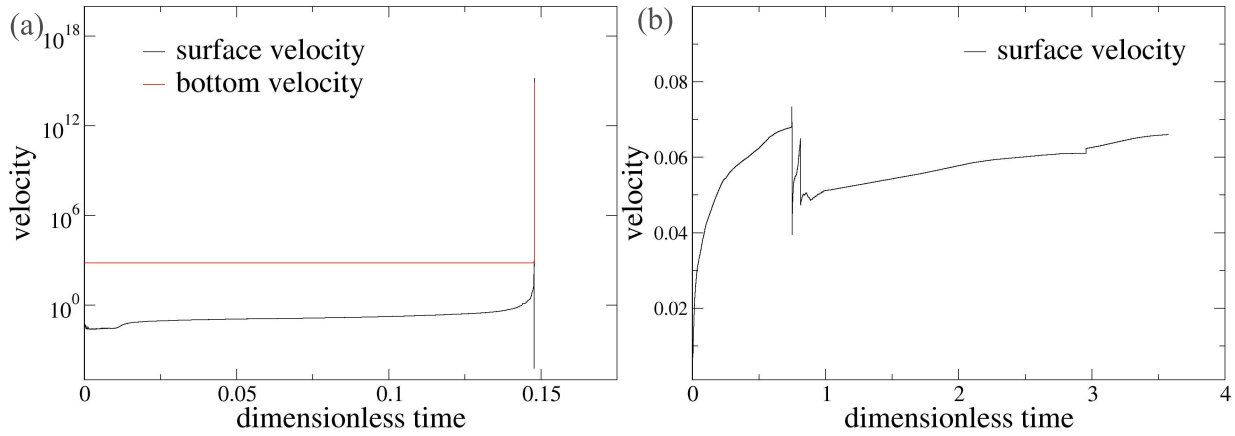

Figure 2.20 Surface velocities over time for $Ra = 3 \times 10^7$, $\theta = 16$, $a = 0.75$ (a) $T_0 = 0.8$, $\tau_y = 6.6 \times 10^5$ (b) $T_0 = 0.4$, $\tau_y = 6.1 \times 10^5$, bottom velocity ≈ 650. The surface velocity in (b) increases slowly. Although it has evolved for ~ 25 times as much as the period for (a) to fail, it is far from reaching the bottom velocity.

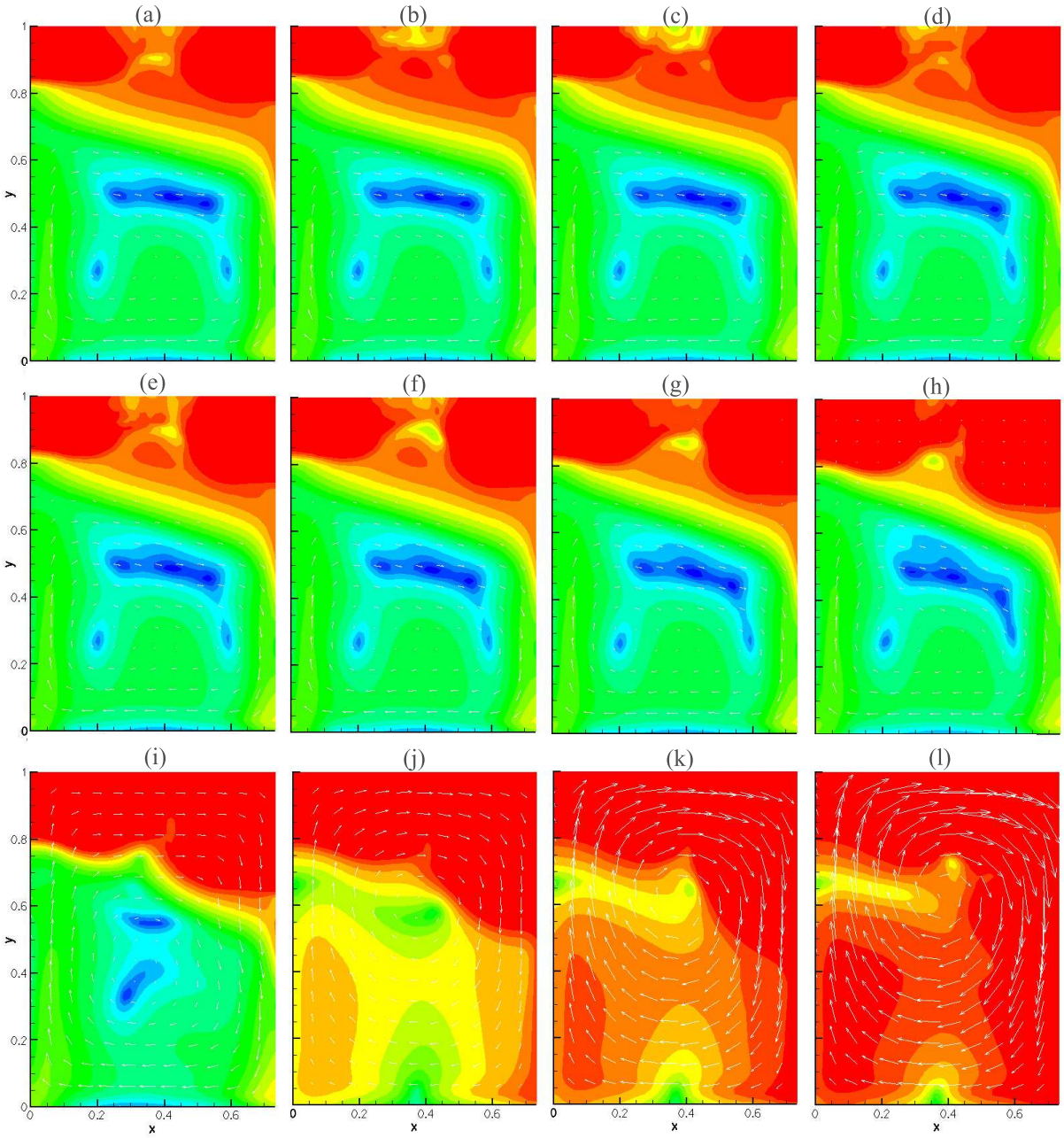

Figure 2.21 Snapshots of stress fields before and at the point of failure for case $Ra = 3 \times 10^7$, $\theta = 16$, $a = 0.75$, $T_0 = 0.8$, $\tau_y = 6.6 \times 10^5$. Time sequence goes from left to right and top to bottom. White arrows show velocities. (a) and (b) are close to beginning of simulation, (c) is at the mid-point between the start and failure, and (d) to (i) are right before overturning (depicted in (j) – (l))occurs.

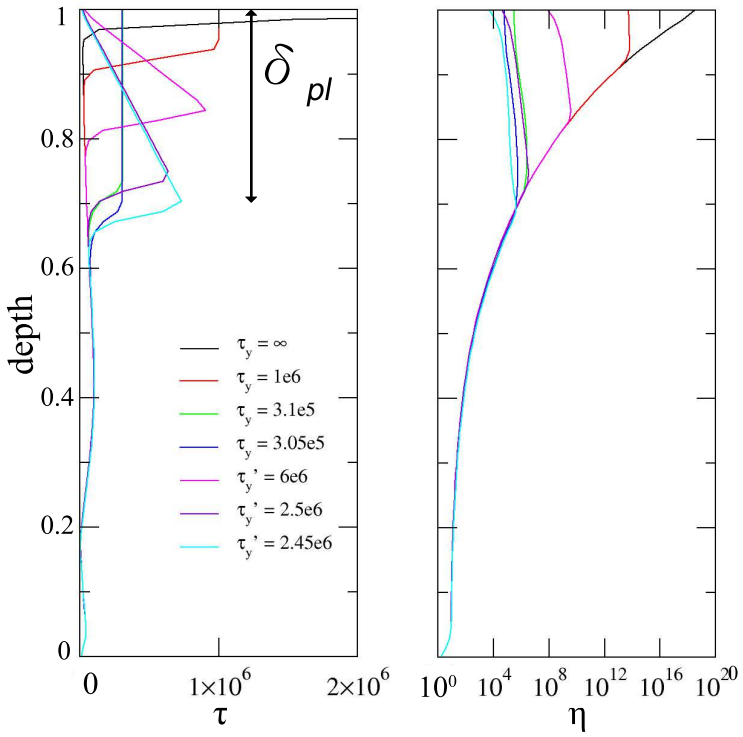

Figure 2.22 Depth of plastic zone determined by the yield stress (right), and the drop in viscosity due to the yield stress (right). Profiles taken at the downwelling edge ($x = a$) of the convecting cell.

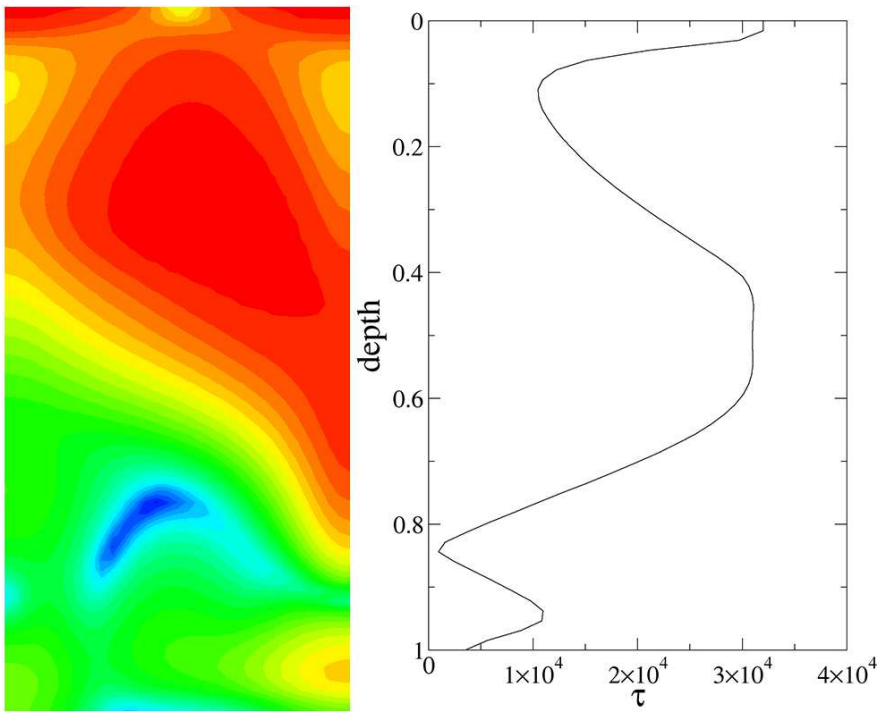

Figure 2.23 Stress field (left) and stress profile at the downwelling edge. $Ra = 3 \times 10^6$, $a = 0.5$, $\theta = 19$, $\tau_y = 3.2 \times 10^4$, exponential viscosity.

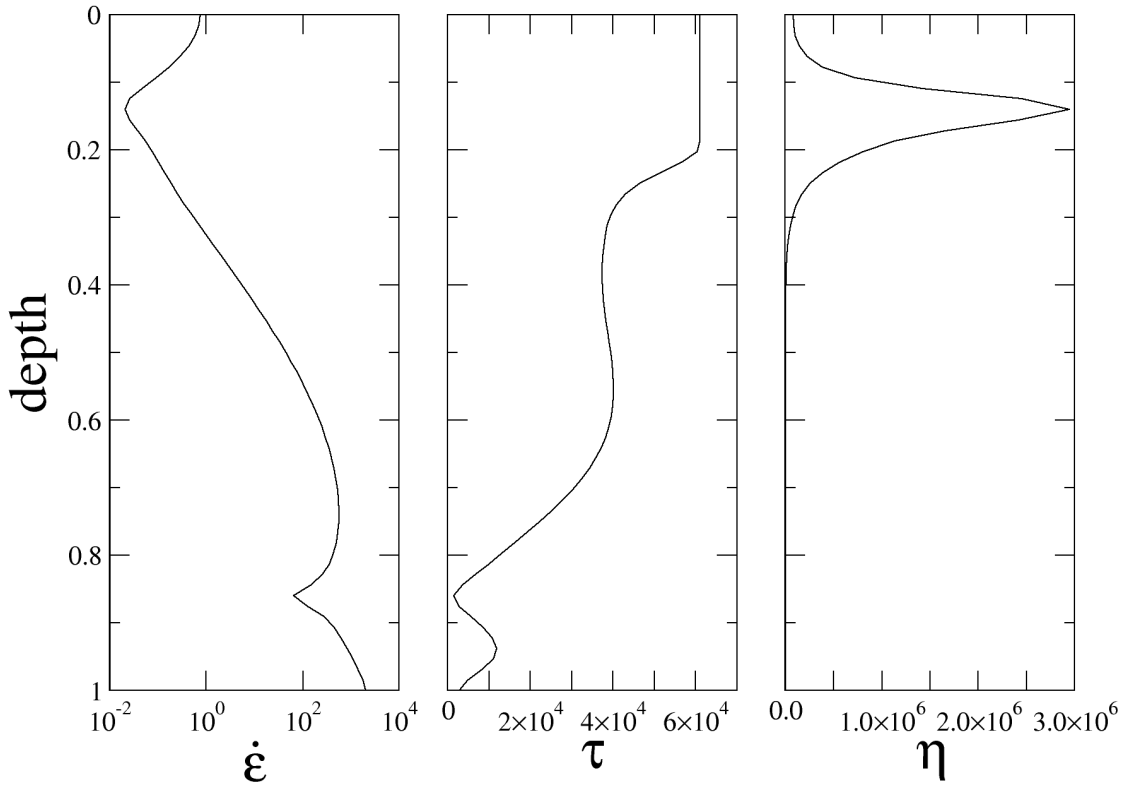

Figure 2.24 Strain rate, stress, and viscosity profile at the edge with $Ra = 3 \times 10^6$, $a = 0.75$, $\theta = 19$, exponential viscosity. The point of maximum viscosity may not correspond to the brittle-plastic transition.

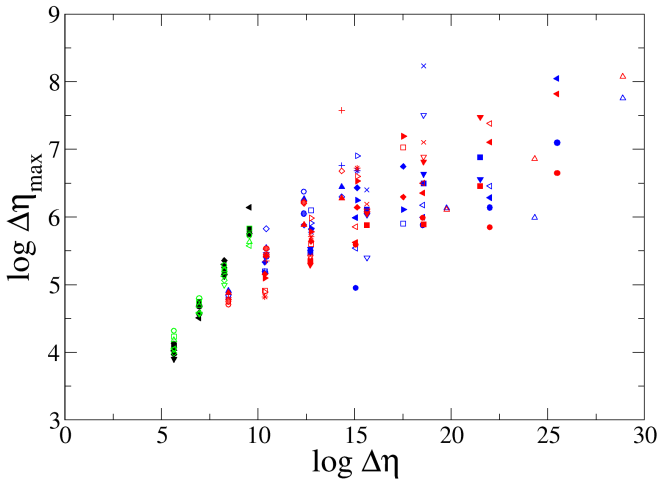

Figure 2.25 Maximum apparent viscosity in the convective cell at the point of lithospheric failure as a function of the viscosity contrast in the absence of yield stress. Black: exponential viscosity with constant $\tau_{y,cr}$; red: Arrhenius viscosity with constant $\tau_{y,cr}$; green: exponential viscosity with constant $\tau'_{y,cr}$; blue: Arrhenius viscosity with constant $\tau'_{y,cr}$.

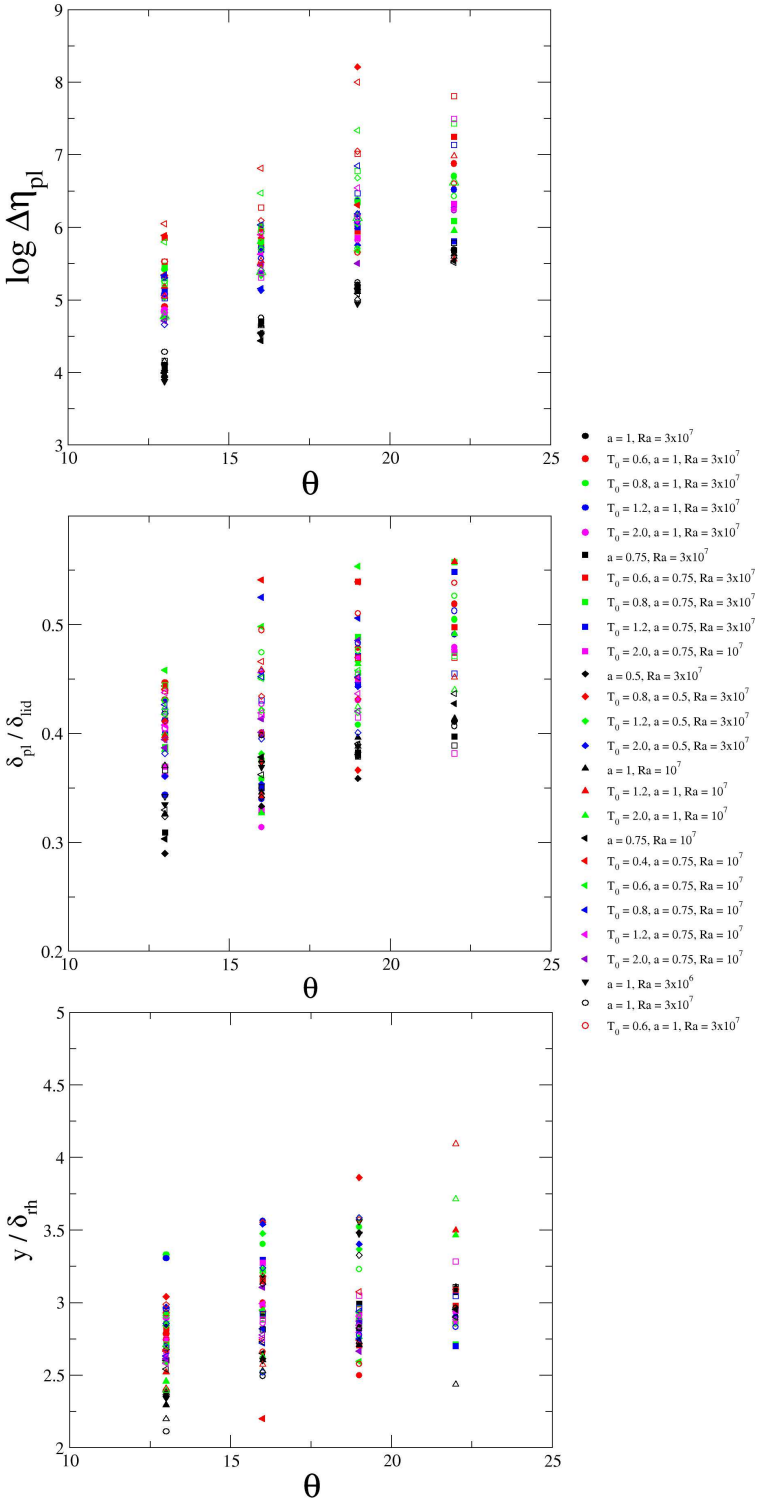

Figure 2.26 Viscosity contrast at plastic depth, fraction of lid that experience plastic failure, and the distance between the interior and plastic depth as a function of θ. Solid symbols represent constant $\tau_{y,cr}$ cases, while open symbols are constant $\tau'_{y,cr}$.

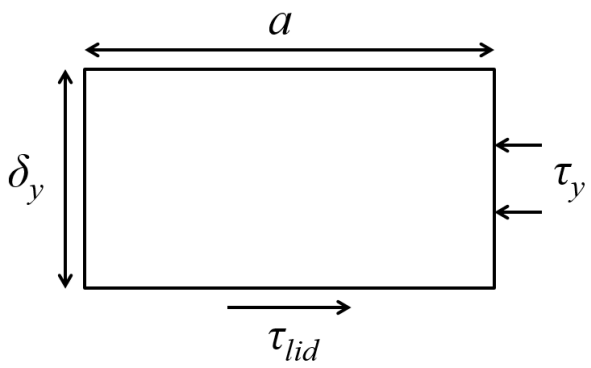

Figure 2.27 Schematic diagram of surface stresses on the plastic zone in the lid. The shear stress τ_{lid} acting on the base of the lid of horizontal length a is balanced by the normal stress τ_y acting on the side with depth δ_y, developed under free-slip boundary conditions.

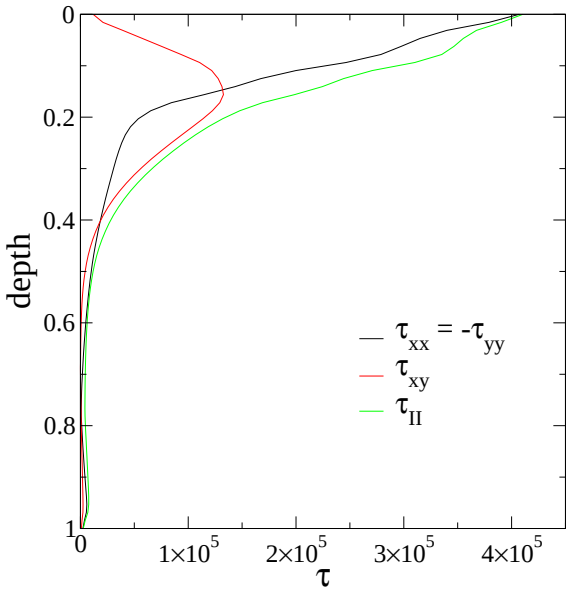

Figure 2.28 Horizontally averaged stress components and second invariant of stress as a function of depth.

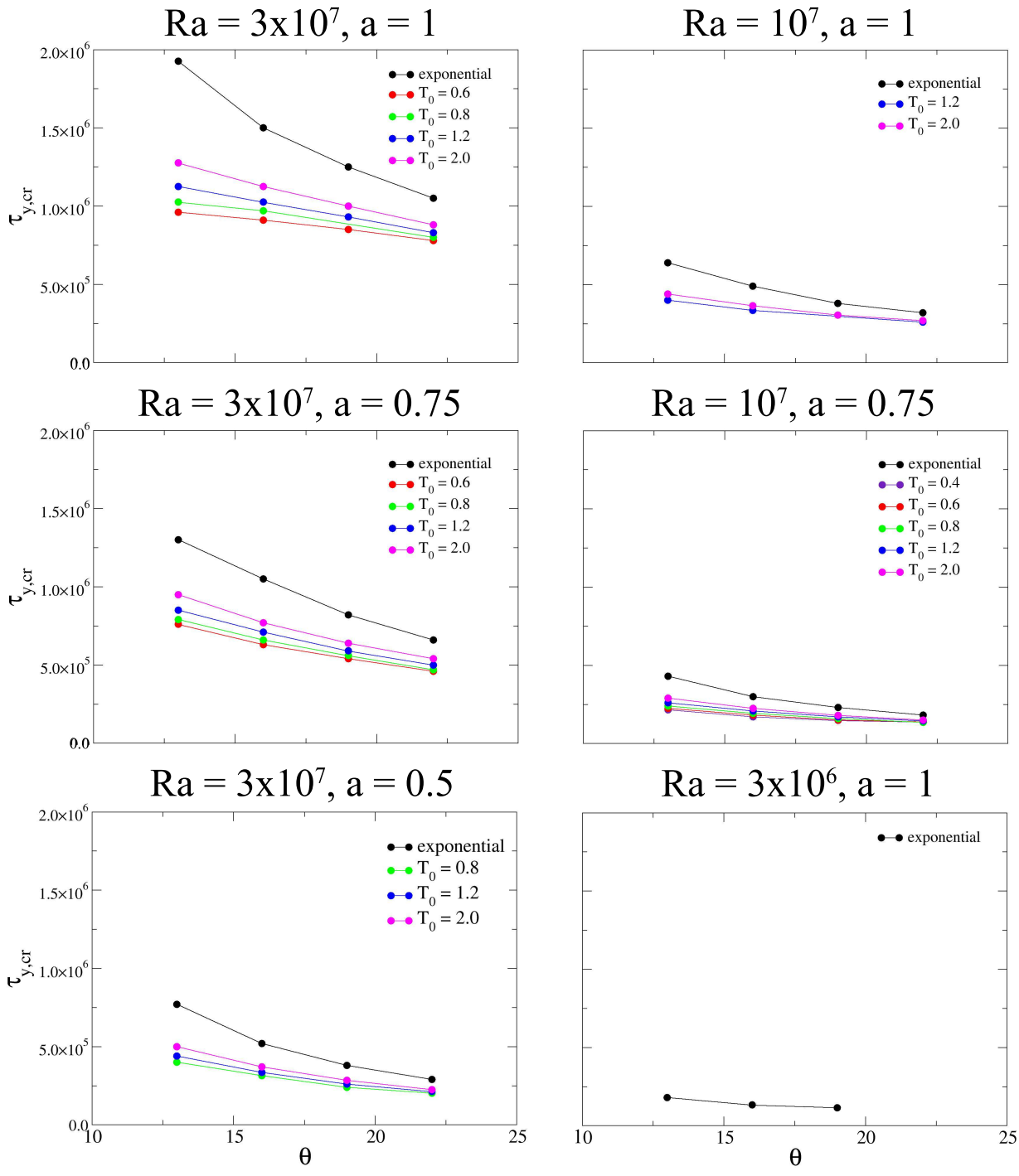

Figure 2.29 Critical yield stress $\tau_{y,cr}$ as a function of Frank-Kamenetskii parameter θ. The Arrhenius viscosity is calculated with the non-dimensional surface temperature T_0 and the activation energy E that gives the corresponding θ. Lower T_0 gives a higher viscosity contrast $\Delta\eta_{\mathrm{Arr}}$.

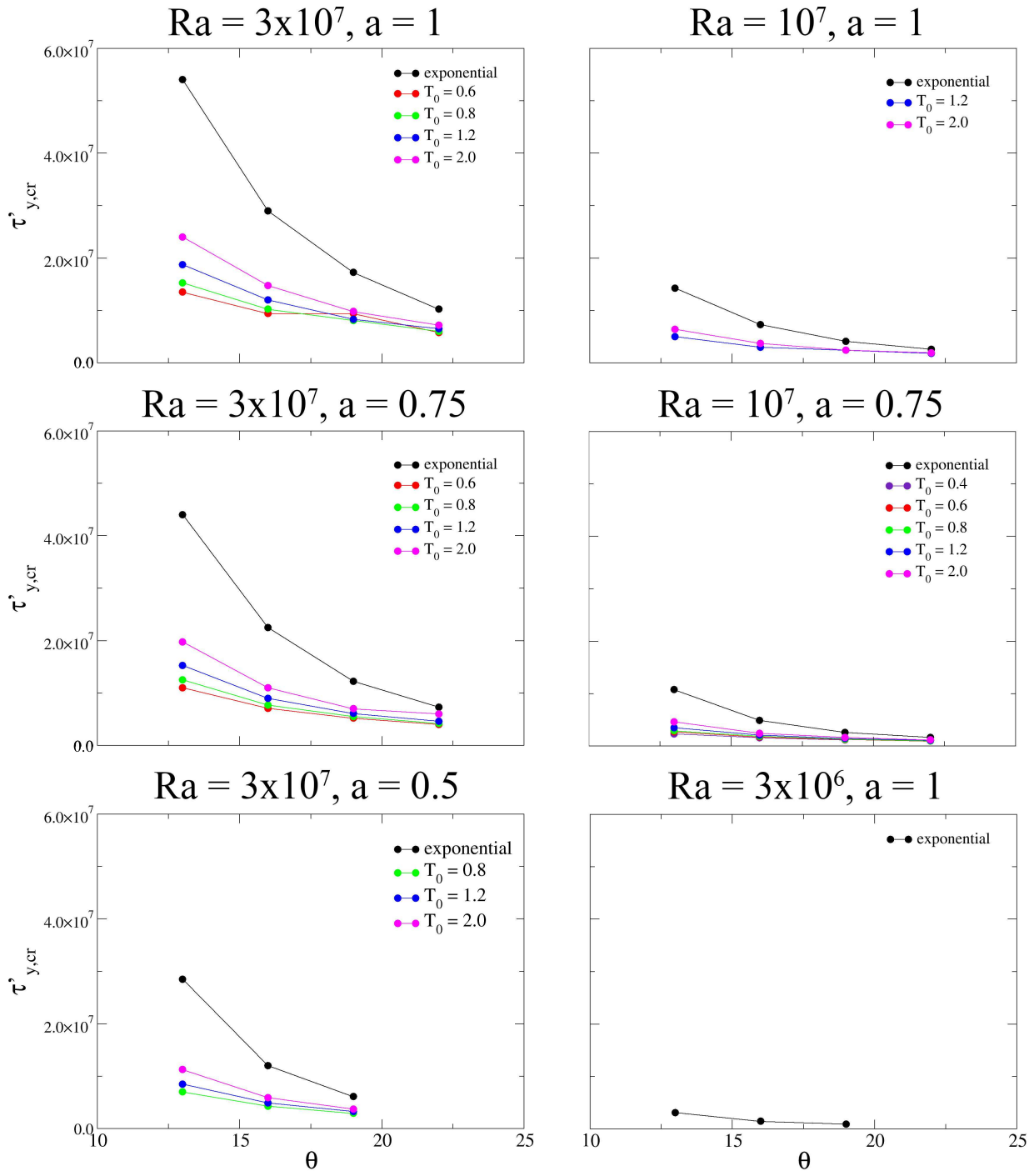

Figure 2.30 Critical yield stress gradient $\tau'_{y,cr}$ as a function of θ.

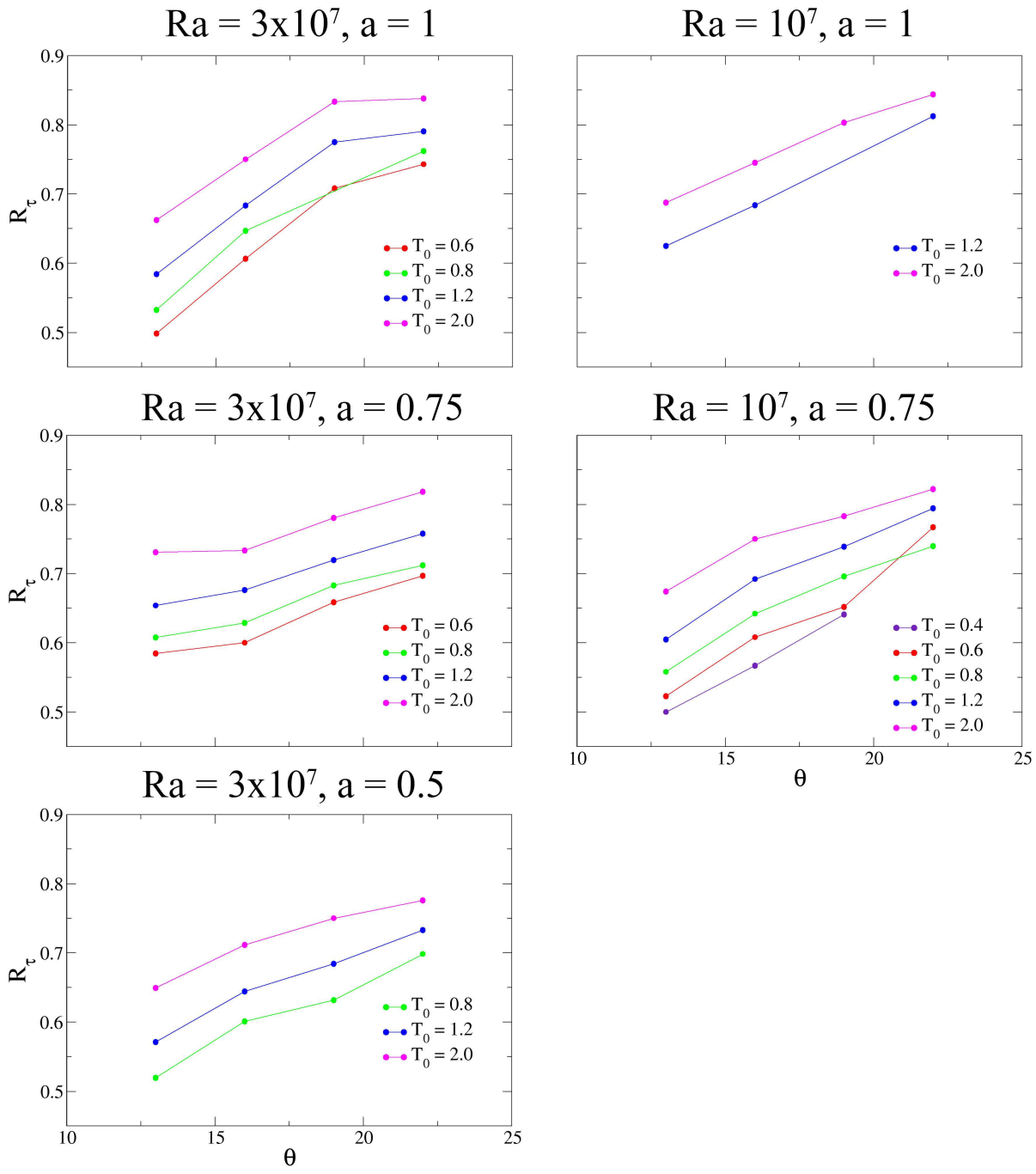

Figure 2.31 The ratio of Arrhenius yield stress to exponential yield stress R_τ as a function of Frank-Kamenetskii parameter θ.

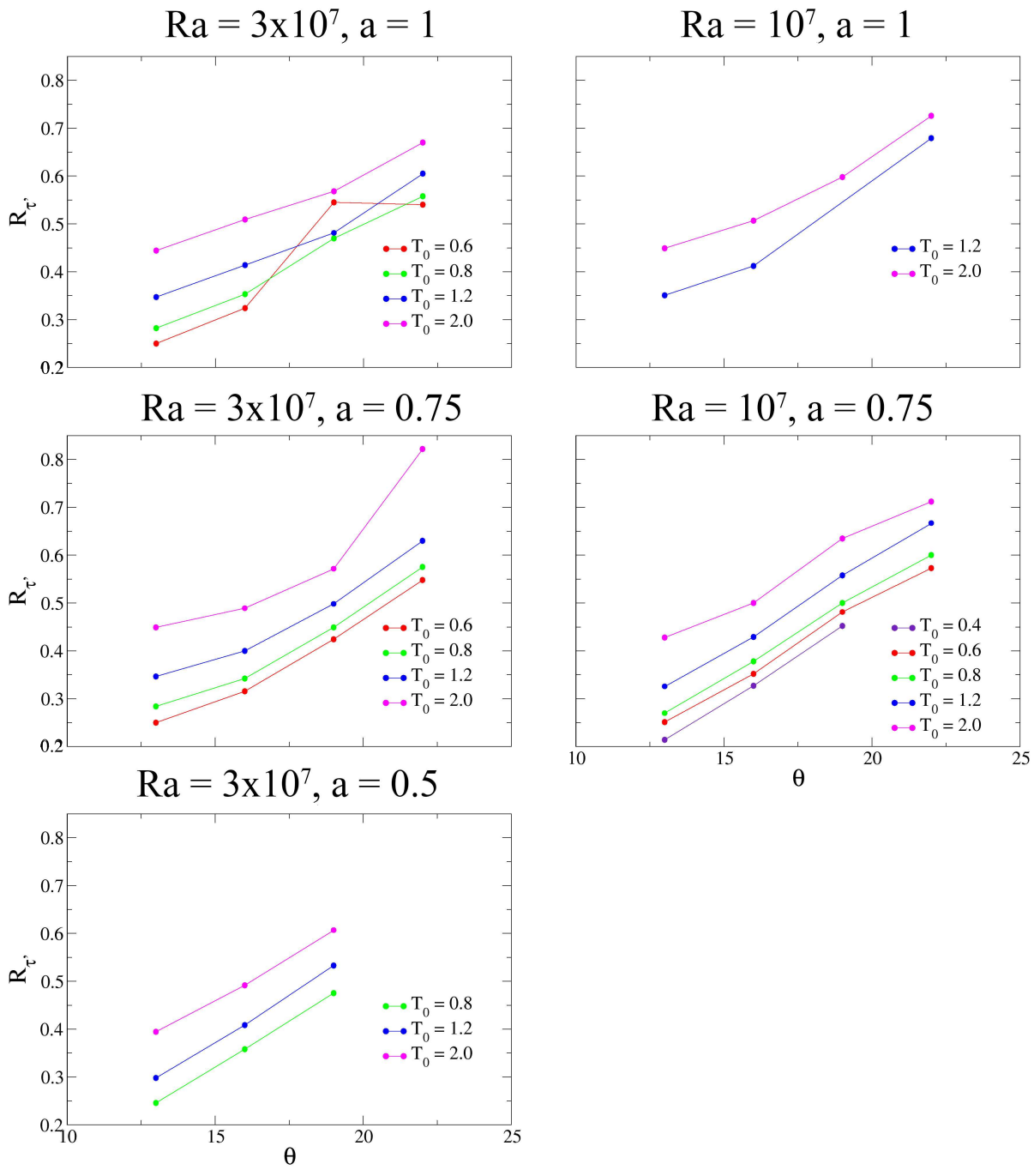

Figure 2.32 The ratio of Arrhenius yield stress gradient to exponential yield stress gradient $R_{\tau'}$ as a function of θ.

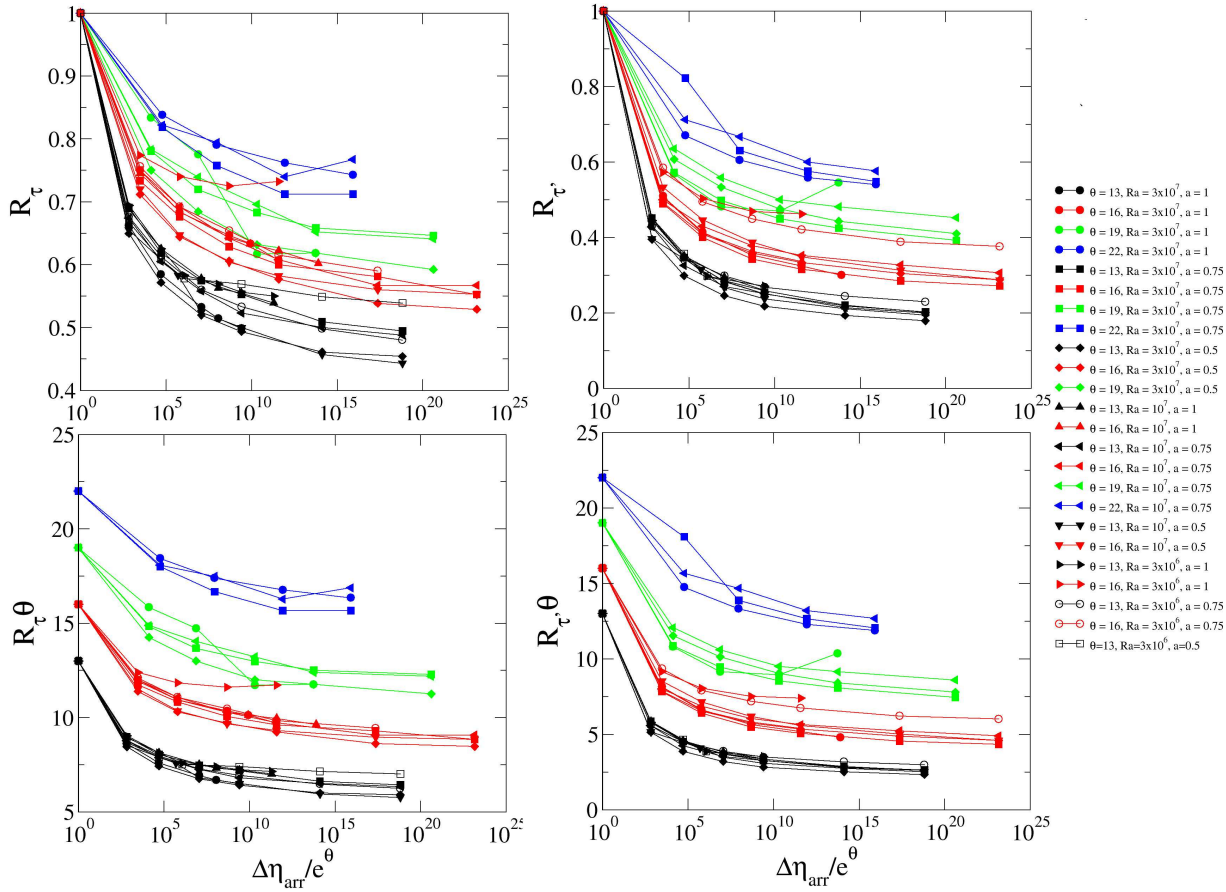

Figure 2.33 Top figures: ratio of yield stress for Arrhenius viscosity to that for exponential viscosity R_τ and $R_{\tau'}$ as a function of Arrhenius viscosity contrast normalized to exponential viscosity contrast $\Delta\eta_{\mathrm{Arr}}/\exp(\theta)$. $\Delta\eta_{\mathrm{Arr}}/\exp(\theta) \geq 1$, and it can go up to many orders of magnitude. Bottom figures: ratio of yield stress multiplied by θ. For cases with the same θ but various Ra and a, these ratios do not differ much, meaning that θ is the controlling factor for the difference in yield stress predicted by Arrhenius viscosity and exponential viscosity. Asymptotically towards high $\Delta\eta_{\mathrm{Arr}}/\exp(\theta)$, R_τ and R'_τ are approximately proportional to θ.

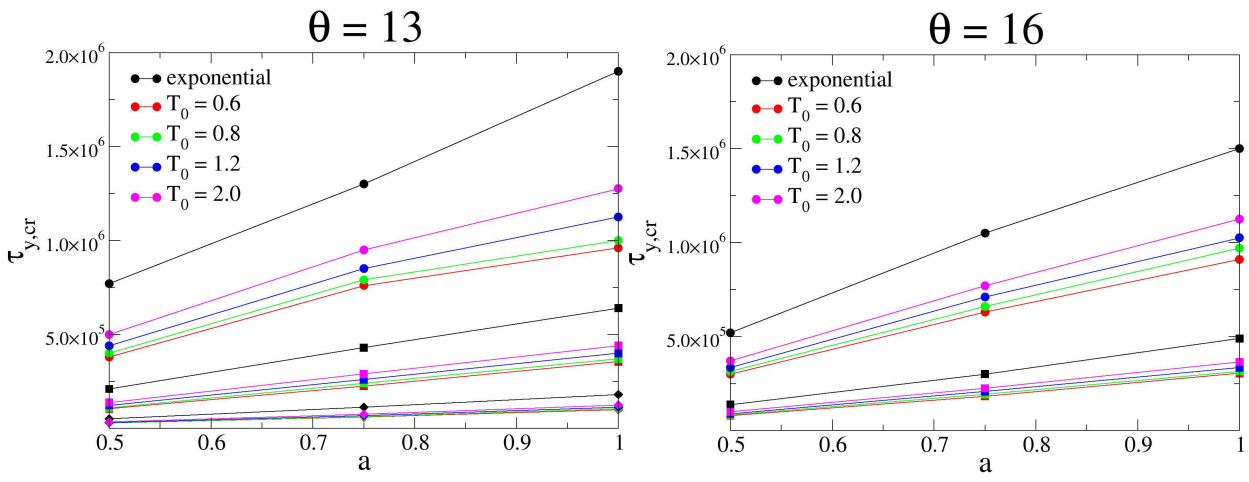

Figure 2.34 Critical yield stress $\tau_{y,cr}$ as a function of aspect ratio. Circles represent Ra=3×10^7, squares Ra=10^7, diamonds Ra=3×10^6.

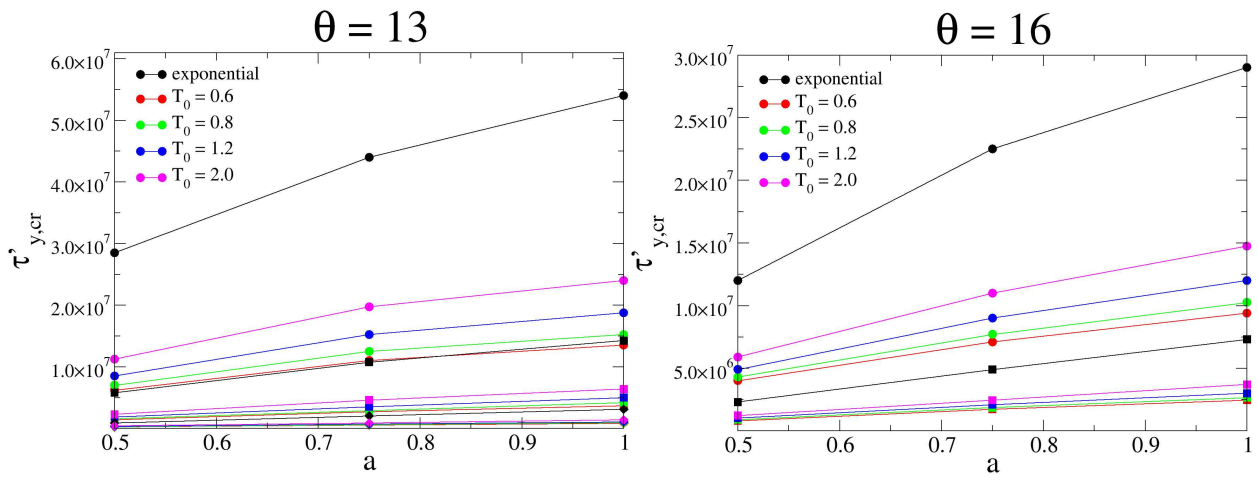

Figure 2.35 Critical yield stress gradient $\tau'_{y,cr}$ as a function of aspect ratio. Legends are the same as in Fig. 2.34.

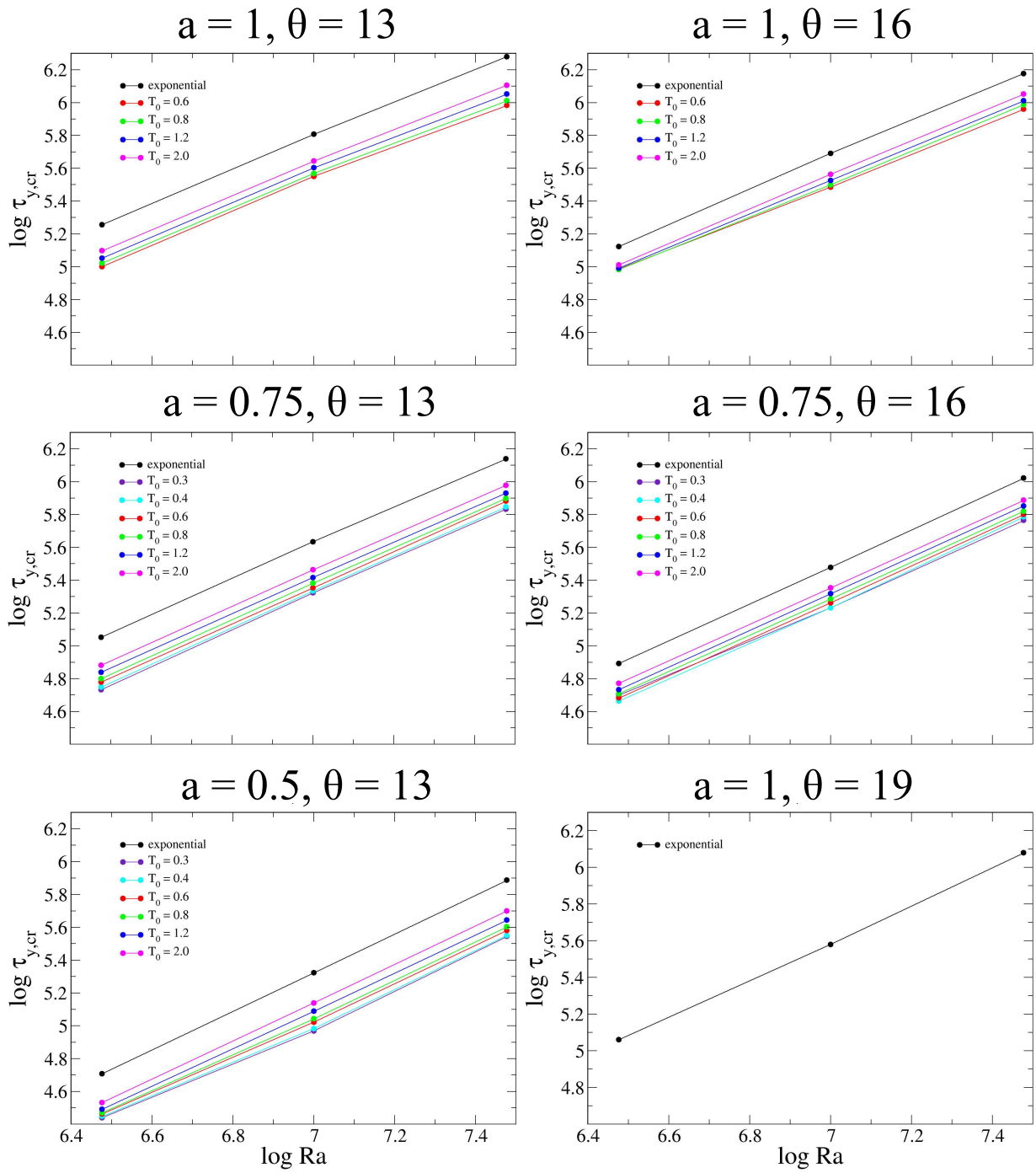

Figure 2.36 Critical yield stress $\tau_{y,cr}$ as a function of Rayleigh number.

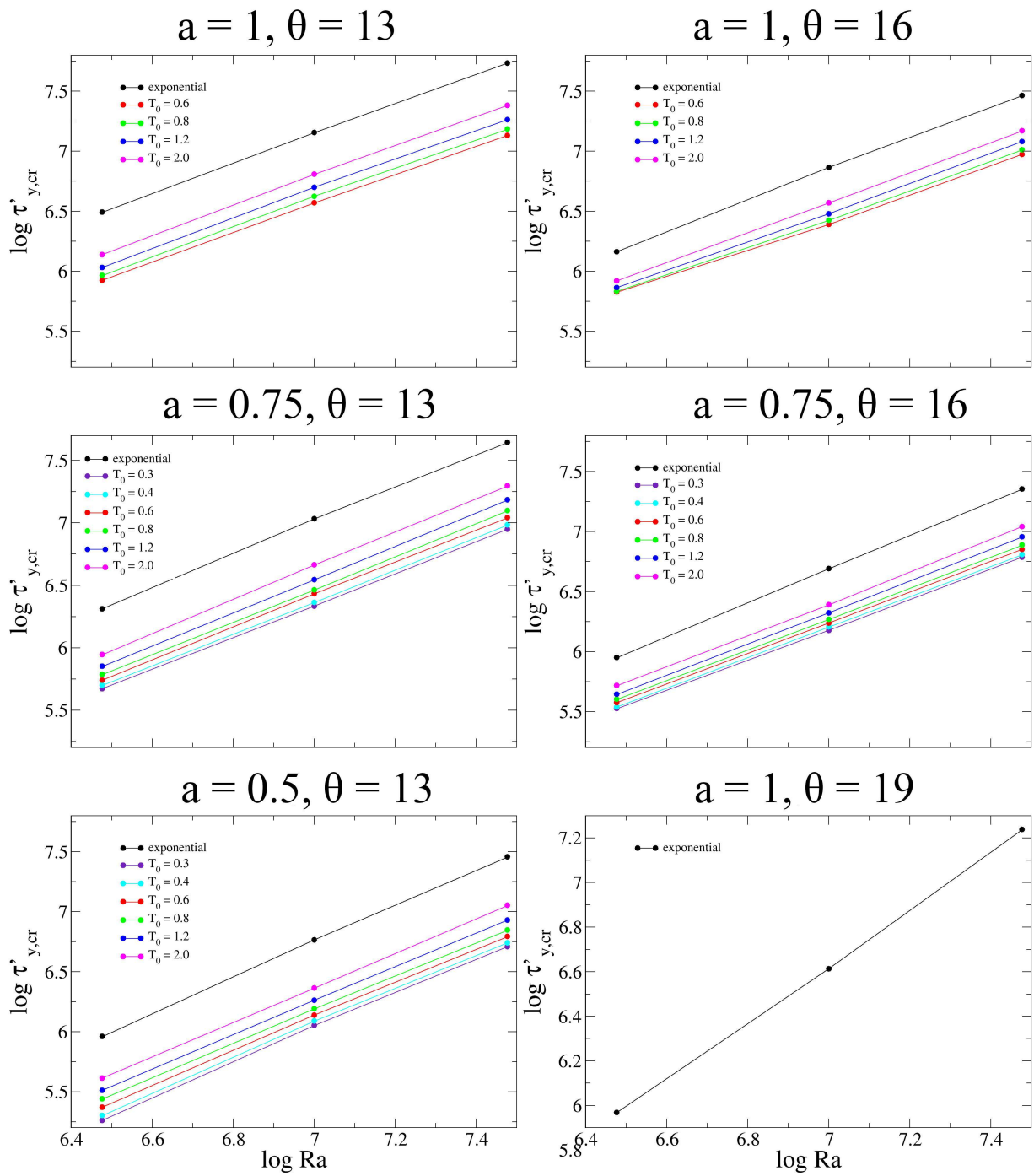

Figure 2.37 Critical yield stress gradient $\tau'_{y,cr}$ as a function of Rayleigh number.

Table 2.1 Numerical results of power law coefficients in scalings of different parameters with Ra, aspect ration a, and Frank-Kamenetskii parameter θ. $\Delta T_{rh}/\Delta T$ and $\tau_{\rm lid}$ taken at mid-width.

Parameter	c in 10^c	Ra	a	θ
Nu	0.23 ± 0.07	0.24 ± 0.01	-0.17 ± 0.03	-1.17 ± 0.05
$\Delta T_{rh}/\Delta T$	0.25 ± 0.17	0.010 ± 0.02	0.39 ± 0.08	-0.84 ± 0.12
δ_0/d	-0.26 ± 0.10	-0.22 ± 0.01	0.27 ± 0.04	1.12 ± 0.06
$\delta_{\rm lid}/d$	-0.74 ± 0.06	-0.23 ± 0.01	0.12 ± 0.03	1.44 ± 0.04
$\delta_{\rm lid,max}/d$	-0.62 ± 0.07	-0.19 ± 0.01	0.33 ± 0.03	1.26 ± 0.05
$\delta_{\rm rh}/d$	0.02 ± 0.33	-0.20 ± 0.04	0.60 ± 0.15	0.34 ± 0.21
lid slope	-0.98 ± 0.13	-0.07 ± 0.02	0.14 ± 0.06	0.63 ± 0.09
plume slope	-0.49 ± 0.39	0.15 ± 0.05	-0.01 ± 0.17	-0.31 ± 0.25
$\tau_{\rm lid}$	0.36 ± 0.21	0.68 ± 0.03	0.92 ± 0.09	-0.15 ± 0.13
$\tau_{y,cr}$	0.40 ± 0.22	1.09 ± 0.03	1.67 ± 0.10	-1.49 ± 0.14
$\tau'_{y,cr}$	2.34 ± 0.32	1.34 ± 0.04	1.45 ± 0.14	-3.47 ± 0.21

Table 2.2 Power law coefficients in scalings of different parameters with Ra, aspect ration a, and Frank-Kamenetskii parameter θ: numerical results versus theory. $\Delta T_{rh}/\Delta T$ and $\tau_{\rm lid}$ taken at mid-width.

Parameter	Ra	a	θ	Method
$\tau_{\rm lid}$	0.68 ± 0.03	0.92 ± 0.09	-0.15 ± 0.13	numerical
	0.73 ± 0.09	1.14 ± 0.29	0.146 ± 0.42	theory (in terms of $\Delta T_{rh}/\delta_{rh}$)
	0.77 ± 0.12	1.18 ± 0.39	0.14 ± 0.56	theory (in terms of Nu)
$\tau_{y,cr}$	1.09 ± 0.03	1.67 ± 0.10	-1.49 ± 0.14	numerical
	0.94 ± 0.10	1.81 ± 0.32	-1.13 ± 0.47	theory (in terms of $\Delta T_{rh}/\delta_{rh}$)
	0.97 ± 0.13	1.85 ± 0.42	-1.16 ± 0.61	theory (in terms of Nu)
$\tau'_{y,cr}$	1.34 ± 0.04	1.45 ± 0.14	-3.47 ± 0.21	numerical
	1.13 ± 0.11	1.48 ± 0.35	-2.39 ± 0.51	theory (in terms of Nu)
	1.16 ± 0.14	1.52 ± 0.45	-2.38 ± 0.65	theory (in terms of $\Delta T_{rh}/\delta_{rh}$)

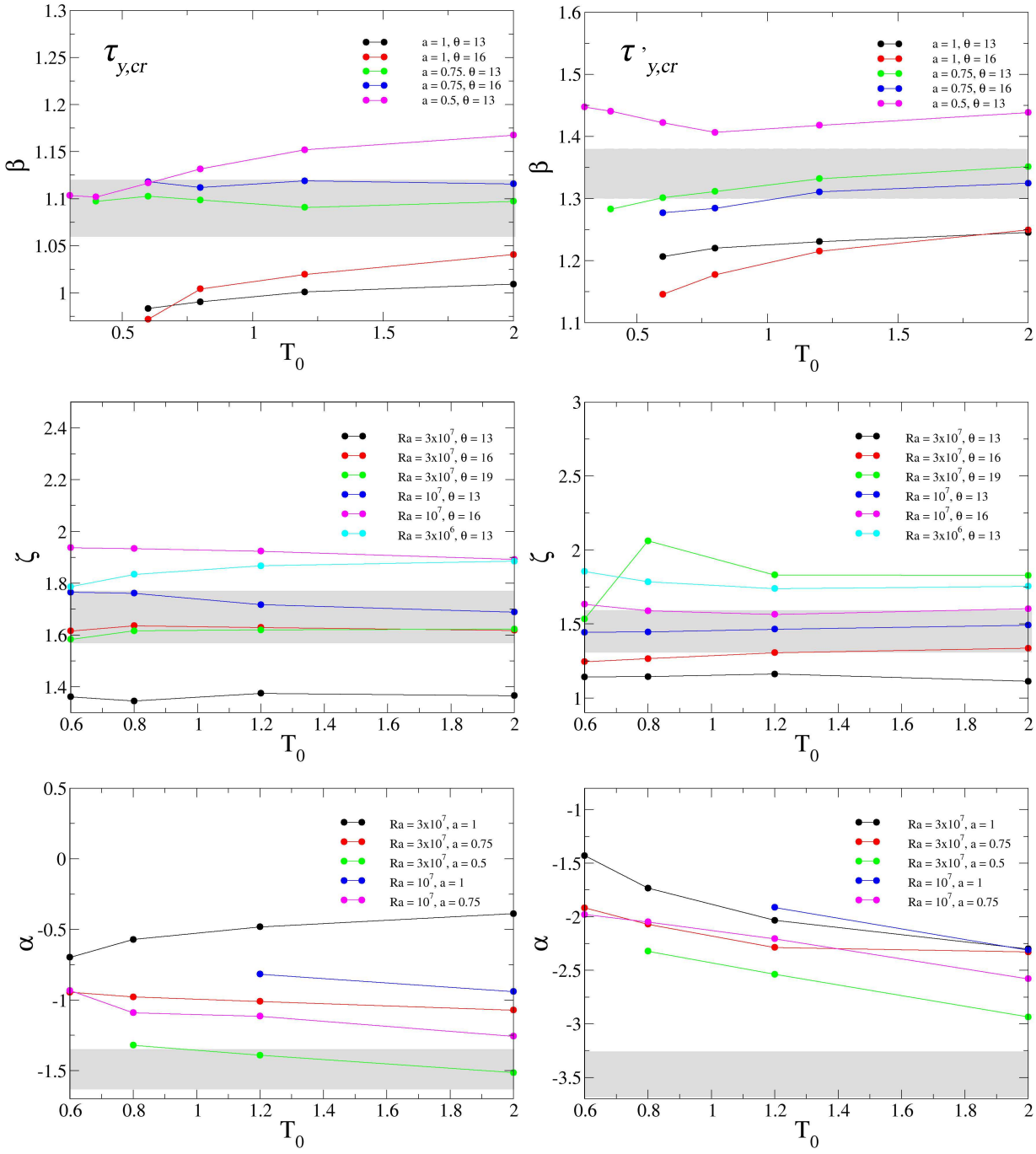

Figure 2.38 Scaling exponents in $\mathrm{Ra}^{\beta}\mathrm{a}^{\zeta}\theta^{\alpha}$ for τ_y (left 3 figures) and $\tau'_{y,cr}$ (right 3 figures) with varying T_0 in Arrhenius viscosity. The grey stripes represent the value obtained from exponential viscosity calculations, with the width determined by error bars.

Table 2.3 Parameters used to estimate $\tau_{y,cr}$ and $\tau'_{y,cr}$ for Earth as in Solomatov (2004a, b).

α	3×10^{-5}
κ	10^{-6} m^2 s^{-1}
$\delta_{\rm lid}$	100 km
k	3 W m^{-1} K^{-1}
E	430 kJ mol$^{-}1$
d	$\sim$500 km
g	10 m s^{-2}
ρ	3300 kg m^{-3}
T_0	300 K
T_i	1700 K
$l_{\rm hor}$	100 km

Chapter 3

Variations in timing of plate tectonics initiation on terrestrial planets due to chaotic nature of mantle convection

T. Wong and V. S. Solomatov

An edited version of this chapter has been submitted for publication in *Geochem. Geophys. Geosyst.* of the American Geophysical Union.

Abstract

Subduction is thought to be the fundamental process for plate tectonics initiation. One major difficulty in subduction initiation is the high viscosity of the cold top layer that prevents it from failure. The viscosity of this layer can be reduced due to a yield stress, which is a simplification of the weakening mechanisms in the lithosphere. If the yield stress is sufficiently low, stresses induced in the lid by sublithospheric convection may overcome the yield stress and cause the lid to fail. At high Rayleigh numbers, convection is strongly time-dependent and chaotic which adds a random component to the timing of subduction initiation. Even if the convective stresses in the lid are not high enough to cause subduction right away, the convective cells may evolve to a configuration in

which the lid stresses are sufficiently large to overcome the yield stress. Alternatively, subduction can be prevented by cell reconfiguration that reduces lid stresses. We inspect these fluctuations of convective flow and their effects on convective stresses. We observe that for a given set of parameters, including the yield stress, the time of lid failure is different for different statistically steady-state solutions. Some insights into what controls the timing of lid failure is gained from treating subduction as a type of Rayleigh-Taylor instability. This study suggests that it is important to address not only the question of whether plate tectonics can occur on a planet but also when it would occur if conditions are favorable.

3.1 Introduction

Plate tectonics has been recognized as the unifying theory for the geology of the Earth, yet there are still unanswered questions regarding the initiating mechanism (e.g., McKenzie 1977; Turcotte 1977; Mueller and Phillips 1991; Kemp and Stevenson 1996; Toth and Gurnis 1998; Regenauer-Lieb et al. 2001; Stern 2004; Hansen 2007; Ueda et al. 2008; Nikolaeva et al. 2010; Burov and Cloetingh 2010; Dymkova and Gerya 2013; Lu et al. 2015). The timing of its initiation is also an unresolved issue (e.g., Stern 2007; Korenaga 2013, and references therein). A major difficulty in plate tectonics initiation is the strength of the lithosphere. Due to the strongly temperature-dependent viscosity, the cold lithosphere is resistant to deformation. Many attempts have been made to quantify the yield strength of Earth's lithosphere and understanding the weakening mechanisms responsible for its magnitude (e.g., Kanamori 1994; Kohlstedt et al. 1995; Hirth and Kohlstedt 1996; Toth and Gurnis 1998; Solomatov 2004b; Bercovici and Ricard 2005).

Previous studies to simulate plate tectonics took two different approaches. One is to impose

deformation that produces plate-like behavior. This is done by applying velocity boundary conditions (Davies 1988; Lithgow-Bertelloni and Richards 1995), or by prescribing a plate structure that has weak zones (Gurnis 1988; Davies 1989; Zhong and Gurnis 1996). In this approach the plate motion or geometry are specified beforehand, and how these a priori conditions emerged is beyond the scope of this approach.

An alternative method is to adopt a rheological model that is constrained by laboratory experiments and can generate plate-like motions and features from mantle convection. This approach might allow us to address a more fundamental question of whether plate tectonics can occur in the first place. The temperature-dependent nature of viscosity results in a large viscosity towards the surface such that a thick, rigid boundary layer is developed and it does not actively participate in convection. Convection below this rigid layer occurs in the stagnant lid regime (Morris and Canright 1984; Fowler 1985; Solomatov 1995).

To mobilize the stagnant lid, a plastic yield stress can be introduced to simulate brittle and ductile failure so that subduction can occur (Fowler 1985, 1993; Trompert and Hansen 1998; Moresi and Solomatov 1998; Richards et al. 2001; Tackley 2000a,b; Fowler and O'Brien 2003; Solomatov 2004b; Stein et al. 2004; O'Neill et al. 2007; Stein and Hansen 2008). Various rheologies such as temperature-, pressure-, and grain-size dependent viscosity (Stegman et al. 2002; Stein et al. 2004; Stein and Hansen 2008; Korenaga 2010b; Bercovici and Ricard 2005; Landuyt et al. 2008) have also been explored. One limitation in these studies is that they set a relatively low viscosity contrast to observe plate behavior. The viscosity contrast used usually ranges from $\sim 10^4$–10^7 (Moresi and Solomatov 1998; Tackley 2000b; Richards et al. 2001; Stein and Hansen 2008), with the help of Frank-Kamenetskii approximation or some limiting maximum viscosities. The temperature-dependent viscosity across terrestrial lithosphere could be much higher, and in the original Arrhe-

nius form it could be tens of orders of magnitude larger. To reach an asymptotic stress distribution in the lid and obtain asymptotic scaling laws for subduction initiation, it is important that the viscosity contrasts in the lid are significantly higher than those that are barely sufficient to form the stagnant lid (which are around 10^5).

Recent models implement free-surface boundary conditions as opposed to the free-slip boundary conditions typically used in numerical studies. These models are able to simulate more realistic phenomena such as single-sided subduction (Crameri et al. 2012; Crameri and Tackley 2015). However these calculations are computationally expensive and therefore systematic analysis using free-surface boundary conditions are yet to be conducted.

Many studies aimed to understand the conditions that would be favorable for the emergence of plate tectonics. In developing a failure criterion for the lithosphere, there are mainly two ways to obtain scaling relations between various physical parameters. One is to fix a yield stress and vary the parameters of a convective system, such as Rayleigh number and viscosity contrast between the top and the bottom of the convecting layer, and find at which values of these parameters the lithosphere can be mobilized (e.g., O'Neill and Lenardic 2007). They tried to define regimes of convection such that given a combination of parameters, the occurrence of lithospheric failure could be predicted. Another approach is to treat the yield stress as a variable, and search for a critical value of yield stress for given sets of parameters in a convective system so that subduction initiation is possible (e.g., Solomatov 2004b). One reason to use the latter approach is that the yield stress is poorly constrained and is usually much lower than the value suggested by laboratory experiments. Thus, it should be treated as an unknown. Another reason is that it is much more accurate and faster to determine the conditions for lithospheric failure by varying the yield stress while keeping all other parameters constant than the other way around. From the perspective of

finding scaling laws, the two approaches are completely equivalent.

Given favorable conditions, an important question that is not systematically studied is when subduction occurs. The factors controlling the time of lithospheric failure are not well understood. Foley et al. (2014) conducted a scaling analysis for the time of subduction initiation based on damage theory and concluded that early Earth conditions permit subduction. The occurrence of subduction may also be contingent on the time evolution and the initial conditions of the convective systems, both of which are random. It is possible for convection systems with the same set of parameters or physical properties, the systems may have different flow structures due to different initial conditions, and they may evolve in different pathways such that the lithosphere may fail at different times, or failure may not happen at all. Here we investigate the variability of the timing of subduction initiation due to these random factors.

This study is organized as follows. First we summarize the results of our previous analysis on the stress distribution of the lithosphere to establish a basis for examining the stress changes in the lid over time. We then conduct numerical simulations to determine the timing of failure. We investigate the parameters that affect the time it takes for the lithosphere to become unstable, and provide a preliminary theoretical interpretation based on Rayleigh-Taylor instability model for lithospheric failure.

3.2 Governing equations and numerical methods

The equations of thermal convection in Boussinesq approximation and infinite Prandtl number are

$$\nabla \cdot \mathbf{u} = 0, \tag{3.1}$$

$$\alpha \rho g T' \mathbf{n} - \nabla p' + \nabla \times \bar{\bar{\tau}} = 0, \tag{3.2}$$

$$\frac{\partial T'}{\partial t} + \mathbf{u} \cdot \nabla T' = \kappa \nabla^2 T', \tag{3.3}$$

where $\mathbf{u}$ is the velocity vector, α is the coefficient of thermal expansion, ρ is density, g is the acceleration due to gravity and $\mathbf{n}$ is a unit vector in the direction of gravity, p' and T' are pressure and temperature perturbations, $\kappa = \frac{k}{\rho c_p}$ is the thermal diffusivity, k is the thermal conductivity, and c_p is the isobaric specific heat, and τ_{ij} is a component of the stress tensor $\bar{\bar{\tau}}$:

$$\tau_{ij} = 2\eta \dot{e}_{ij} \tag{3.4}$$

$$\dot{e} = \eta \left(\frac{\partial u_i}{\partial x_j} + \frac{\partial u_j}{\partial x_i} \right), \tag{3.5}$$

where η is the viscosity, $\dot{e}_{ij}$ is a component of the strain rate tensor, i and j are indices of the coordinate axes. The viscosity is strongly temperature-dependent and it assumes an exponential form:

$$\eta = A \exp(-\gamma T) \tag{3.6}$$

where A is a constant, and $\gamma = E/RT_i^2$, E is the activation energy, R is the gas constant, and T_i is the interior temperature. The non-dimensional form of γ is the Frank-Kamenetskii parameter:

$$\theta = \gamma \Delta T. \tag{3.7}$$

The brittle behavior of the lithosphere can be simplified with a pseudoplastic rheology (Moresi and Solomatov 1998; Trompert and Hansen 1998; Tackley 2000a; Fowler and O'Brien 2003). Viscous deformation occurs according to Eq. 3.6 when stresses are less than the yield stress τ_y. Above the yield stress, deformation follows a plastic flow law defined by an effective viscosity determined by a plastic yield stress τ_y, which is taken to be a constant in this study, and the second invariant of the strain rate tensor $\dot{e}$:

$$\eta_{\text{eff}} = \frac{\tau_y}{\dot{e}}. \tag{3.8}$$

We use the finite element code CITCOM (Moresi and Solomatov 1995) to solve Eqs. 3.1–3.3 for a 2D convection system with a fixed temperature difference $\Delta T = T_1 - T_0$ between the top and the bottom and free-slip boundary conditions. The calculations are performed with $64a \times 64$ resolution, where a is the aspect ratio.

3.3 Stress distribution in the lithosphere and critical yield stress

Although stresses in the convecting interior are low due to the warm temperatures, stresses induced in the conductive lid could be large and may be sufficient to cause large-scale lid failure (Fowler 1985). To establish a theoretical basis for the magnitude of stresses required to destabilize the lid, Wong and Solomatov (2015) considered the process of lid failure as gravitational sliding. The

concept of lid slope providing the downward force resembles the finite amplitude perturbation in McKenzie's theory, which suggested that a self-sustaining subduction requires a certain combination of the length and dip angle of the underthrusting slab (McKenzie 1977). The gravitational sliding model can also be considered as a simplification of a more sophisticated Fowler's (1985) model. In the gravitational sliding model, the lid slope that dips toward the downwelling plume provides the gravitational force that drives the lid motion. From the force balance on the lid, the lid stress is

$$\tau_{\text{lid}} = -\alpha\rho_0 g \frac{dT}{dy}\lambda\frac{y^2}{2}, \tag{3.9}$$

where ρ_0 is the reference density, λ is the slope of the lid base which is assumed to be small, and y is the vertical distance from the convecting interior towards the top of the lid (Fig. 3.1). In the non-dimensional form, τ_{lid} is a function of Rayleigh number Ra, thermal gradient dT/dy, lid slope λ and y. In the vicinity of the surface the stresses increase drastically due to huge normal stresses developed from the free-slip boundary conditions and Eq. 3.9 no longer holds.

Fowler (1985) suggested that with the introduction of a yield stress, plastic yielding occurs in the parts of the lid where the stresses are high. If the yield stress is lower, a larger part of the lid is weakened by the yield stress. If a sufficiently large part of the lid has yielded plastically, the lid can be mobilized. To determine the critical yield stress, we need to know the extent of weakening that is just necessary to destabilize the lid. This requires understanding of the stress distribution in the lid. Wong and Solomatov (2015) carried out a detailed analysis of the stresses in the lid affected by a yield stress right above the critical value, at which subduction does not occur but would have if the yield stress is slightly decreased. As the lid is stagnant at the yield stress slightly above the critical value, the dynamics of the system remains steady and so the time-dependence of

the various parameters can be neglected in the analysis.

In previous studies of failure criterion, it is often assumed that the plastically yielded depth has to extend through the bottom of the lid to initiate failure (e.g., Fowler and O'Brien 2003; van Heck and Tackley 2011). On the other hand, Solomatov (2004b) proposed that failure can occur if the lid is weakened to the point at which viscosity contrast has a critical value of $e^{4(n+1)}$, where n is the stress exponent for non-Newtonian viscosity. Wong and Solomatov (2015) found that the depth of the plastic zone $\delta_{\rm pl}$ (Fig. 3.1) does not have to reach the bottom of the lid. However the critical viscosity contrast at $\delta_{\rm pl}$ is not constant as assumed by Solomatov (2004b). It increases with the viscosity contrast due to temperature alone ($\Delta\eta_{\rm layer}$), which is related to the Frank-Kamenetskii parameter θ. It seems to converge with high $\Delta\eta_{\rm layer}$, yet no discernable scaling relationship was found. Although the failure criterion could not be defined by a certain critical viscosity contrast, $\delta_{\rm pl}$ at the critical yield stress seems to occupy 1/3–1/2 of the lid thickness.

To find out the lid stress at the plastic depth $\delta_{\rm pl}$, the distance of $\delta_{\rm pl}$ from the base of the thermal boundary layer $y_{\rm pl}$ has to be determined (Fig. 3.1). Wong and Solomatov (2015) found that at the critical yield stress, this distance is $y_{\rm pl} \approx 3\delta_{\rm rh}$, where $\delta_{\rm rh}$ is the rheological sublayer thickness.

The scaling laws for critical yield stress and critical yield stress gradient are derived by considering the force balance on the yielded plastic zone, whose extent (dictating $\delta_{\rm pl}$ and $y_{\rm pl}$) is deter-

mined by numerical solutions:

$$\begin{aligned}
\tau_{y,cr} &\approx \tau_{\mathrm{lid}}\frac{a}{\delta_{\mathrm{pl}}} \\
&\approx -\alpha\rho_0 g\frac{dT}{dy}\lambda\frac{y_{\mathrm{pl}}^2}{2}\frac{a}{\delta_{\mathrm{pl}}}, \qquad (3.10)\\
\tau'_{y,cr} &\approx \tau_{\mathrm{lid}}\frac{a}{\delta_{\mathrm{pl}}^2}1 \\
&\approx -\alpha\rho_0 g\frac{dT}{dy}\lambda\frac{y_{\mathrm{pl}}^2}{2}\frac{a}{\delta_{\mathrm{pl}}^2}. \qquad (3.11)
\end{aligned}$$

Eqs. 3.10 and 3.11 show that the critical yield stress $\tau_{y,cr}$ and the critical yield stress gradient $\tau'_{y,cr}$ depend on both the aspect ratio and the lid slope. This implies that convective cells with longer widths and steeper lid base have higher critical yield stress and yield stress gradient, and thus are more likely to initiate subduction. As other parameters in Eqs. 3.10 and 3.11 such as the thermal gradient, y_{pl}, and δ_{pl} also scale with the aspect ratio, the critical yield stress and critical yield stress gradient depend strongly on the aspect ratio.

3.4 Strongly time-dependent convection with yield stress

In the regime of higher Ra with larger aspect ratio convective boxes, the convective system is strongly time-dependent. We examine the behavior of these systems when they are subjected to a yield stress that is low enough to cause lid failure.

The snapshots in Figs. 3.2 illustrates the initiation of lithospheric failure for a statistically steady-state solution with bottom Rayleigh number $\mathrm{Ra}_1 = 3\times10^8, \Delta\eta = 10^8, a = 4$, and $\tau_y = 7\times10^6$. There are multiple regions in the stagnant lid that has reached the yield stress, indicated by the pink color in the snapshots. These yielded regions change in size as the system

evolves, and they disappear and reappear throughout the period of evolution before failure initiates. The topography of the lid base (white line in between cold blue lid and hot red interior) remains relatively stable, while both the upwelling and downwelling plumes in the interior continually fluctuate (snapshots (a)–(d) in both figures). One of the yielded regions continues to grow in size as the system approaches the time of failure, and the downwelling plume further curves the lid slope of that sub-cell (snapshots e). The downwelling plume that causes failure can be in the middle of the stagnant lid (Fig. 3.2f), or, more often, at the edge of the convective box which is forced down by the free-slip boundary condition (Fig. 3.3f).

3.4.1 Non-uniqueness of statistically steady-state solutions

For strongly time-dependent convection in long boxes, both the initial conditions and the evolution of the dynamics in the system are random factors that produce different statistically steady-state convective structures (such as those shown in Figs. 3.2 and 3.3). These structures can undergo subduction at different values of the yield stress, or subduction can happen at drastically different times.

To generate different solutions, we use different initial conditions and run the calculations until convection is statistically steady. As shown in Fig. 3.4, the lid structure and even the average lid thickness are slightly different among the solutions. We use these different statistically steady-state solutions as the starting point of simulation with yield stress.

3.4.2 Time of failure

3.4.2.1 Dependence on yield stress

Figure 3.5 shows that the time of failure seems to depend exponentially on the yield stress. Note that it is difficult to determine the exact value of the critical yield stress for strongly time-dependent cases. When the yield stress is high, there is a possibility that our simulations were not run long enough to reach lid failure. Therefore if simulations are run indefinitely, the value of the critical yield stress may be pushed higher.

3.4.2.2 Variability in the timing of subduction initiation due to non-uniqueness of convective solutions

We take one set of parameters for a convection system with bottom Rayleigh number $\mathrm{Ra}_1 = 3\times10^8$, $\Delta\eta = 10^8$, $a = 4$, and generate slightly different solutions by using different initial conditions. In each case, we allow the system to reach a statistically steady state without yield stress. Then we introduce ("turn on") a yield stress and observe how the system evolves after that. As seen from Fig. 3.5, the yield stresses and failure times vary significantly among these cases. For cases with similar times of failure, the yield stress can differ by as much as a factor of 5. This is due to variations in the lid structures among these cases, even if all these case have the same controlling parameters and all are in statistical steady states.

We compare the times of failure for convective systems with the same yield stress and other controlling parameters but corresponding to different statistically steady states. The times of failure can vary by orders of magnitude (Fig. 3.6). Thus convective systems characterized by the same controlling parameters but differing from each other because of the non-uniqueness of the solutions

give rise to a broad range of outcomes. However we can still see some systematic difference in the time of failure with different values of yield stress. As described in the previous section, for each case with the same statistically steady state, the time of failure increases with the yield stress. In other words, at lower yield stresses, more cases experience lid failure within a certain time. This can be seen from Fig. 3.6: within a dimensionless time of unity, all but one of the cases in our numerical experiment underwent lid failure at $\tau_y = 6 \times 10^6$, but only 4 of them were successful in having lid failure at $\tau_y = 9 \times 10^6$ while the rest of these cases may or may not have lid failure at longer times. Therefore the yield stress is a key controlling parameter for the probability of lid failure within a specific period of time.

Interestingly, for cases in which the yield stress is "turned on" at different times of the same statistically steady system (generated from the same initial conditions), the failure time varies randomly as well and the spread of failure times varies with yield stress. As shown in Fig. 3.7, the spread in failure time increases with τ_y. This suggests that the similar lid structure resulting from the same statistically steady system did not change much within the time range in which the yield stress was turned on. As yield stress increases, more time is needed for the lid to become unstable, which also means that the system has more time to evolve to a favorable flow configuration for subduction initiation, allowing a larger range of failure times.

3.5 Time of failure in single-cell steady-state convection

Time-dependent convection is chaotic, thus it is difficult to analyze and computationally challenging to study. To understand the factors controlling the time of failure, we examine the solutions of single-cell simulation with a fixed cell width. The flow in a single cell is better controlled and

therefore allowing a relatively simple scaling analysis. In single-cell simulations there is only one solution for the problem of subduction initiation with a fixed yield stress, as opposed to the multiple solutions with the same set of parameters in strongly time-dependent convection. These single cells can be considered as part of the multi-cell system at an instant (Fig. 3.8). The stress state of a sub-cell can be used to predict whether subduction can occur in the multi-cell system and even which part of the multi-cell system will undergo subduction.

3.5.1 Numerical results: time of failure with varying yield stress, Rayleigh number, viscosity contrast, and aspect ratio

We slowly decrease the yield stress from its critical value until the time of failure becomes comparable to the timescale of sublithospheric instabilities, the shortest characteristic time in the system.

As we reduce the yield stress below the critical value, the maximum viscosity in the lid gradually decreases and the plastic zone propagates down, until a point at which the surface velocity of the lid increases drastically indicating that the lid becomes mobile (Fig. 3.9). The maximum viscosity $\eta_{\max}$ is determined by the method described in Wong and Solomatov (2015). The glitches on the plots of $\eta_{\max}$ and depth of the plastic zone δ_{pl} with time in Fig. 3.9 are due to insufficient resolution. Throughout most of the system's evolution, the plastic zone is maintained at approximately the same depth and the maximum viscosity remains in the same order of magnitude. When $\eta_{\max}$ drops below some value, both δ_{pl} and $\eta_{\max}$ changes rapidly as the lid fails. This transitional $\eta_{\max}$, which can be estimated approximately from the sharp change in the viscosity-time plot in Fig. 3.9, differs by about an order of magnitude when the yield stress varies by about 25%. It also increases with the Frank-Kamenetskii parameter θ, which determines the viscosity contrast in the absence of the yield stress ($\Delta\eta = \exp\theta$). As the yield stress approaches the critical value, a

slight increase in yield stress gives a much longer time of failure while $\delta_{\rm pl}$ and $\eta_{\rm max}$ do not change significantly.

Figure 3.10 shows the relationships between the time of failure and the ratio of yield stress to critical yield stress $\tau_y/\tau_{y,cr}$. At a lower range of τ_y the time of failure increases approximately exponential with τ_y. When τ_y gets close to $\tau_{y,cr}$ the time of failure increases rapidly. The exponential part resembles the relationships that we observed in time-dependent calculations (Fig. 3.5. This resemblance suggest that the mechanisms controlling the time of failure are similar. Compared to the time-dependent cases in Fig. 3.5, the exponential relationship between the time of failure and yield stress is much smoother, and the rapid increase in time to infinity is clear as the ratio $\tau_y/\tau_{y,cr}$ approaches 1. The slope of these exponential curves varies with Ra, viscosity contrast, and aspect ratios. The difference is most pronounced with varying aspect ratio (right column of Fig. 3.10): the time of failure may increase by as much as an order of magnitude for the same value of $\tau_y/\tau_{y,cr}$ as the aspect ratio doubles. In contrast, an order of magnitude change in viscosity contrast (middle column of Fig. 3.10) does not cause significant change in the time of failure, and the times of failure converge as $\tau_y/\tau_{y,cr} \rightarrow 1$. Varying Ra (left column of Fig. 3.10) has still a smaller effect, changing the time of failure only slightly at higher $\tau_y/\tau_{y,cr}$. However the spread due to the variation of these parameters is not large: the difference in smaller $\tau_y/\tau_{y,cr}$ range is about an order of magnitude, and the time of failure increases towards infinity as it approaches $t = 1$ at τ_y approaching $\tau_{y,cr}$.

The fluctuations in the time-yield stress relationship in time-dependent cases in Fig. 3.5 are due to the random evolution of the lid structure such that the sub-cell with favorable properties for lid failure such as long width and large lid slope varies in location, as illustrated in Figs. 3.2 and 3.3. In other words, the sub-cell with the highest critical yield stress may switch location, whereas in

single-cell cases subduction is bound to occur at one downwelling edge. The jumps in the curves in Fig. 3.5 may correspond to a switch of the subducting sub-cell. Therefore the question of lid failure in time-dependent systems may be whether a sub-cell with high critical yield stress can be maintained for a sufficiently long time until failure initiates, and analysis of the changes in the properties of a single convective cell with time will shed light on this aspect.

Our results show that a large range of time of failure is possible ($\sim 10^{-3}$–1) and that the transition from instantaneous subduction to no subduction occurs over a small range of τ_y: below approximately 1/2 $\tau_{y,cr}$, subduction occurs immediately after the yield stress is "turned on", and above $\tau_{y,cr}$ it does not occur.

3.5.2 Model for lithospheric instability

To interpret the numerical results, we consider the subduction process as a Rayleigh-Taylor instability. Canright and Morris (1993) considered Rayleigh-Taylor instability of two layers with different viscosities, which can be approximately applied to subduction initiation. During subduction, thermal diffusion is unimportant because it is too slow compared to the subducting plate and thus subduction is akin to the Rayleigh-Taylor instability in a chemically stratified layer. We approximate the convective system by a two-layer model: a cold, dense layer lying on top of a hot convecting interior, each having a characteristic viscosity (Fig. 3.11a). The timescale of the growth of the instability is:

$$t_s = \frac{1}{\tilde{s}} \frac{\eta_{\text{eff}}}{\Delta\rho g \delta_{\text{lid}}}, \tag{3.12}$$

where η_{eff} is the effective viscosity of the top layer, and $\tilde{s}$ is the non-dimensional growth rate.

Since the density difference between the two layers is driven by temperature, the top layer

is defined by the isotherm of the bottom of the lid, using the method described in Wong and Solomatov (2015). The lid includes both the plastic zone and the parts below which deform by the creep flow law. The yield stress reduces the viscosity within the lid, with a maximum at around $\delta_{\rm pl}$ (Fig. 3.1), causing the greatest viscosity contrast with η_i. We take this maximum viscosity to be the effective viscosity $\eta_{\rm eff}$ of the lid.

The growth rate $\tilde{s}$ depends on the regime of Rayleigh-Taylor instability (Fig. 3.11b). The controlling parameters are the viscosity contrast between the top and bottom layers $\Delta\eta = \eta_{\rm eff}/\eta_i$, the ratio of the depth of the interior to the lid thickness $\beta = (d - \delta_{\rm lid})/\delta_{\rm lid}$, and the normalized wavenumber K which depends on the perturbation wavelength λ_p as $K = 2(2\pi/\lambda_p)\delta_{\rm lid}$. In our single-cell steady-state cases, the lid slope dips towards the downwelling edge so the lid thickness varies laterally. At large θ and small Rayleigh numbers, $\delta_{\rm lid}$ is comparable to the depth of the interior. We take the average $\delta_{\rm lid}$, which is approximately the lid thickness at the middle of the cell. It ranges from around 0.2 to around 0.5, so β is around 4 and approaches 1 as lid thickness approaches 0.5. The range of viscosity contrast is determined by $\eta_{\rm eff}$, which is taken to be $\sim 10^4$–10^6 (Fig. 3.9). The perturbation wavelength in our cases is twice the width of the cell (a = 0.5 to 1). This gives K on the order of 10 to 100. For $\beta \to 1$, $K \to \beta^{\infty}$ and $(\Delta\eta)^{-1} \to \beta^{-\infty}$, placing our cases in the regime of $\tilde{s} = 1/K$ (the shaded area in Fig. 3.11b). In the limit of very thin thermal boundary layer and large viscosity contrasts, which may be more relevant to planetary conditions, $\beta \gg 1$ and $K < 1$, thus $\tilde{s}$ can be in the regime of $\tilde{s} = 1/4$.

We can relate the effective viscosity $\eta_{\rm eff}$ in Eq. 3.12 to the yield stress. The yield stress determines the depth of the plastic zone from the force balance $\delta_{\rm pl}\tau_y \sim a\tau_{\rm lid}$. The effective viscosity $\eta_{\rm eff}$ is given by the temperature at this depth $T_{\rm eff}$, which can be found from the thermal gradient

dT/dy:

$$\begin{aligned} T_{\text{eff}} &= \frac{dT}{dy}\delta_{\text{pl}} \\ &= \frac{dT}{dy}a\frac{\tau_{\text{lid}}}{\tau_y}. \end{aligned}$$

Eq. 3.12 thus becomes

$$\begin{aligned} t_s &= \frac{1}{\tilde{s}}\frac{\exp(-\gamma T_{\text{eff}})}{\Delta\rho g\delta_{\text{lid}}} \\ &= \frac{1}{\tilde{s}}\frac{1}{\Delta\rho g\delta_{\text{lid}}}\exp\left(-\gamma\frac{dT}{dy}a\frac{\tau_{\text{lid}}}{\tau_y}\right). \end{aligned} \tag{3.13}$$

In addition, there must exist a critical effective viscosity η_{cr} such that $t_s \to \infty$ when $\eta \to \eta_{\text{cr}}$. Thus we introduce a threshold term for η_{cr} to Eq. 3.12:

$$t_s = \frac{1}{\Delta\rho g\delta_{\text{lid}}\tilde{s}}\left(\frac{1}{\eta_{\text{eff}}} - \frac{1}{\eta_{\text{cr}}}\right)^{-1}. \tag{3.14}$$

The non-dimensional form of Eq. 3.14 is:

$$t_s = \frac{1}{\text{Ra}_0\delta_{\text{lid}}\tilde{s}}[\exp(\theta T_{\text{eff}}) - \exp(\theta T_{\text{cr}})]^{-1}, \tag{3.15}$$

where Ra_0 is the surface Rayleigh number and δ_{lid} in this equation is non-dimensionalized by the depth of convecting layer d. The temperature at η_{eff} is related to the depth of the plastic zone.

Expressing the ratio $\tau_y/\tau_{y,cr}$ as $R_{\tau_{\text{cr}}}$, the temperature at η_{eff} is:

$$T_{\text{eff}} = \frac{dT}{dy}a\frac{\tau_{\text{lid}}}{\tau_{y,cr}}R_{\tau_{\text{cr}}}^{-1}. \tag{3.16}$$

Eq. 3.15 can be rewritten to relate the timescale of instability growth and $R_{\tau_{cr}}$ by grouping all the other terms, noting that Nu is the non-dimensional form of dT/dy:

$$t_s = C[\exp(C' R_{\tau_{\rm cr}}^{-1}) - \exp C']^{-1}, \tag{3.17}$$

$$C = \frac{1}{{\rm Ra}_0 \delta_{\rm lid} \tilde{s}}, \tag{3.18}$$

$$C' = \theta {\rm Nu} a \frac{\tau_{\rm lid}}{\tau_{y,cr}}. \tag{3.19}$$

Note that C and C' are not constants for several reasons: (1) The lid thickness $\delta_{\rm lid}$ (and thus Nu which scales as $\sim \delta_{\rm lid}^{-1}$) is not an independent variable. It depends on convective parameters and can be expressed with some power law relationships with Ra, viscosity contrast, and aspect ratio (Wong and Solomatov 2015). If $\tilde{s}$ is in the 1/4 regime, both C and C' depend on $\delta_{\rm lid}$; in the $1/K$ regime, C could be independent of $\delta_{\rm lid}$, but Nu remains in C'. (2) The lid stress $\tau_{\rm lid}$ refers to the shear stress at the plastic depth $\delta_{\rm pl}$ as a consequence of force balance on the plastic zone, and this may vary in a complex way in the lid depending on $\delta_{\rm pl}$. As mentioned in the previous section, $\delta_{\rm pl}$ is roughly at a distance $y_{\rm pl} \approx 3\delta_{\rm rh}$ from the interior at the critical yield stress. However for τ_y not too close to $\tau_{y,cr}$, as shown in Fig. 3.9, $\delta_{\rm lid}$ changes by ~50% with a ~25% variation in τ_y. Also as $\tau_{\rm lid} \sim y_{\rm pl}^2$, and $y_{\rm pl}$ changes with $\delta_{\rm pl}$, $\tau_{\rm lid}$ may be a function of τ_y. Since $\tau_{\rm lid}$ is inside the exponent, even a small variation in $\tau_{\rm lid}$ may lead to a great change in C', which is the slope of the exponential curve. This may also explain why the aspect ratio changes the slope of these exponential curves substantially as $\tau_{\rm lid}$ depends on the aspect ratio. A complete scaling law with C and C' would be too cumbersome as each of these coefficients depends on several factors, and a small error would result in a huge difference especially with C' inside the exponent. Interestingly the spread in time of failure is relatively small, suggesting that extrapolating to planetary conditions from these curves

would yield estimates that are not far from the numerically established range.

To see how well Eq. 3.17 describes the evolution of lithospheric failure, we apply this equation to one case with $\mathrm{Ra}_1 = 10^7$, $a = 1$, and $\theta = 19$. Fig. 3.12 shows that the values of C and C' determined from the fit are close to the values of C and C' estimated directly from Eqs. 3.18 and 3.19. For this case, $\beta \approx 1.4$, $(\Delta\eta)^{-1} = e^{-19} \approx 10^{-8}$, and $K = 2\pi\delta_{\mathrm{lid}} \approx 2.6$. Therefore it is in the regime of $\tilde{s} = 1/K$, and $C = 36$. Nu can be found from numerical results and it is ≈ 2 until the instant when failure occurs. The lid stress τ_{lid} in this case may be tricky to estimate because of the range of yield stress and therefore different δ_{pl} and y_{pl}. From the curve fitting in Fig. 3.12 $\tau_{\mathrm{lid}}/\tau_{y,cr}$ is about 1/6. From the force balance $\tau_{\mathrm{lid}}/\tau_{y,cr} \sim \delta_{\mathrm{pl}}/\delta_{\mathrm{lid}} \approx 0.4$, which is on the same order. Thus Rayleigh-Taylor instability seems to be an appropriate interpretation of lithospheric failure.

3.6 Conclusions

Due to the variability in time-dependent convection solutions, a large range of subduction time is possible for a given set of parameters of a convective system. In time-dependent convection, which is chaotic in nature, the behavior of the convective system depends on the initial conditions, such that systems with the same convective parameters and yield stress may experience lithospheric failure at different times during their evolution. We found that for a given set of parameters with the same yield stress but different convective solutions, the time of failure can vary by several orders of magnitude. Thus the time of subduction initiation is a stochastic property controlled by initial conditions and tiny variations in the convective system. The analytical solutions of Rayleigh-Taylor provide an explanation for the relationship between the yield stress and the time of lithospheric failure. The problem of subduction and thus plate tectonics initiation is not only whether the

lithosphere has a sufficiently low yield strength, but also whether lithospheric failure would occur on a geologic time scale.

More work needs to be done to understand the timing of plate tectonics initiation. While pseudoplastic rheology has been successful at producing lithospheric failure with plate-like behavior, it is often criticized for not being able to record the history of weakening as the materials are weakened instantaneously when the yield stress is applied. Both physical and numerical models of subduction evolution demonstrated that subduction zone could initiate on pre-existing weak zones, suggesting that the memory of deformation can be a key factor of the process (e.g., Shemenda 1992; Gurnis et al. 2000). To model with history-dependent deformation, Tackley (2000b) employed a strain weakening rheology, and Bercovici and colleagues developed the damage theory that captures changes in rheology from energy considerations (Bercovici et al. 2001; Bercovici and Ricard 2005; Landuyt et al. 2008; Bercovici and Ricard 2012). These models were able to produce plate-like behaviors with localized weak zones that resemble plate boundaries. Perhaps a connection between the yield stress simplification and more complicated rheologies such as the one described by the damage theory would be the variation of yield stress with time. The history-dependent nature of deformation may be expressed as a time-dependent yield stress, as it has been shown that the evolution pathway of the yield stress influences the regimes of convection (Lenardic and Crowley 2012; Weller and Lenardic 2012). The analysis using constant yield stress or yield stress gradient can constrain the time required for the lithosphere to be sufficiently destabilized. The yield stress approach in combination with theories that captures the inheritance of deformation will be able to give a better understanding of stress state and weakening mechanisms in the lithosphere.

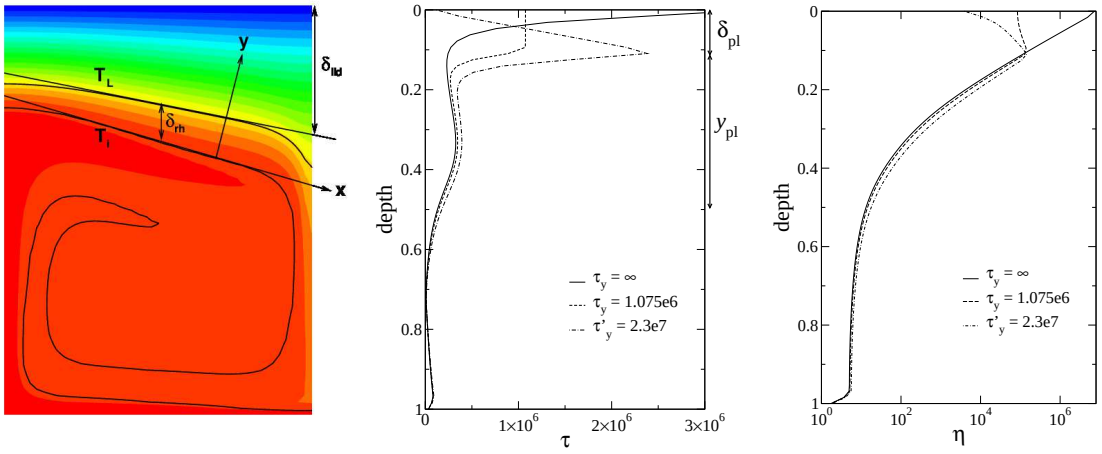

Figure 3.1 Left: Thermal structure of a steady-state convective cell (red is hot, blue is cold); y is the vertical distance from the bottom of the thermal boundary layer. Middle: depth of plastic zone $\delta_{\rm pl}$ and y at this depth ($y_{\rm pl}$) determined by the yield stress at the downwelling edge ($x = a$) of the convecting cell. Right: the corresponding viscosity profile. The viscosity is limited by the yield stress such that there is a maximum value at approximately $\delta_{\rm pl}$.

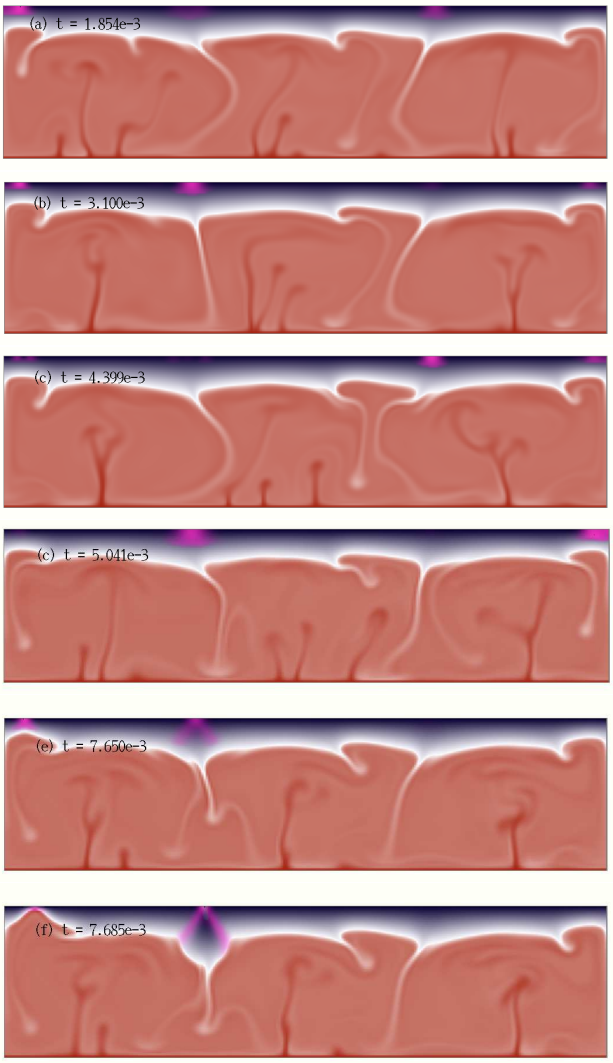

Figure 3.2 Snapshots for the case $\mathrm{Ra}_1 = 3 \times 10^8$, $a = 4$, $\Delta\eta = 10^8$, $\tau_y = 7 \times 10^6$. Pink color represents yielded areas. The time on the figures are dimensionless.

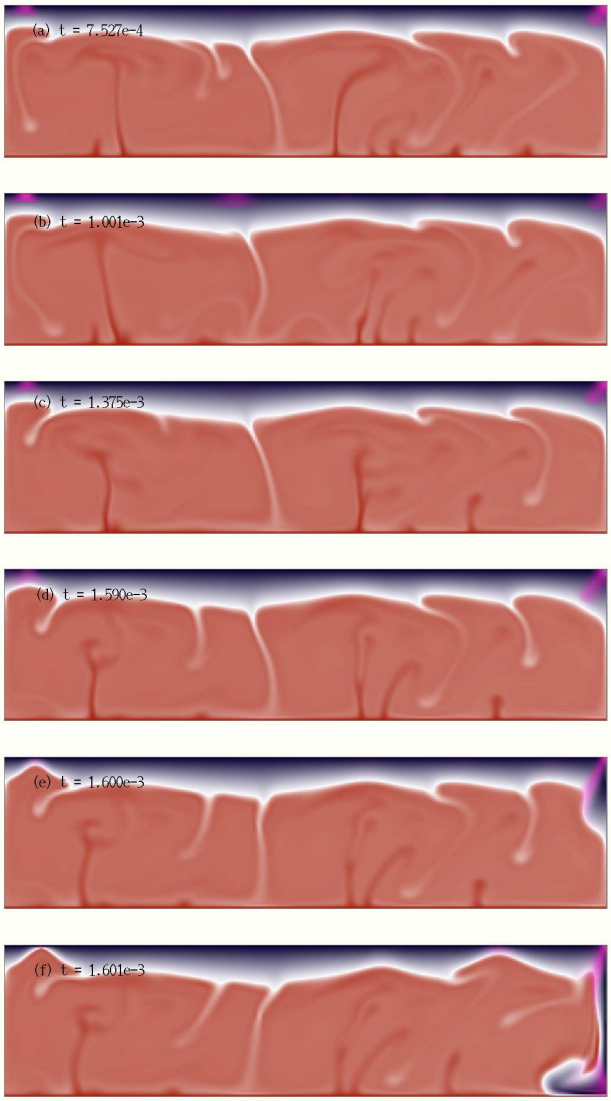

Figure 3.3 Snapshots for the case $\mathrm{Ra}_1 = 3 \times 10^8$, $a = 4$, $\Delta\eta = 10^8$, $\tau_y = 7 \times 10^6$. Note that although the parameters are the same as in Fig. 3.2, the convective solution is different.

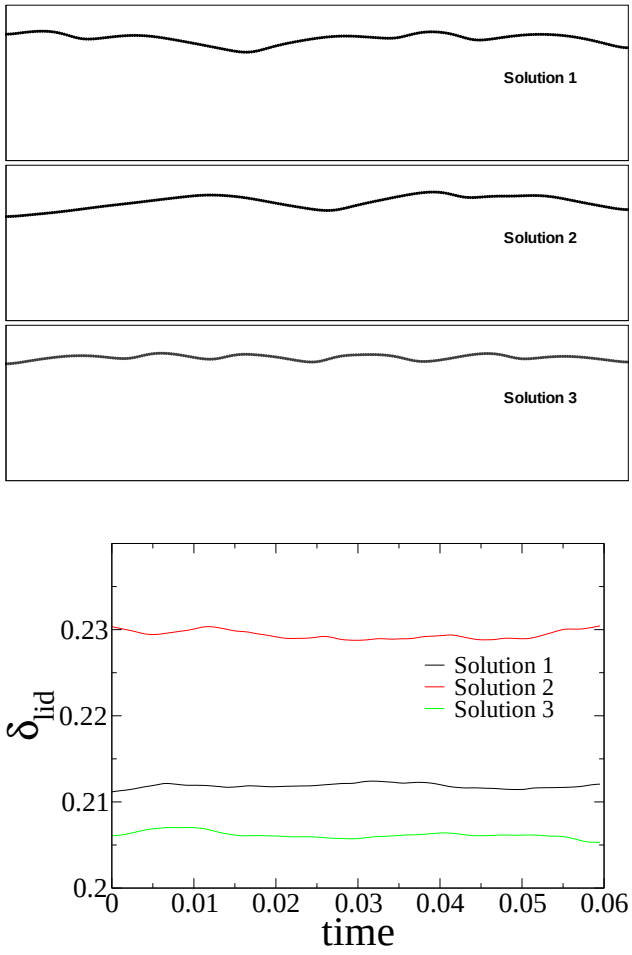

Figure 3.4 Topography of the lid base for different solutions corresponding to the same set of controlling parameters ($\mathrm{Ra}_1 = 3 \times 10^8$, $\Delta\eta = 10^8$, $a = 4$). The lid base is inferred from surface heat flow variations horizontally. Bottom graph: average lid thickness over time. The lid thickness is relatively steady with time.

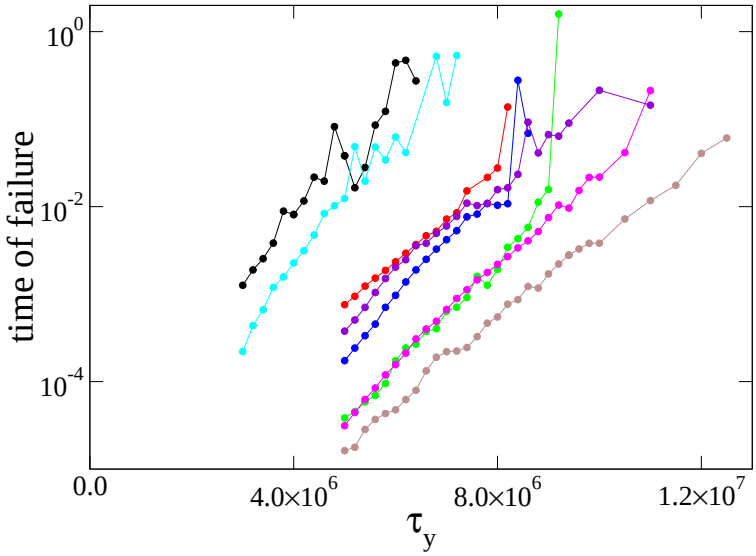

Figure 3.5 Time of failure as a function of yield stress for different convective solutions (represented by different colors) corresponding to $\mathrm{Ra}_1 = 3 \times 10^8$, $\Delta\eta = 10^8$, $a = 4$.

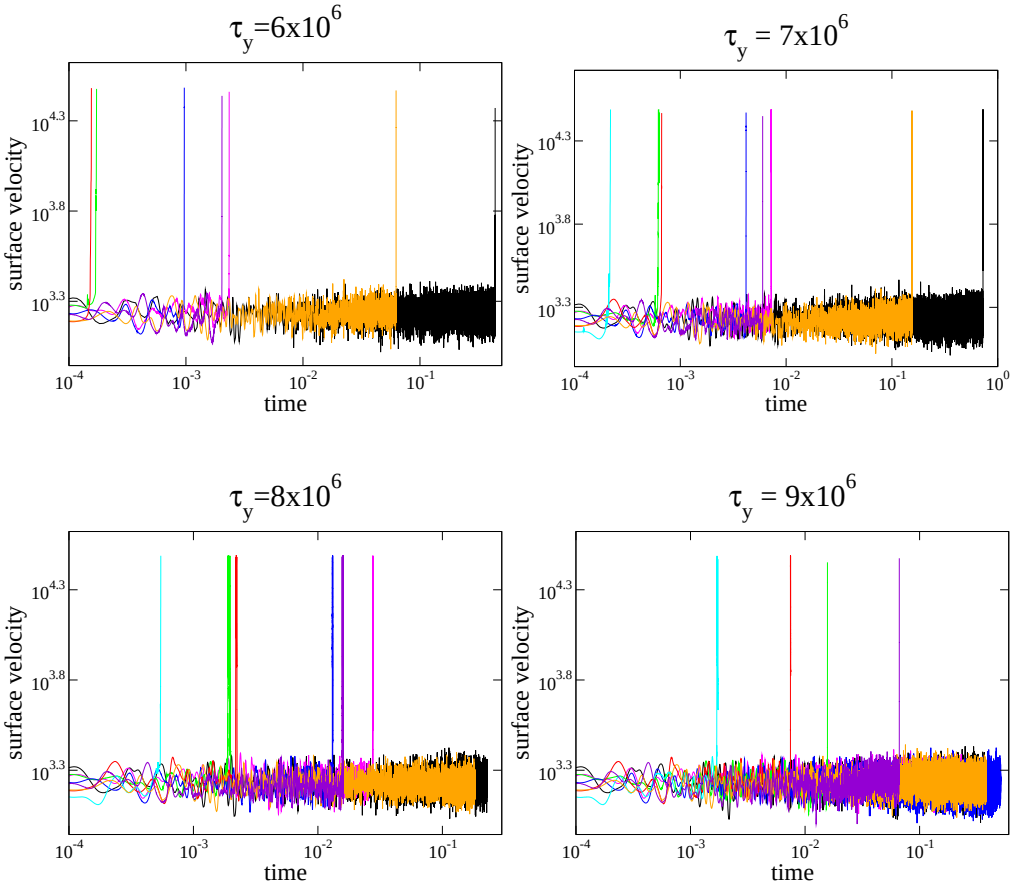

Figure 3.6 The spread in the time of failure for the cases with the same yield stress and other controlling parameters ($\mathrm{Ra}_1 = 3 \times 10^8$, $a = 4$, $\Delta\eta = 10^8$) but different convective solutions represented by different colors. The spikes in surface velocity means that the lithosphere is no longer stable and starts to move, which indicates the initiation of lid failure. For the cases which do not show the velocity spikes, failure did not happen within the simulation runtime, which could be continued for longer period with the possibility of observing failure.

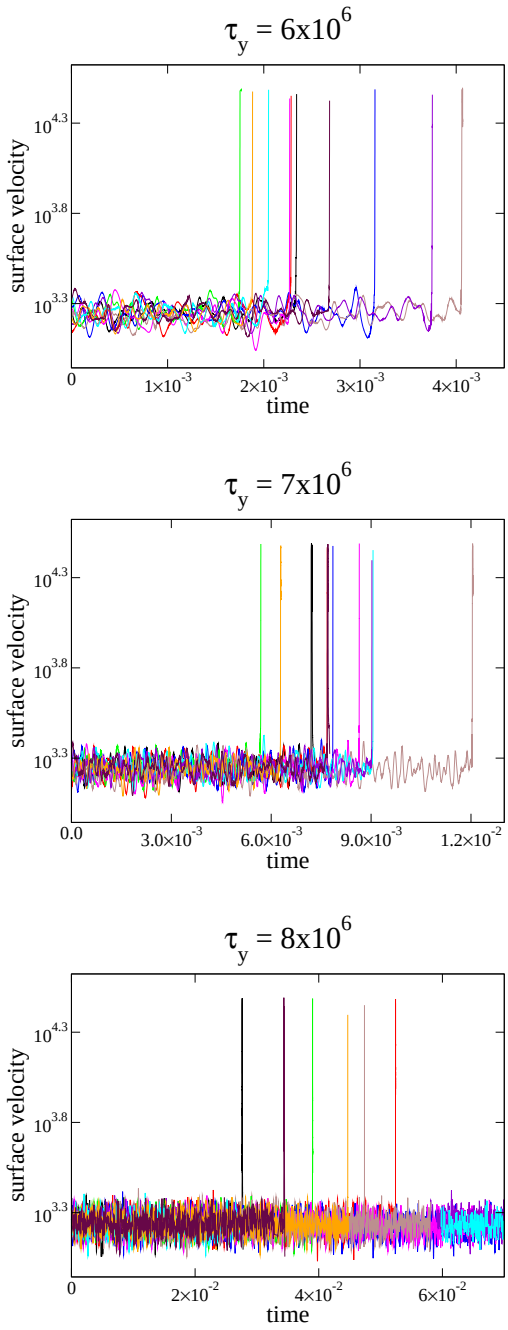

Figure 3.7 Time of failure with different values of yield stress for cases with different times of "turning on" the yield stress in a convective system operating in a statistically steady state. The different colors represent different "turning on" times. The ranges of failure times are about a factor of 2 for these cases at $\tau_y = 6 \times 10^6$ and 7×10^6, but for some of the cases at $\tau_y = 8 \times 10^6$, failure is not observed even when the simulation is run over non-dimensional time approaching one.

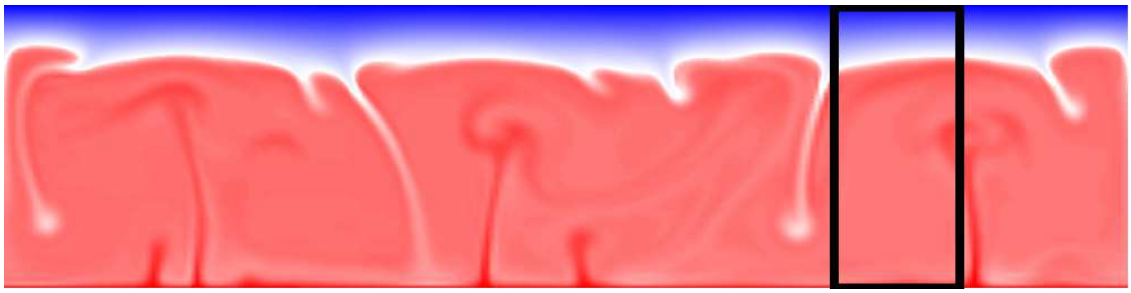

Figure 3.8 Sub-cell (in the black rectangular box) in a 4×1 convective box.

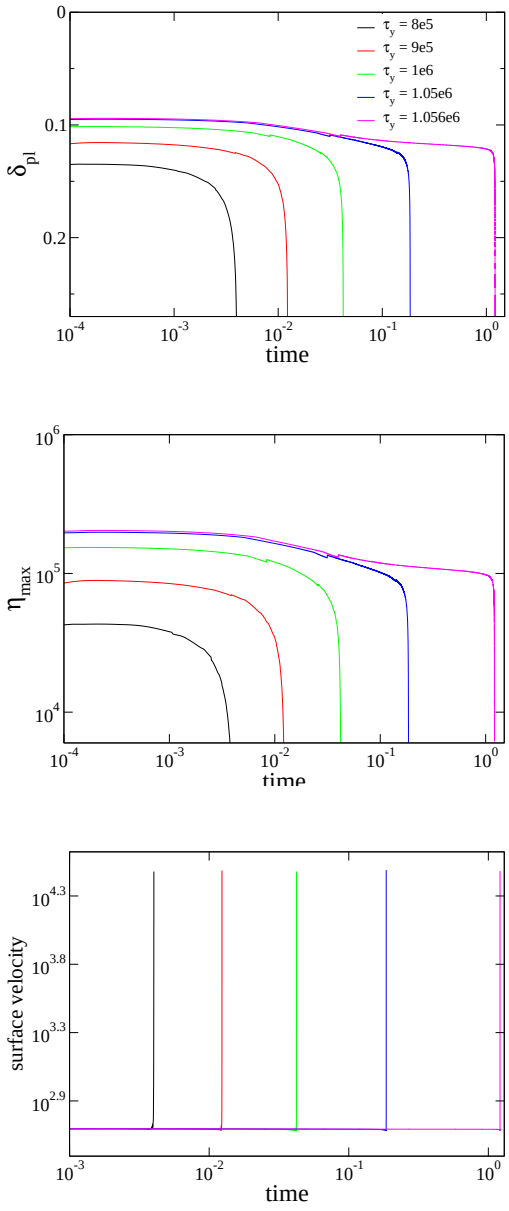

Figure 3.9 Depth of plastic zone, and maximum viscosity, and surface velocity over time. $\mathrm{Ra}_1 = 3\times10^7$, $a = 0.75$, $\Delta\eta = e^{16}$. All axes are dimensionless.

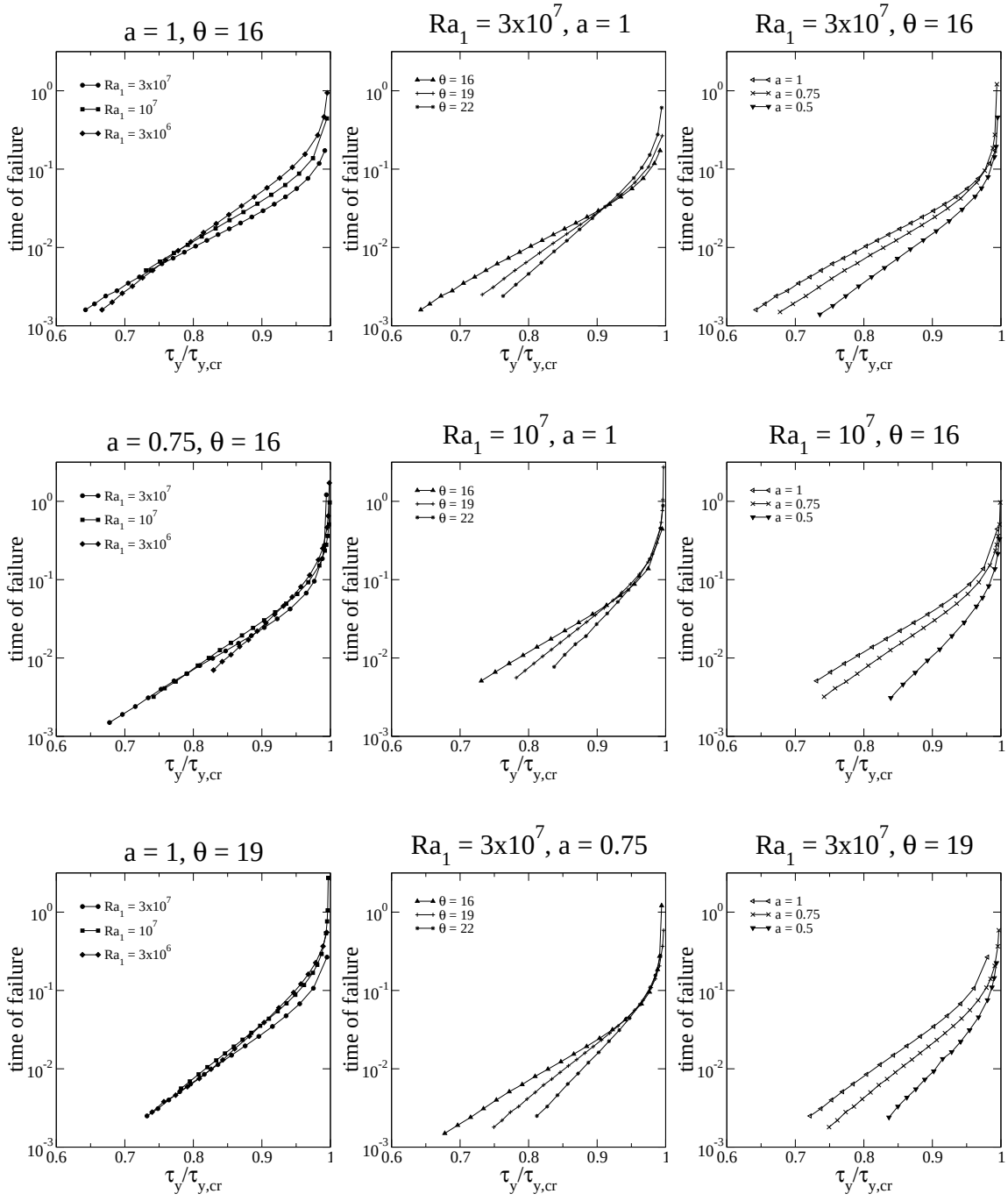

Figure 3.10 Time of failure as a function of the ratio of yield stress to critical yield stress in single-cell cases.

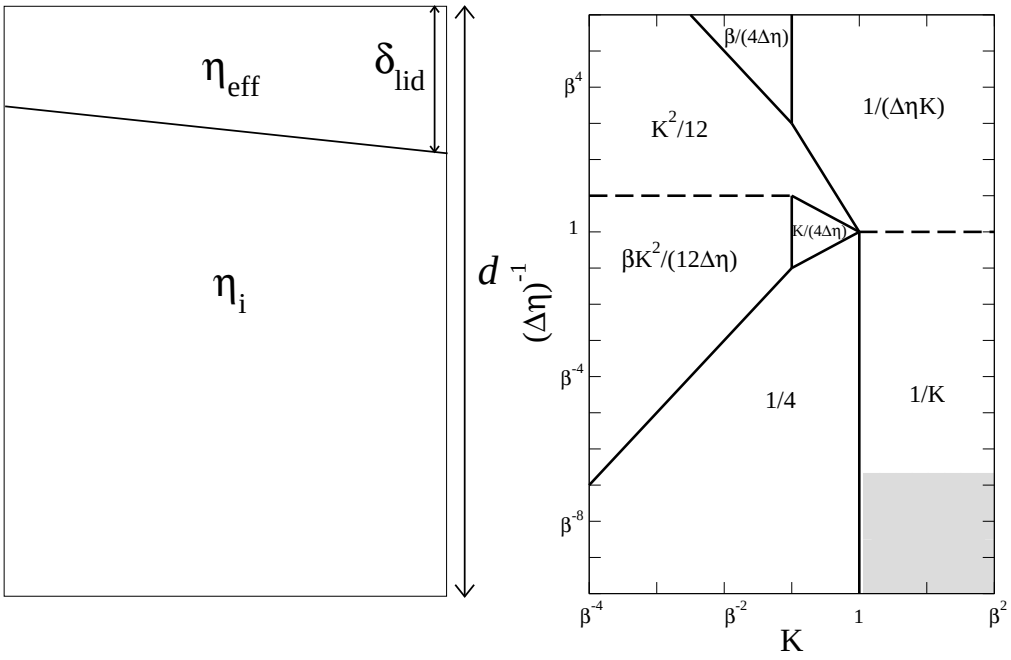

Figure 3.11 (a) Conceptual model of subduction as Rayleigh-Taylor instability. (b) Regime diagram for the growth rate $\tilde{s}$ for 2-D Rayleigh-Taylor instability, after (Canright and Morris 1993). The shaded area represents the regime applicable to our numerical experiments.

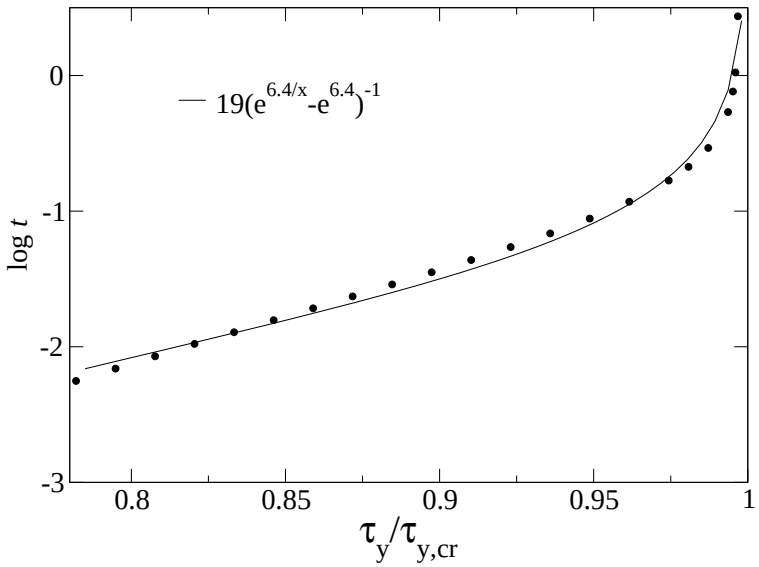

Figure 3.12 Log time as a function of the ratio $\tau_y/\tau_{y,cr}$ from numerical data (dots) and theoretical equation Eq. 3.17 (solid line). $\mathrm{Ra}_1 = 10^7$, $a = 1$, $\Delta\eta = \exp(19) \approx 2 \times 10^8$.

Chapter 4

Constraints on plate tectonics initiation from scaling laws for single-cell convection

T. Wong and V. S. Solomatov

An edited version of this chapter has been submitted for publication in *Phys. Earth and Planet. Inter.* of Elsevier.

Abstract

The Earth is the only planet known to have plate tectonics, while other planets are thought to be covered with a stagnant lid. On the Earth, the initiation of subduction, which is thought to be the fundamental process for plate tectonics initiation, is caused not only by the negative buoyancy of the lithosphere but also by the compressional forces from plate motions. However for planets which do not have plate tectonics, very first episode of lithospheric failure has to be caused by forces other than plate motions. Sublithospheric convection has been proposed as a possible mechanism that provides lithospheric instability through inducing stresses in the lithosphere, and lithospheric failure can occur when the yield stress is below a critical value. We test the applica-

bility of scaling laws for the critical yield stress obtained in single-cell convection simulations to strongly time-dependent multi-cell systems. We show that with an appropriate choice of characteristic aspect ratio for the convective system, the scaling laws from single-cell simulations can be used to evaluate the conditions on the terrestrial planets in the inner Solar System for plate tectonics to exist. The estimated values for critical yield stress and coefficient of friction are much lower than the observed values for the Earth's lithosphere. For Venus, Mars, and Mercury, a very small yield stress is required for plate tectonics to initiate.

4.1 Introduction

The diversity of terrestrial planets, both inside and outside the Solar System, have posed interesting questions their evolution, surface expression, and interior structures. One factor that contributes to the variety is the convective styles of the mantles in these planets. Plate tectonics is currently understood as a mode of convection that operates on the Earth, making it distinct from all other known planets where mantle convection, if existing, is likely to be in the stagnant lid regime. The presence of plate tectonics has implications on the planets' surface history and interior dynamics, which are closely related to the atmospheric composition and surface conditions, and ultimately linked to the origin of life (e.g., Franck et al. 2000). Therefore the origin of plate tectonics on the Earth, whether plate tectonics could have occurred on other planets, and the conditions favorable for Earth-like planets to have plate tectonics are active topics of research.

There has been many studies on how plate tectonics could have emerged on a planet. A potential mechanism to initiate subduction, which may be the key process to start plate tectonics on a one-plate planet, is sublithospheric convection (e.g., Ogawa 1990; Fowler and O'Brien 2003; Solo-

matov 2004b). A major difficulty for this mechanism is the high strength of the lithosphere that prevents it from failing. In numerical studies the strength is often reduced with a yield stress, which is a simplification of the weakening mechanisms in the lithosphere (e.g., Fowler 1993; Trompert and Hansen 1998; Moresi and Solomatov 1998; Tackley 2000a; Richards et al. 2001; Solomatov 2004b; Stein et al. 2004; O'Neill et al. 2007; Wong and Solomatov 2015). Obtaining scaling relations of the yield stress and physical parameters can help understanding the conditions favorable for plate tectonics.

This study aims to apply scaling laws developed for relatively simple and controlled convection systems to more variable time-dependent convection systems typical in planetary mantles. Our goal is to assess whether conditions on terrestrial planets in the inner Solar System allow plate tectonics to exist. These planets have more constraints from available observational data, and there have been different views on past and present episodes of plate tectonics which will be reviewed here.

4.2 Plate tectonics on terrestrial planets in the inner Solar System

4.2.1 Subduction initiation on the Earth

Plate tectonics on the Earth is thought to be driven by ridge push and slab pull forces. The origin of these forces comes from the movements of Earth's surface that are already occurring, but it is not clear how they first emerge. Calculations show that slab pull accounts for $\sim$90% of the driving forces (Lithgow-Bertelloni and Richards 1995), therefore to start plate tectonics, subduction initiation may be the key to mobilize the surface.

There are two main physical models for subduction initiation mechanisms on Earth: by gravita-

tional instability (termed by Stern (2004) as spontaneous nucleation of subduction zones) (Turcotte 1977; Stern and Bloomer 1992; Kemp and Stevenson 1996; Stern 2004), or by continued compression due to trench congestion or plate reorganization (induced nucleation of subduction zones) (McKenzie 1977; Mueller and Phillips 1991; Toth and Gurnis 1998; Hall et al. 2003; Gurnis et al. 2004).

Spontaneous nucleation of subduction zones refers to lithospheric failure due to vertical force of gravity such that the denser plate thrusts under the less dense plate at passive margins, along transform faults, or fracture zones. This type of models usually involves tensile failure, as the tensile strength is lower than the compressive strength (Turcotte 1977; Kemp and Stevenson 1996). Passive margin failure could be aided by sedimentary loading (Cloetingh et al. 1989) with the help of wet rheology (Regenauer-Lieb et al. 2001) and/or low-temperature plasticity (Branlund et al. 2001).

Induced nucleation involves horizontal compressional forces, which could be found in sites such as intraoceanic subduction zones, transform faults, passive margins, and spreading centers. A number of experimental, numerical, and analytical studies showed that without the help of compressional forces, it is difficult for ridge push alone to overcome the forces that resist lithospheric rupture (e.g., McKenzie 1977; Mueller and Phillips 1991; Shemenda 1992; Gurnis et al. 2004). In his estimates, McKenzie took the frictional shear resistance to be 1–10 MPa from seismic studies, while Mueller and Phillips used experimental results of rock deformation to obtain values on the order of 10^2–10^3 MPa. Toth and Gurnis (1998) presented numerical models suggesting that the frictional resistance of the fault has to be as low as a few MPa in order for subduction to initiate with ridge push forces, which is one or two orders of magnitude lower than the value predicted by experiments (Byerlee 1978).

Although the spontaneous nucleation and induced nucleation models differ in the source of forces that initiate subduction, both predict that subduction zones nucleate along preexisting weak zones or transform boundary. Therefore much effort has been devoted to understand the mechanisms of deformation localization to create weak zones (e.g., Bercovici et al. 2001; Branlund et al. 2001; Regenauer-Lieb and Kohl 2003).

4.2.2 Possible plate tectonics on Venus

Plate tectonics is not thought to be currently active on Venus. The random distribution of craters on Venus suggests that the planet has a young surface of less than 700 Ma (Arkani-Hamed et al. 1993; Herrick 1994; Turcotte et al. 1999). Although Venus has a plethora of tectonic features including coronae and chasmata, plate-boundary signatures resembling those on the Earth such as subduction zones and spreading centers are not obvious (e.g., Smrekar et al. 2010). Venus has a unimodal hypsometry while the Earth has very distinctly different elevations between the continents and the ocean basins, implying that plate tectonics processes on the Earth are not present on Venus (e.g., McGill et al. 2010).

The young age of the surface is believed to be due to a catastrophic resurface event that occurred $\sim$500–1000 Ma (e.g., McKinnon et al. 1997). The process of this resurfacing event is not clear, as the main source of observational data for this event comes from cratering records. Two major models for the nature of the resurfacing event were proposed: plate tectonics or plume/magmatic activity. Magmatic resurfacing is probably the most direct conclusion from observations of widespread volcanic landforms (e.g. Phillips and Hansen 1998; Stofan et al. 2005; Reese et al. 2007). For the tectonic resurfacing model, geologic features have been identified as localized subduction zones, which may have triggered the catastrophic resurfacing (Schubert and Sandwell 1995), although

these features might have other non-plate-boundary origins such as diapirs (Hansen and Phillips 1993).

If the resurfacing event has tectonic origins, the end of this event may represent the cessation of Venusian plate tectonics (Arkani-Hamed et al. 1993; Herrick 1994), or it may be a quiescent period in between episodes of subduction (Parmentier and Hess 1992; Turcotte 1993; Weinstein 1996; Fowler and O'Brien 1996; Schubert et al. 1997; Moresi and Solomatov 1998). The transition to a one-plate planet may be caused by mantle cooling (Herrick 1994) and thus a decline in the vigor of mantle convection (Arkani-Hamed et al. 1993; Solomatov and Moresi 1996). Mantle cooling can make the lithosphere positively buoyant (Herrick 1994), and the decline in convection also decreases the stresses in the lithosphere that might be able to mobilize the surface (Solomatov and Moresi 1996). However, without an efficient heat loss mechanism such as plate tectonics, the mantle temperature would increase and the planet may undergo episodic subduction to lose heat (Turcotte 1995).

One reason for the lack of plate tectonics on Venus may be its high surface temperature. The hot surface evaporates water away so the dry lithosphere has a higher yield strength, making subduction more difficult on Venus than on Earth (e.g., Kaula 1994; Mackwell et al. 1998). The high temperatures also favor grain growth, which hinders deformation localization and therefore failing to produce plate boundary and subduction zones (Landuyt and Bercovici 2009). The positive buoyancy of both the crust and the depleted mantle residuum inhibits subduction (Parmentier and Hess 1992), but the thickness of the crust is debated (Sandwell and Schubert 1992; Phillips 1994; Orth and Solomatov 2012).

4.2.3 Possible plate tectonics on early Mars

Mars poses a different set of problems for plate tectonics due to its intermediate size and cold surface. Plate tectonics has been suggested for different periods in Mars' history. Early plate tectonics on Mars was proposed as the origin of the global dichotomy. From the lateral extent of the thin crust of the northern lowlands, Sleep (1994) hypothesized that the northern lowlands were formed from seafloor spreading. However crater densities and structural features in the northern plains show that the area does not conform to this plate tectonics model of formation (Pruis and Tanaka 1995; Frey 2004).

Another line of evidence for early Martian plate tectonics comes from magnetic field data. The magnetic lineations observed by Mars Global Surveyor in the southern hemisphere (Acuna et al. 1999) have been interpreted as a signature for plate tectonics processes such as seafloor spreading (Connerney et al. 1999) and accretion of terranes (Fairen et al. 2002). Based on the magnitude of magnetic field in the magnetic lineations in the southern highlands, there might have been an active dynamo in early Mars (Acuna et al. 1999). This dynamo demands a large core heat flux, which may require early plate tectonics to drive core cooling (Nimmo and Stevenson 2000), and plate tectonics could efficiently cool the planet to avoid early massive melting (Hauck and Phillips 2002). However other non-plate tectonics mechanisms for magnetic lineations such as dike intrusion could be possible (Nimmo 2000). The Martian dynamo can also be driven by an initially hot core without plate tectonics (Breuer and Spohn 2003). Further evidence against early plate tectonics includes the isotopic heterogeneity of the early mantle from Martian meteorites, which indicates that the mantle had not undergone much recycling (Albarede et al. 2000; Halliday et al. 2001).

Plate tectonics occurring at a later period of Mars' history has also been proposed. Mapping of the Valles Marineris interpreted the feature as a large-scale strike-slip fault that could be a plate boundary, suggesting some form of plate tectonics in the Late Hesperian and Amazonian (Yin 2012). However, the small displacement ($\sim$160 km) on this fault and the lack of such features anywhere else on the planet makes this argument rather weak. Processes other than plate tectonics could be responsible for the formation of this feature.

4.2.4 Stress state of Mercury's surface

Although plate tectonics is ruled out as a cooling mechanism for Mercury, recent mapping analysis by Byrne et al. (2014) raised questions on the stress state of the surface as it might be more deformable than previously thought. The observations from Mariner 10 and the MESSENGER spacecraft revealed a heavily cratered surface with tectonic features on Mercury, which indicate that this could be a one-plate planet undergoing global contraction (e.g., King 2008; Watters et al. 2009; Byrne et al. 2014). Other causes for the distribution and orientation of lobate scarps and wrinkle ridges include tidal despinning and convection patterns (e.g., Melosh and McKinnon 1988; King 2008; Padovan et al. 2014; Klimczak et al. 2015; Watters et al. 2015).

There has been a longstanding debate on whether Mercury's mantle is currently convecting. Since Mariner 10 only had three flybys that had limited coverage of the planet, earlier simulations of mantle convection of Mercury tested a range of parameters for thermal evolution. Their findings indicate that existence of convection depends on several factors including the concentration of radiogenic elements in the mantle, the core heat flux, and mantle rheology (Hauck et al. 2004; Redmond and King 2007). MESSENGER provided surface measurements of radiogenic elements that constrain the heat production and thus the thermal history of Mercury (Peplowski et al. 2011),

and the geophysical observations constrained the thickness of the silicate layer to be in the range of 300–600 km (Smith et al. 2012; Hauck et al. 2013). Therefore if convection exists it is likely to be in the stagnant lid regime due to the small Rayleigh number (Solomatov 1995). Using different models of core cooling, Tosi et al. (2013) and Michel et al. (2013) reached opposing conclusions on whether convection is occurring. However due to uncertainties in interior structure, such as the existence and thickness of a solid FeS layer at the core-mantle boundary, these models do not exclude the possibility of mantle convection. Estimating the contribution of stresses induced by convection on Mercury's lithosphere has implications for the existence of convection and thus the thermal evolution on Mercury.

4.2.5 Possibility of plate tectonics on Earth-like exoplanets

Various theories have been proposed for the conditions of exoplanets to have plate tectonics based on different assumptions (e.g., O'Neill and Lenardic 2007; Valencia and O'Connell 2007, 2009; Korenaga 2010a; Karato 2011; van Heck and Tackley 2011; Foley et al. 2012; Stamenkovic and Breuer 2014). The different rheologies such as temperature-, pressure- and stress-dependent rheology, addition of water, internal heating, and the use of damage theory are considered in the scaling of mass and radius to conclude whether plate tectonics is likely to occur on exoplanets. The high pressure in the interior of larger-sized planets may be a major influence on their structure and evolution (e.g., Valencia et al. 2007; Wagner et al. 2011; Stamenkovic et al. 2012). It affects various properties including density, thermal expansivity and conductivity (van Heck and Tackley 2011; Tachinami et al. 2014), deformation mechanism and phase transitions (Karato 2011; Stein et al. 2011; Tackley et al. 2013), and enthalpy changes (Karato 2011; Stamenkovic et al. 2011). The compressibility of the mantle fluids would be relevant to high pressure conditions. Miyagoshi

et al. (2014, 2015) modeled convection of compressible fluids and concluded that adiabatic compression suppresses convection thus does not favor plate tectonics. The effects of pressure on the rheology require further experimental and theoretical support.

4.3 Critical yield stress approach and scaling laws

One way of studying the criterion of failure for different planets is to develop scaling relations between the yield stress of planetary lithospheres and various physical parameters. The yield stress is a physical property that is determined experimentally or from geophysical observations. Due to uncertainties in assumptions and complications in extrapolation, these observed values of yield stress are not well constrained and are usually too high for the lithosphere to fail. For these reasons we obtained scaling laws using the critical yield stress approach: the yield stress is a variable that is adjusted to the point at which the lithosphere becomes unstable, while the other parameters of the convective system are held constant (Solomatov 2004b; Wong and Solomatov 2015). This process is repeated for different sets of convective parameters.

To examine how the yield stress affects the stress distribution of the lithosphere, Wong and Solomatov (2015) carried out an analysis of the spatial variation in magnitude of stresses induced in the lithosphere by sublithospheric convection. They found that the process of subduction can be approximately described by the gravitational sliding model in which the stresses are caused by the variations of the lid base topography, in particular the dipping of the lid slope that provides the instability. To find out the extent of weakening needed for the lithosphere to become unstable, they determined the depth of region affected by the yield stress (termed the depth of the plastic zone δ_{pl}, Fig. 4.1). Contrary to previous belief that this depth is controlled by the viscosity of the mantle

(e.g., Fowler and O'Brien 2003; van Heck and Tackley 2011) or the viscosity contrast for the mobilization of the stagnant lid (Solomatov 2004b), the depth of the plastic zone is approximately 1/2–1/3 of the lithospheric thickness, even if the viscosity contrast at this depth is as high as $\sim 10^7$. Wong and Solomatov (2015) thus obtained the following expressions for the critical yield stress $\tau_{y,cr}$ and critical yield stress gradient $\tau'_{y,cr}$:

$$\tau_{y,cr} = -\alpha\rho_0 g\frac{dT}{dy}\lambda\frac{y_{\rm pl}^2}{2}\frac{a}{\delta_{\rm pl}}, \tag{4.1}$$

$$\tau'_{y,cr} = -\alpha\rho_0 g\frac{dT}{dy}\lambda\frac{y_{\rm pl}^2}{2}\frac{a}{\delta_{\rm pl}^2}, \tag{4.2}$$

where $y_{\rm pl}$ is the distance from the interior to $\delta_{\rm pl}$ respectively (Fig. 4.1), and other parameters are defined in Table 4.1. Eqs. 4.1 and 4.2 imply that these critical values depend on the topography of the bottom of the lithosphere: the aspect ratio and the lid slope, as well as other factors including the thermal gradient which also depends on the aspect ratio.

Following the dimensional form in Wong and Solomatov (2015), after combining the terms in Eq. 4.1 and 4.2, the scaling laws for critical yield stress $\tau_{y,cr}$ and friction coefficient μ_{cr} are:

$$\tau_{y,cr} \sim 1.95\alpha\rho g\Delta T d\left(\frac{E\Delta T}{RT_i^2}\right)^{-1.03}\left(\frac{\delta_0}{d}\right)^{-0.41}a^{1.78}, \tag{4.3}$$

$$\mu \sim 89\alpha\Delta T\left(\frac{E\Delta T}{RT_i^2}\right)^{-1.74}\left(\frac{\delta_0}{d}\right)^{-1.55}a^{1.87}. \tag{4.4}$$

The above scaling laws were derived from single-cell steady-state convective solutions, which have more controlled flows and therefore permit relatively simple scaling analysis. In the following sections we describe our approach to test this analysis of single-cell solutions for the strongly time-dependent convection. These systems are more complex and difficult to analyze, but they are more

realistic representations of mantle convection on terrestrial planets. By establishing the relevance of these scaling laws to time-dependent convection, they can be used for extrapolation to planetary conditions.

4.4 Numerical methods

We use the finite element code CITCOM (Moresi and Solomatov 1995) to solve the equations of thermal convection in 2D with a fixed temperature difference $\Delta T = T_1 - T_0$ between the top and the bottom with free-slip boundary conditions. The equations of thermal convection in Boussinesq approximation and infinite Prandtl number are

$$\nabla \cdot \mathbf{u} = 0, \tag{4.5}$$

$$\alpha \rho g T' \mathbf{n} - \nabla p' + \nabla \times \bar{\bar{\tau}} = 0, \tag{4.6}$$

$$\frac{\partial T'}{\partial t} + \mathbf{u} \cdot \nabla T' = \kappa \nabla^2 T', \tag{4.7}$$

where notations are defined in Table 4.1. The stress tensor $\bar{\bar{\tau}}$ has components τ_{ij}:

$$\tau_{ij} = \eta(\nabla \mathbf{u} + \{\nabla \mathbf{u}\}^T), \tag{4.8}$$

where η is the viscosity, $\{\}^T$ is the transpose operator.

The viscosity strongly depends on the temperature and it assumes an Arrhenius form:

$$\eta = A \exp\left(\frac{E}{RT}\right) \tag{4.9}$$

where A is a constant. The viscosity is often approximated by the exponential form:

$$\eta = B \exp(-\gamma T) \tag{4.10}$$

where B is another constant, and $\gamma = E/RT_i^2$, which in non-dimensional form is known as the Frank-Kamenetskii parameter:

$$\theta = \gamma \Delta T. \tag{4.11}$$

To simulate brittle failure of the lithosphere, we use a pseudoplastic rheology with a yield stress that takes the form of either a constant (τ_y) or a constant gradient with depth τ_y', although it is often a combination of both as defined by Byerlee's law (Byerlee 1978). This approach is commonly used in numerical studies that investigate mobile or episodic regimes of convection and plate-like behaviors (e.g., Moresi and Solomatov 1998; Trompert and Hansen 1998; Tackley 2000a; Fowler and O'Brien 2003). Plastic yielding occurs when convective stresses exceed the yield value and deformation follows a plastic flow law defined by an effective viscosity:

$$\eta_{\text{eff}} = \frac{\tau_y}{\dot{e}}, \tag{4.12}$$

where $\dot{e}$ is the second invariant of the strain rate tensor. When stresses are less than the yield stress, deformation occurs in the Newtonian creep as in Eq. 4.10.

The numerical calculations were performed with a 512×128 mesh as strongly time-dependent convection in the regime of high Rayleigh number and large aspect ratio ($a = 4$) requires higher resolution.

4.5 Comparison between theoretical and numerical critical yield stress and yield stress gradient: matching aspect ratios

To see how well the scaling theories developed from single-cell steady-state solutions apply to strongly time-dependent systems, we determine $\tau_{y,cr}$ and $\tau'_{y,cr}$ from numerical experiments of convective systems in the regime of higher Ra with longer aspect ratios. We then compare these numerically observed values of $\tau_{y,cr}$ and $\tau'_{y,cr}$ with theoretical predictions using the power law coefficients for the scaling laws in Table 4.3. To do so we need to find a characteristic aspect ratio to use in the scaling laws, as the long convective box is often subdivided into smaller aspect ratio cells with widths varying continually in time-dependent convection (Fig. 4.2). This variability in aspect ratio gives an uncertainty in determining the critical yield stress and yield stress gradient.

Previous studies obtained scaling laws for the aspect ratios by estimating the number of downwelling plumes in the convective system (Parmentier and Sotin 2000; Solomatov 2004b). However as described in the previous section, the lateral variation of the lid base is a key factor in initiation of lid failure, therefore a general value of the aspect ratio determined for the whole system from scaling laws may not be appropriate. If the scaling laws from single-cell simulations can be applied to multi-cell convective systems, the characteristic aspect ratio can be inferred from the critical yield stress or critical yield stress gradient using the scaling laws (with scaling exponents in Table 4.3) as:

$$a_\tau \sim 10^{-0.2}\tau_{y,cr}^{0.6}\mathrm{Ra}^{-0.7}\theta^{0.9}, \tag{4.13}$$

$$a_{\tau'} \sim 10^{-1.6}\tau_{y,cr}^{\prime 0.7}\mathrm{Ra}^{-0.9}\theta^{2.4}. \tag{4.14}$$

This aspect ratio is referred to as the inverted aspect ratio.

To see if this inverted aspect ratio has any correlation with the aspect ratios from the numerical solutions, we choose an aspect ratio that can be representative of the different sizes of the sub-cells in the multi-cell system. The size of the sub-cells are defined by the topography of the lid base. For the problem of subduction initiation, we look at the part of the convective box that is most prone to lid failure (Fig. 4.2). The scaling laws in Eq. 4.3 and 4.4 suggest that sub-cells with large aspect ratios have higher critical yield stresses and coefficients of friction, so we find the maximum possible aspect ratio of sub-cell in the convective system. However the maximum aspect ratio may not be a good predictor of the critical yield stress as the other factors such as lid slope also vary, therefore in addition to finding the maximum aspect ratio, we also determine the average aspect ratio of sub-cells.

For each set of convective parameters (same Ra and viscosity contrast), we check the maximum and average sub-cell width in a large yield stress (Fig. 4.3 left) or yield stress gradient (Fig. 4.3 right) case in which convection is in the stagnant lid regime. The shape of lid base, which determines the widths of sub-cells, can be inferred from the variation in surface heat flux horizontally. As shown in Wong and Solomatov (view), the variation in cell width is more or less stable when lithospheric failure does not occur, and this width is similar to the cell width before failure in cases with lower yield stress or yield stress gradient. The maximum and average aspect ratios from numerical simulations are listed in Table 4.2.

These numerically observed maximum and average aspect ratios (hereafter referred to as numerical aspect ratios) are compared with the inverted aspect ratios. From Fig. 4.3 and Table 4.2 the inverted aspect ratios mostly fall between the maximum aspect ratios and the average aspect ratios found from numerical solutions, except for a few cases with high Ra. The average aspect

ratio seems to show a better correlation with the inverted aspect ratio, so it may be a more suitable predictor of $\tau_{y,cr}$ and $\tau'_{y,cr}$ for a multi-cell time-dependent convection system. By multiplying the numerical average aspect ratio with a correction factor of $\sim$1.4, the numerically observed critical yield stress will be consistent with theoretical predictions, so the scaling laws from single-cell solutions can be used to estimate the critical yield stress and yield stress gradients in strongly time-dependent convection.

4.6 Application to terrestrial planets

4.6.1 Physical parameters for terrestrial planets

Tables 4.1 and 4.4 suggest the values of physical parameters that are applicable for conditions of Earth, Venus, Mars, and Mercury. The interior temperature T_i is taken to be $\sim$1700 K. At temperatures slightly below this value convection ceases, while at temperatures slightly above this value the mantle rocks begin to melt (Solomatov 2004b; Korenaga 2010b). Since the scaling laws used in this paper are derived from calculations using Newtonian rheology, we use the activation energy of diffusion for olivine which is about 375 kJ/mol (Hirth and Kohlstedt 2003). The melting temperature and the activation energy for wet olivine gives the interior viscosity that is close to the mantle viscosity, thus we take the mantle viscosity as the reference viscosity. Here we consider a typical value of interior viscosity 10^{19} (e.g., Schubert et al. 2001) in our extrapolation. Note that while the interior viscosity is uncertain, the critical yield stress is not very sensitive to this value but is most sensitive to the thermal structure of the lid. The lithospheric thickness is needed to estimate the friction coefficient, and it is inferred from heat flux estimates. For the Earth where plate tectonics processes contribute to the large average surface heat flow, we take the value typical

for oceanic lithosphere, which is about 40 mW/m^2 (e.g., Solomatov and Moresi 2000).

4.6.2 Depth of convecting layer

The depth of convecting layer is required for the dimensional scaling of $\tau_{y,cr}$ and μ_{cr}. Due to the exponential dependence of viscosity on pressure, the bottom part of the mantle is very viscous and thus sluggish. Therefore convection does not span the entire depth of the mantle and is restricted to the top part of the mantle (e.g., Christensen 1985), and at high viscosity contrasts the convective system breaks into smaller sub-cells (Khaleque et al. 2015). On the Earth, it is believed that small-scale convection is active in the upper mantle (e.g., Richter and McKenzie 1981; Solomatov and Moresi 2000; van Hunen et al. 2003). As the effects of pressure on convection is not well understood, for our scaling purposes we assume that the pressure reduces the depth to an effective depth of the actively convective layer. We use a range for this effective depth which goes from half to the whole of the depth of the convecting mantle. For Earth and Venus this is about 350–700 km. For smaller planets such as Mars and Mercury which have lower pressures, we take the entire mantle depth as the upper limit.

4.6.3 Aspect ratio

Since the aspect ratio of strongly time-dependent convection is variable as discussed in the previous section, we estimate the range of critical yield stress and coefficient of friction with limiting values of aspect ratios. The aspect ratios observed from numerical simulations range from about 0.2–0.5 (Table 4.2). The fit between the inverted aspect ratio and the numerical aspect ratio in Fig. 4.3 suggests that the average aspect ratio can be used in the scaling laws when multiplied with a coefficient of $\sim$1–2. Therefore we take the aspect ratio to be between 0.2–1.

4.6.4 Critical yield stress and critical coefficient of friction

The critical yield stress and critical yield stress gradient for various planets can be estimated from Eq. 4.3 and 4.4 using the parameters in Table 4.1 and 4.4, and they are listed in Table 4.5. We estimate $\tau_{y,cr}$ and μ_{cr} with higher and lower end values of aspect ratios, and the range in the magnitudes of $\tau_{y,cr}$ and μ_{cr} come from the depth range of the convective layer.

In the comparison between the Arrhenius viscosity and Frank-Kamenetskii approximation, Wong and Solomatov (2015) found that the scaling laws derived from calculations using exponential viscosity (Eq. 4.10) predict a slightly larger $\tau_{y,cr}$ than that of Arrhenius viscosity (Eq. 4.9) by $\sim$20–50%. This difference with exponential viscosity is greater for $\tau'_{y,cr}$, which could be $\sim$40% higher to almost 5 times larger than that with the Arrhenius viscosity. They found that as the difference between Arrhenius viscosity and its corresponding exponential viscosity increases, the ratio of the two yield values ($\tau_{y,cr,\mathrm{Arr}}/\tau_{y,cr,\mathrm{exp}}$ and $\tau'_{y,cr,\mathrm{Arr}}/\tau'_{y,cr,\mathrm{exp}}$) decreases to some asymptotic values that depend mostly on θ (Fig. 4.4). For the Earth and Mars which has $\theta \approx 22$ and where the surface temperature is low, the difference between Arrhenius and exponential viscosity is great ($\Delta\eta_{\mathrm{Arr}}/e^{\theta} \gg 10^{30}$). Referring to Fig. 4.4, the actual $\tau_{y,cr}$ and $\tau'_{y,cr}$ for these planets are in the asymptotic regime which are between 0.7–0.8 and 0.6–0.7 of their corresponding values from exponential viscosity. Venus's high surface temperature yields a smaller θ of about 15 and its viscosity difference between the two laws $\Delta\eta_{\mathrm{Arr}}/e^{\theta} \approx 10^{9}$, which gives $\tau_{y,cr,\mathrm{Arr}} \approx 0.6\tau_{y,cr,\mathrm{exp}}$ and $\tau'_{y,cr,\mathrm{Arr}} \approx 0.4\tau'_{y,cr,\mathrm{exp}}$. Mercury has $\theta \approx 20$ and viscosity difference $\approx 10^{24}$, giving $\tau_{y,cr,\mathrm{Arr}} \approx 0.7\tau_{y,cr,\mathrm{exp}}$ and $\tau'_{y,cr,\mathrm{Arr}} \approx 0.5\tau'_{y,cr,\mathrm{exp}}$.

We can make some remarks on the critical yield stress and friction coefficient for super-Earths based on the dimensional scaling laws. As the mass and size increase, the pressure inside the planet

also increases. Besides increasing gravitational acceleration, the pressure also affects the depth of the convecting layer. The pressure may reach a critical value at shallower depths that the viscosity becomes too high for the lower part of the mantle to participate in active convection. Therefore even if gravitational acceleration increases with pressure, the depth of convecting layer may be smaller; according to Eq. 4.3, these two properties may have compensating effects.

4.6.5 Uncertainties in extrapolation

One source of uncertainty is in the values of physical properties. The uncertainty in mantle viscosity gives Ra values with 3 orders of magnitude, causing the biggest range in extrapolation from our scaling laws. For the estimates of critical yield stress in this study we use the activation energy for diffusion creep, as the scaling laws were derived with Newtonian rheology. In previous estimates the value for dislocation creep was used, which yield a lower value of critical yield stress than the ones obtained in this study (e.g., Solomatov 2004b; Wong and Solomatov 2015).

The uncertainties in the scaling exponents in Table 4.3 due to numerical errors can result in about an order of magnitude difference from the theoretically predicted values.

As mentioned before and also in Wong and Solomatov (2015), the behavior of the nonlinear system near the critical value may be difficult to predict, and it may depend on the model runtime to observe lid failure. This also contributes to the uncertainty in determining the critical yield stress and yield stress gradient.

4.7 Discussion and conclusion

We have showed that the scaling laws derived from single-cell steady-state convection simulations can be applied to multi-cell time-dependent convection. The characteristic aspect ratio for a multi-cell time-dependent system can be obtained by determining the average aspect ratio of sub-cells in a convective box with large aspect ratio and modifying this value with a factor of $\sim$1–2. This aspect ratio can be used in the scaling laws to predict the critical yield stress and friction coefficient in strongly time-dependent convection.

In general, a very low yield stress and/or a small coefficient of friction is required for a stagnant lid planet to initiate plate tectonics. This agrees with previous theoretical estimates (e.g., Toth and Gurnis 1998), but much smaller than experimental values (e.g., Mueller and Phillips 1991). Water may be a key factor contributing to the low yield stress of the Earth's lithosphere (e.g., Kohlstedt et al. 1995), differentiating the Earth's evolution from that of Venus. As it is difficult for one-plate planets to have plate tectonics, other possibilities such as impact (Hansen 2007; Ruiz 2011) or transition from magma ocean convection (Solomatov 2004b; Foley et al. 2014; Solomatov 2015) may be viable candidates for the origin plate tectonics.

The properties affecting the critical yield stress and friction coefficient change with time. One of them is internal heating, which decays with time and changes the interior temperature. The critical yield stress can also be related with the change in rheology with time through more complicated models such the damage theory (e.g., Bercovici and Ricard 2012). In the future it might be helpful to investigate the connection between the parameters in the damage theory and the critical yield stress, such that at some point during the planet's history subduction initiation could be easier.

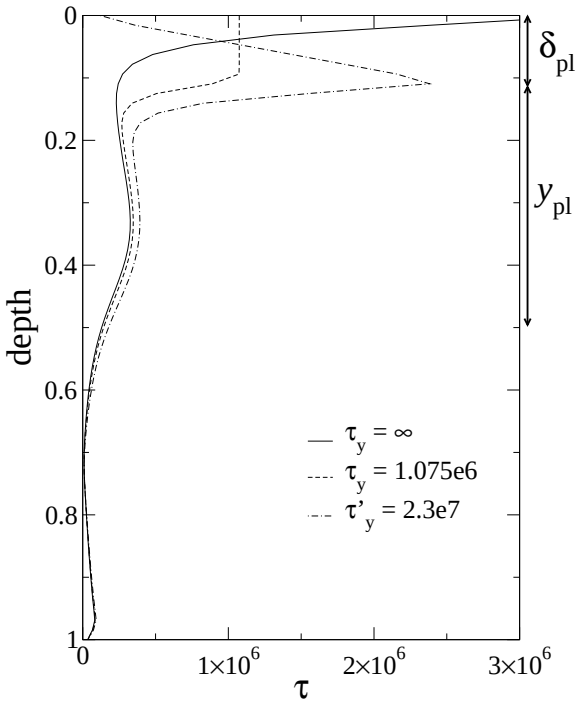

Figure 4.1 Depth of plastic zone $\delta_{\rm pl}$ and the vertical distance from the interior to this depth $y_{\rm pl}$. Profile taken at the the downwelling edge of the convecting cell.

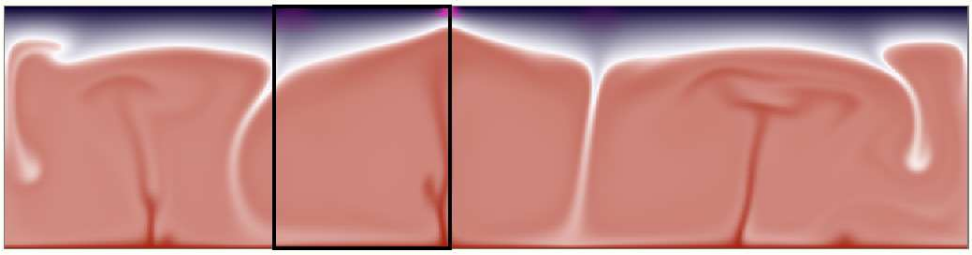

Figure 4.2 Incipient subduction in the sub-cell that is most prone to subduction in a long convective box. The cold blue lid starts to subduct into the hot interior in red color. The magenta color in the lid represent parts that have reached the yield stress.

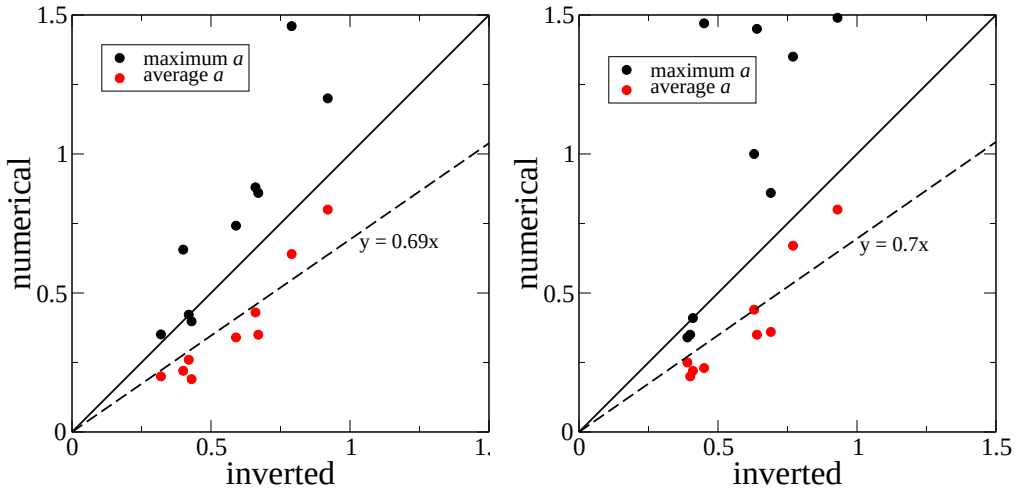

Figure 4.3 Comparison between the numerical aspect ratios and inverted aspect ratios. Left figure correspond to constant yield stress cases (τ_y) and right figure shows constant yield stress gradient cases (τ_y').

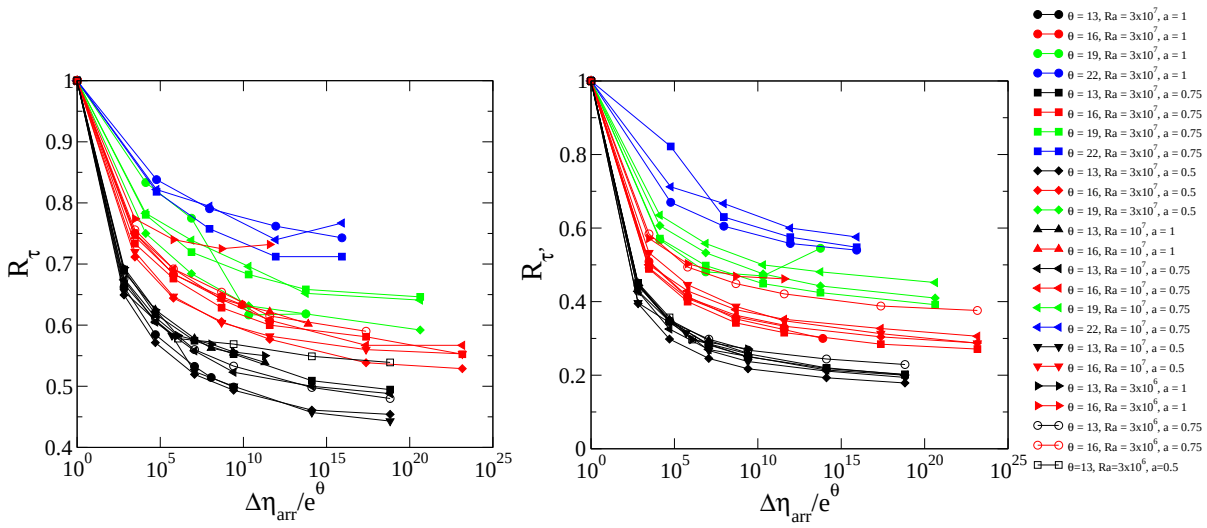

Figure 4.4 Ratio of yield stress for Arrhenius viscosity to that for exponential viscosity $R_\tau = \tau_{y,cr,\mathrm{Arr}}/\tau_{y,cr,\exp}$ and $R_{\tau'} = \tau'_{y,cr,\mathrm{Arr}}/\tau'_{y,cr,\exp}$ as a function of Arrhenius viscosity contrast normalized to exponential viscosity contrast $\Delta\eta_{\mathrm{Arr}}/\exp(\theta)$. The ratio $\Delta\eta_{\mathrm{Arr}}/\exp(\theta)$ depends on the surface temperature T_0, and it can go up to many orders of magnitude if T_0 is low. Asymptotically towards high $\Delta\eta_{\mathrm{Arr}}/\exp(\theta)$, R_τ and R'_τ are approximately proportional to θ. Figures adapted from Wong and Solomatov (2015).

Table 4.1 Model Parameters

Parameter	Notation	Value
Thermal expansion coefficient	α	3×10^{-5}
Reference density	ρ_0	
Temperature	T	
Lid slope	λ	
Aspect ratio	a	
Depth of convecting layer	d	
Thickness of lithosphere	δ_0	
Thermal diffusivity	κ	10^{-6} m^2 s^{-1}
Reference viscosity	η_0	10^{19} Pa s
Thermal conductivity	k	3 W m^{-1} K^{-1}
Activation energy (diffusion creep)	E	375 kJ mol^{-1}
Gas constant	R	
Interior temperature	T_i	1700 K
Velocity vector	$\mathbf{u}$	
Unit vector	$\mathbf{n}$	
Pressure perturbations	p'	
Temperature perturbations	T'	

Table 4.2 Comparison between critical yield stress predicted from theory and that obtained from numerical experiments for time dependent cases with $a = 4$. The characteristic aspect ratio of sub-cells in numerical experiments are calculated inversely from the observed $\tau_{y,cr}$ and $\tau'_{y,cr}$.

		constant τ_y				constant τ'_y				
Ra_1	$\Delta\eta$	max. a	$\tau_{y,cr}$	avg. a	$\tau_{y,cr}$	max. a	$\tau'_{y,cr}$	avg. a	$\tau'_{y,cr}$	method
10^8	10^6	1.46	1.39×10^7	0.64	3.53×10^6	1.35	4.09×10^8	0.67	1.47×10^8	theoretical
				0.79	5×10^6			0.77	1.8×10^8	numerical
10^8	10^7	0.88	4.76×10^6	0.43	1.46×10^6	1.0	1.57×10^8	0.44	4.83×10^7	theoretical
				0.66	3×10^6			0.63	8×10^7	numerical
10^8	10^8	1.2	6.71×10^6	0.8	3.39×10^6	1.49	1.79×10^8	0.8	7.22×10^7	theoretical
				0.92	4.25×10^6			0.93	9×10^7	numerical
3×10^8	10^6	0.742	1.49×10^7	0.34	3.94×10^6	1.45	1.98×10^9	0.35	2.45×10^8	theoretical
				0.59	10^7			0.64	6×10^8	numerical
3×10^8	10^7	0.86	1.53×10^7	0.35	3.41×10^6	0.86	5.5×10^8	0.36	1.58×10^8	theoretical
				0.67	10^7			0.69	4.5×10^8	numerical
3×10^8	10^8	0.422	3.85×10^6	0.26	1.67×10^6	0.34	9.23×10^7	0.25	5.81×10^7	theoretical
				0.42	3.8×10^6			0.39	1.1×10^8	numerical
10^9	10^6	0.398	1.95×10^7	0.19	5.51×10^6	1.47	1.01×10^{10}	0.23	6.74×10^8	theoretical
				0.43	2.2×10^7			0.45	1.8×10^9	numerical
10^9	10^7	0.351	1.27×10^7	0.2	4.95×10^6	0.35	7.54×10^8	0.2	3.32×10^8	theoretical
				0.32	1.1×10^7			0.4	9×10^8	numerical
10^9	10^8	0.656	2.99×10^7	0.22	4.89×10^6	0.41	6.08×10^8	0.22	2.46×10^8	theoretical
				0.4	1.3×10^7			0.41	6×10^8	numerical

Table 4.3 Power law coefficients in scalings of different parameters with Ra, aspect ration a, and Frank-Kamenetskii parameter θ from Wong and Solomatov (2015)

Parameter	c in 10^c	Ra	a	θ
δ_0	-0.26 $\pm$ -0.10	-0.22 $\pm$ 0.01	0.27 $\pm$ 0.04	1.12 $\pm$ 0.06
$\tau_{y,cr}$	0.40 $\pm$ 0.22	1.09 $\pm$ 0.03	1.67 $\pm$ 0.09	-1.49 $\pm$ 0.14
$\tau'_{y,cr}$	2.34 $\pm$ 0.32	1.34 $\pm$ 0.04	1.45 $\pm$ 0.14	-3.47 $\pm$ 0.21

Table 4.4 Parameters for terrestrial planets

	Earth	Venus	Mars	Mercury
Depth of convective layer (d) km	350 – 700	350 – 700	850 – 1700	350 – 660
Gravitational acceleration (g) m/s^2	9.8	8.9	3.7	3.8
Density (ρ) kg/^{3}	3300	3300	3500	3500
Surface temperature (T_0) K	300	733	270	442
Surface heat flux (q) mW/m^2	40	20	30	30

Table 4.5 Estimates of critical yield stress $\tau_{y,cr}$ and friction coefficient μ_{cr} for terrestrial planets.

	$\tau_{y,cr}$ (MPa)	
	$a = 0.2$	$a = 1$
Earth	3.7 – 9.8	65 – 170
Venus	2.9 – 7.7	51 – 140
Mars	2.9 – 7.8	52 – 140
Mercury	0.9 – 2.2	16 – 39
	μ_{cr}	
Earth	0.005 – 0.016	0.11 – 0.32
Venus	0.006 – 0.016	0.11 – 0.33
Mars	0.002 – 0.006	0.043 – 0.13
Mercury	0.001 – 0.004	0.027 – 0.072

Chapter 5

Conclusions and future directions

Initiation of plate tectonics on a planet operating in the stagnant lid convection regime is difficult. Although sublithospheric convection is capable of inducing large stresses in the lithosphere, especially towards the surface, to mobilize the lithosphere plastic yielding has to penetrate through some depths into the lid. To do so a very low yield stress is required since the stresses at depth are small. We quantify the extent of this depth by examining the stress distribution in the stagnant lid. Our scaling laws indicate that the physical conditions on the terrestrial planets in the inner Solar System gives a small value of critical yield stress, which means that the existence of plate tectonics is not favored as the yield stress of the lithosphere is often too high for these planets. This further confirms previous theories (e.g., Solomatov 2004b) that the natural state of a planet is to be covered with a stagnant lid.

Plate tectonics initiation may also depend on chance. Our simulations have shown that even if the physical parameters are in the range that allow surface mobilization, the timing is a variable outcome depending on the initial conditions and evolution of the system. As the evolution of the convection system is sensitive to the initial conditions, the timing of subduction initiation is a random property of chaotic convective systems. Although the scaling laws provide insights

into favorable physical conditions for the initiation of plate tectonics from stagnant lid convection, the occurrence of plate tectonics may be unpredictable as the range of subduction initiation time resulting from the chaotic nature of strongly time-dependent convection can exceed planetary lifetimes.

The problem of plate tectonics initiation is far from being solved. Here we are only considering one possible scenario: initiation from a sub-solidius stagnant lid planet. We mentioned in the previous chapter the possible exogenic origins such as impacts, or transition from magma ocean convection. We still do not understand one of the most basic questions: why does the Earth have plate tectonics? There are also other obstacles to plate tectonics as well, such as the compositional buoyancy that hinders plate motions (e.g., Sleep and Windley 1982). In the problem of lithospheric strength addressed here, there are still complexities in the rheology, such as dependencies on stress, grain size, and pressure, that need to be taken into account. This work presents a theoretical approach to analyze the mechanics of the lithosphere in convection systems. This can be applied to investigate more realistic rheologies, which will be relevant to both terrestrial lithospheres and planetary bodies with different materials. For example, the theoretical analysis can provide an assessment for the recent hypothesis of subduction on Europa (Kattenhorn and Prockter 2014), the potential of subduction zones developing on Venus in features such as coronae and rifts (e.g., Schubert and Sandwell 1995), and studying pressure effects will be pertinent to understanding the evolution and the possibility of plate tectonics on super-Earths.

Bibliography

Acuna, M., Connerney, J., Ness, N., Lin, R., Mitchell, D., Carlson, C., McFadden, J., Anderson, K., Reme, H., Mazelle, C., Vignes, D., Wasilewski, P., and Cloutier, P. (1999). Global distribution of crustal magnetization discovered by the mars global surveyor mag/er experiment. *Science*, 284(5415):790–793.

Albarede, F., Blichert-Toft, J., Vervoort, J., Gleason, J., and Rosing, M. (2000). Hf-nd isotope evidence for a transient dynamic regime in the early terrestrial mantle. *Nature*, 404(6777):488–490.

Arkani-Hamed, J., Schaber, G., and Strom, R. (1993). Constraints on the thermal evolution of venus inferred from magellan data. *J. Geophys. Res.*, 98(E3):5309–5315.

Bercovici, D. and Ricard, Y. (2005). Tectonic plate generation and two-phase damage: Void growth versus grain size reduction. *J. Geophys. Res.*, 110(B3).

Bercovici, D. and Ricard, Y. (2012). Mechanisms for the generation of plate tectonics by two-phase grain-damage and pinning. *Phys. Earth. Planet. Int.*, 202-203:27–55.

Bercovici, D., Ricard, Y., and Richards, M. A. (2000). *The Relation Between Mantle Dynamics and Plate Tectonics: A Primer*, pages 5–46. American Geophysical Union, Washington, D. C.

Bercovici, D., Ricard, Y., and Schubert, G. (2001). A two-phase model for compaction and damage: 3. applications to shear localization and plate boundary formation. *Journal of Geophysical Research: Solid Earth*, 106(B5):8925–8939.

Branlund, J., Regenauer-Lieb, K., and Yuen, D. (2001). Weak zone formation for initiating subduction from thermo-mechanical feedback of low-temperature plasticity. *Earth Planet. Sci. Lett.*, 190(3-4):237–250.

Breuer, D. and Spohn, T. (2003). Early plate tectonics versus single-plate tectonics on mars: Evidence from magnetic field history and crust evolution. *J. Geophys. Res.*, 108(E7).

Burov, E. and Cloetingh, S. (2010). Plume-like upper mantle instabilities drive subduction initiation. *Geophysical Research Letters*, 37(3):n/a–n/a. L03309.

Byerlee, J. (1978). Friction of rocks. *Pure Appl. Geophys.*, 116(4-5):615–626.

Byrne, P. K., Klimczak, C., Sengor, A. M. C., Solomon, S. C., Watters, T. R., and Steven A. Hauck, I. (2014). Mercurys global ontraction much greater than earlier estimates. *Nature Geoscience*, 7:301–307.

Canright, D. and Morris, S. (1993). Buoyant instability of a viscous film over a passive fluid. *J. Fluid Mech.*, 255:349–372.

Christensen, U. R. (1985). Heat transfer by variable viscosity convection, ii, presure influence, non-newtonian rheology, and decaying heat sources. *Phys. Earth Planet Inter.*, 35:141–166.

Cloetingh, S., Wortel, R., and Vlaar, N. (1989). On the initiation of subduction zones. *Pure Appl. Geophys.*, 129(1-2):7–25.

Connerney, J., Acuna, M., Wasilewski, P., Ness, N., Reme, H., Mazelle, C., Vignes, D., Lin, R., Mitchell, D., and Cloutier, P. (1999). Magnetic lineations in the ancient crust of mars. *Science*, 284(5415):794–798.

Crameri, F. and Tackley, P. J. (2015). Parameters controlling dynamically self-consistent plate tectonics and single-sided subduction in global models of mantle convection. *Journal of Geophysical Research: Solid Earth*, 120(5):3680–3706. 2014JB011664.

Crameri, F., Tackley, P. J., Meilick, I., Gerya, T. V., and Kaus, B. J. P. (2012). A free plate surface and weak oceanic crust produce single-sided subduction on earth. *Geophys. Res. Lett.*, 39(3):n/a–n/a. L03306.

Davies, G. (1988). Role of the lithosphere in mantle convection. *Journal of Geophysical Research-Solid Earth and Planets*, 93(B9):10451–10466.

Davies, G. (1989). Mantle convection model with a dynamic plate - topography, heat-flow and gravity-anomalies. *Geophysical Journal International*, 98(3):461–464.

Dymkova, D. and Gerya, T. (2013). Porous fluid flow enables oceanic subduction initiation on earth. *Geophysical Research Letters*, 40(21):5671–5676.

Fairen, A., Ruiz, J., and Anguita, F. (2002). An origin for the linear magnetic anomalies on mars through accretion of terranes: Implications for dynamo timing. *Icarus*, 160(1):220–223.

Foley, B. J., Bercovici, D., and Elkins-Tanton, L. T. (2014). Initiation of plate tectonics from post-magma ocean thermochmical convection. *J. Geophys. Res.*, 119:8538–8561.

Foley, B. J., Bercovici, D., and Landuyt, W. (2012). The conditions for plate tectonics on super-earths: Inferences from convection models with damage. *Earth Planet. Sci. Lett.*, 331:281–290.

Fowler, A. (1985). Fast thermoviscous convection. *Studies in Applied Mathematics*, 72(3):189–219.

Fowler, A. (1993). Boundary-layer theory and subduction. *J. Geophys. Res.*, 98(B12):21997–22005.

Fowler, A. and O'Brien, S. (1996). A mechanism for episodic subduction on venus. *J. Geophys. Res.*, 101(E2):4755–4763.

Fowler, A. and O'Brien, S. (2003). Lithospheric failure on venus. *Proceedings of the Royal Society of London Series A-Mathematical Physical and Engineering Sciences*, 459(2039):2663–2704.

Franck, S., Block, A., von Bloh, W., Bounama, C., Schellnhuber, H., and Svirezhev, Y. (2000). Reduction of biosphere life span as a consequence of geodynamics. *Tellus Series B-Chemical and Physical Meteorology*, 52(1):94–107.

Frank-Kamenetskii, D. (1969). *Diffusion and heat exchange in chemical kinetics*. Plenum Press.

Frey, H. V. (2004). A timescale for major events in early mars crustal evolution. In *35th Lunar and Planetary Science Conference*, page Abstract #1382, Houston. Lunar and Planetary Institute.

Goetze, C. and Evans, B. (1979). Stress and temperature in the bending lithosphere as constrained by experimental rock mechanics. *Geophys. J. R. astr. Soc*.

Gurnis, M. (1988). Large-scale mantle convection and the aggregation and dispersal of supercontinents. *Nature*, 332(6166):695–699.

Gurnis, M., Hall, C., and Lavier, L. (2004). Evolving force balance during incipient subduction. *Geochemistry, Geophysics, Geosystems*, 5(7):n/a–n/a. Q07001.

Gurnis, M., Zhong, S., and Toth, J. (2000). On the competing roles of fault reactivation and brittle failure in generating plate tectonics from mantle convection. *Geophysical Monograph*, 121:73–94.

Hall, C., Gurnis, M., Sdrolias, M., Lavier, L., and Muller, R. (2003). Catastrophic initiation of subduction following forced convergence across fracture zones. *Earth Planet. Sci. Lett.*, 212(1-2):15–30.

Halliday, A., Wanke, H., Birck, J., and Clayton, R. (2001). The accretion, composition and early differentiation of mars. *Space Science Reviews*, 96(1-4):197–230. ISSI Workshop on Chronology and Evolution of Mars, Bern, Switzerland, APR 10-14, 2000.

Hansen, V. and Phillips, R. (1993). Tectonics and volcanism of eastern aphrodite terra, venus - no subduction, no spreading. *Science*, 260(5107):526–530.

Hansen, V. L. (2007). Subduction origin on early earth: A hypothesis. *Geology*, 35(12):1059–1062.

Hauck, S. and Phillips, R. (2002). Thermal and crustal evolution of mars. *J. Geophys. Res.*, 107(E7).

Hauck, S. A., Dombard, A. J., Phillips, R. J., and Solomon, S. C. (2004). Internal and tectonic evolution of mercury. *Earth and Planetary Science Letters*, 222:713 – 728.

Hauck, II, S. A., Margot, J.-L., Solomon, S. C., Phillips, R. J., Johnson, C. L., Lemoine, F. G., Mazarico, E., McCoy, T. J., Padovan, S., Peale, S. J., Perry, M. E., Smith, D. E., and Zuber, M. T. (2013). The curious case of mercury's internal structure. *J. Geophys. Res.-Planets*, 118(6):1204–1220.

Herrick, R. (1994). Resurfacing history of venus. *Geology*, 22(8):703–706.

Hirth, G. and Kohlstedt, D. (2003). Rheology of the upper mantle and mantle wedge; a view from the experimentalists. In Eiler, J., editor, *Inside the Subduction Factory*, volume 138 of *Geophysical Monograph*, pages 83–105. AGU.

Hirth, G. and Kohlstedt, D. L. (1996). Water in the oceanic upper mantle: implications for rheology, melt extraction and the evolution of the lithosphere. *Earth and Planetary Science Letters*, 144(1-2):93 – 108.

Kanamori, H. (1994). Mechanics of earthquakes. *Annu. Rev. Earth Planet. Sci.*, 22:207–237.

Kanamori, H. and Brodsky, E. (2004). The physics of earthquakes. *Reports on Progress in Physics*, 67:1429–1496.

Karato, S. (2011). Rheological structure of the mantle of a super-earth: Some insights from mineral physics. *Icarus*, 212(1):14–23.

Karato, S. and Wu, P. (1993). Rheology of the upper mantle - a synthesis. *Science*, 260(5109):771–778.

Karato, S., Zhang, S., and Wenk, H. (1995). Superplasticity in earth's lower mantle - evidence from seismic anisotropy and rock physics. *Science*, 270(5235):458–461.

Kattenhorn, S. A. and Prockter, L. M. (2014). Evidence for subduction in the ice shell of europa. *Nature Geoscience*, 7:762–767.

Kaula, W. M. (1994). The tectonics of venus. *Philosophical Transactions - Royal Society of London, Physical Sciences and Engineering*, 349(1690):345–355.

Kaus, B., Mulhaus, H., and May, D. (2010). Astabiliplumes algorithm for geodynamic numerical simulations with a free surface. *Phys. Earth. Planet. Int.*, 181:12–20.

Kemp, D. and Stevenson, D. (1996). A tensile flexural model for the initiation of subduction. *Geophys. J. Int.*, 125:73–96.

Khaleque, T. S., Fowler, A. C., Howell, P. D., and Vynnycky, M. (2015). Numerical studies of thermal convection with temperature- and pressure-dependent viscosity at extreme viscosity contrasts. *Phys. Fluids*, 27(7):–.

King, S. (2008). Pattern of lobate scarps on mercurys surface reproduced by a model of mantle convection. *Nature Geoscience*, 1:229–232.

King, S. (2009). On topography and geoid from 2-d stagant lid convection calculations. *Geochem. Geophys. Geosystems (G^3)*, 10(3).

Klimczak, C., Byrne, P. K., and Solomon, S. C. (2015). A rock-mechanical assessment of mercury's global tectonic fabric. *Earth and Planetary Science Letters*, 416:82 – 90.

Kohlstedt, D., Evans, B., and Mackwell, S. (1995). Strength of the lithosphere - constraints imposed by laboratory experiments. *J. Geophys. Res.*, 100(B9):17587–17602.

Korenaga, J. (2007). Thermal cracking and the deep hydration of oceanic lithosphere: A key to the generation of plate tectonics? *Journal of Geophysical Research-Solid Earth*, 112(B5).

Korenaga, J. (2009). Scaling of stagnant-lid convection with arrhenius rheology and the effects of mantle melting. *Geophys. J. Int.*, 179:54–170.

Korenaga, J. (2010a). On the likelihood of plate tectonics on super-earths: does size matter? *Astrophysical Journal Letters*, 725(1):L43–L46.

Korenaga, J. (2010b). Scaling of plate tectonic convection with pseudoplastic rheology. *J. Geophys. Res.*, 115.

Korenaga, J. (2013). Initiation and evolution of plate tectonics on earth: Theories and observations. *Annu. Rev. Earth Planet. Sci.*, 41(1):117–151.

Kramer, S., Wilson, C., and Davies, D. (2012). An implicit free surface algorithm for geodynamic simulations. *Phys. Earth. Planet. Int.*, 194-195:25–37.

Lammer, H., Bredehoeft, J. H., Coustenis, A., Khodachenko, M. L., Kaltenegger, L., Grasset, O., Prieur, D., Raulin, F., Ehrenfreund, P., Yamauchi, M., Wahlund, J. E., Griessmeier, J. M., Stangl, G., Cockell, C. S., Kulikov, Y. N., Grenfell, J. L., and Rauer, H. (2009). What makes a planet habitable? *Astronomy and Astrophysics Review*, 17(2):181–249.

Landuyt, W. and Bercovici, D. (2009). Variations in planetary convection via the effect of climate on damage. *Earth Planet. Sci. Lett.*, 277(1-2):29–37.

Landuyt, W., Bercovici, D., and Ricard, Y. (2008). Plate generation and two-phase damage theory in a model of mantle convection. *Geophysical Journal International*, 174(3):1065–1080.

Lenardic, A. and Crowley, J. W. (2012). On the notion of well-defined tectonic regime for terrestrial planets in this solar system and others. *ApJ*, 755:132.

Lithgow-Bertelloni, C. and Richards, M. (1995). Cenozoic plate driving forces. *Geophys. Res. Lett.*, 22(11):1317–1320.

Lu, G., Kaus, B. J., Zhao, L., and Zheng, T. (2015). Self-consistent subduction initiation induced by mantle flow. *Terra Nova*, 27(2):130–138.

Mackwell, S., Zimmerman, M., and Kohlstedt, D. (1998). High-temperature deformation of dry diabase with application to tectonics on venus. *Journal of Geophysical Research-Solid Earth*, 103(B1):975–984.

McGill, G. E., Stofan, E., and Smrekar, S. E. (2010). Venus tectonics. In Watters, T. R. and Schultz, R. A., editors, *Planetary tectonics*, pages 81–120. Cambridge University Press.

McKenzie, D. (1977). The initiation of trenches: A finite amplitude instability. In Talwani, M. and Pitman, W. I., editors, *Island Arcs, Deep Sea Trenches, and Back-Arc Basins, Maurice Ewing Series*, Maurice Ewing, pages 57–61.

McKinnon, W. B., Zahnle, K. J., Ivanov, B. A., and Melosh, H. J. (1997). Cratering on venus: Models and observations. In Bougher, S. W., Hunten, D. M., and Phillips, R. J., editors, *Venus II: Geology, Geophysics, Atmosphere, and Solar Wind Environment*, page 969.

Mei, S., Suzuki, A., Kohlstedt, D., N.A., D., and Durham, W. (2010). Experimental constraints on the strength of the lithospheric mantle. *J. Geophys. Res.*

Melosh, H. J. and McKinnon, W. B. (1988). The tectonics of mercury. In Vilas, F., Chapman, C. R., and Matthews, M. S., editors, *Mercury*, pages 374–400. University of Arizona Press.

Michel, N. C., Hauck, II, S. A., Solomon, S. C., Phillips, R. J., Roberts, J. H., and Zuber, M. T. (2013). Thermal evolution of mercury as constrained by messenger observations. *J. Geophys. Res.-Planets*, 118(5):1033–1044.

Miyagoshi, T., Kameyama, M., and Ogawa, M. (2015). Thermal convection and the convective regime diagram in super-earths. *Journal of Geophysical Research: Planets*, 120(7):1267–1278. 2015JE004793.

Miyagoshi, T., Tachinami, C., Kameyama, M., and Ogawa, M. (2014). On the vigor of mantle convection in super-earths. *Astrophysical Journal Letters*, 780(1):L8.

Moresi, L. and Solomatov, V. (1995). Numerical investigation of 2d convection with extremely large viscosity variations. *Physics of Fluids*, 7(9):2154–2162.

Moresi, L. and Solomatov, V. (1998). Mantle convection with a brittle lithosphere: thoughts on the global tectonic styles of the earth and venus. *Geophysical Journal International*, 133(3):669–682.

Morris, S. (1982). The effects of a strongly temperature-dependent viscosity on slow flow past a hot sphere. *J. Fluid Mech.*, 124:1–26.

Morris, S. and Canright, D. (1984). A boundary-layer analysis of benard convection in a fluid of strongly temperature-dependent viscosity. *Physics of the Earth and Planetary Interiors*, 36(SI):355–373.

Mueller, S. and Phillips, R. (1991). On the initiation of subduction. *Journal of Geophysical Research*, 96(B1):651–665.

Nikolaeva, K., Gerya, T., and Marques, F. O. (2010). Subduction initiation at passive margins: Numerical modeling. *J. Geophys. Res.*, 115:B03406.

Nimmo, F. (2000). Dike intrusion as a possible cause of linear martian magnetic anomalies. *Geology*, 28(5):391–394.

Nimmo, F. and Stevenson, D. (2000). Influence of early plate tectonics on the thermal evolution and magnetic field of mars. *J. Geophys. Res.*, 105(E5):11969–11979.

Ogawa, M. (1990). Perturbation analysis of convective instability of oceanic lithosphere and initiation of subduction zones. *J. Geophys. Res.*, 95(B1):409–420.

O'Neill, C., Jellinek, A. M., and Lenardic, A. (2007). Conditions for the onset of plate tectonics on terrestrial planets and moons. *Earth Planet. Sci. Lett.*, 261(1-2):20–32.

O'Neill, C. and Lenardic, A. (2007). Geological consequences of super-sized earths. *Geophys. Res. Lett.*, 34(19):L19204.

Orth, C. P. and Solomatov, V. S. (2012). Constraints on the venusian crustal thickness variations in the isostatic stagnant lid approximation. *Geochemistry, Geophysics, Geosystems*, 13:11. Q11012.

Padovan, S., Margot, J.-L., Hauck, S. A., Moore, W. B., and Solomon, S. C. (2014). The tides of mercury and possible implications for its interior structure. *Journal of Geophysical Research: Planets*, 119(4):850–866.

Parmentier, E. and Hess, P. (1992). Chemical differentiation of a convecting planetary interior - oonsequences for a one plate planet such as venus. *Geophysical Research Letters*, 19(20):2015–2018.

Parmentier, E. and Sotin, C. (2000). Three-dimensional numerical experiments on thermal convection in a very viscous fluid: Implications for the dynamics of a thermal boundary layer at high rayleigh number. *Phys. Fluids*, 12(3):609–617.

Peplowski, P. N., Evans, L. G., Hauck, S. A., McCoy, T. J., Boynton, W. V., Gillis-Davis, J. J., Ebel, D. S., Goldsten, J. O., Hamara, D. K., Lawrence, D. J., McNutt, R. L., Nittler, L. R., Solomon, S. C., Rhodes, E. A., Sprague, A. L., Starr, R. D., and Stockstill-Cahill, K. R. (2011). Radioactive elements on mercury's surface from messenger: Implications for the planet's formation and evolution. *Science*, 333(6051):1850–1852.

Phillips, R. (1994). Estimating lithospheric properties at alta-regio, venus. *Icarus*, 112(1):147–170.

Phillips, R. and Hansen, V. (1998). Geological evolution of venus: Rises, plains, plumes, and plateaus. *SCIENCE*, 279(5356):1492–1497.

Pruis, M. and Tanaka, K. (1995). The martian northern plains did not result from plate tectonics. In *26th Lunar and Planetary Science Conference*, page Abstract #1574, Houston. Lunar and Planetary Institute.

Ratcliff, J., Tackley, P., Schubert, G., and Zebib, A. (1997). Transitions in thermal convection with strongly variable viscosity. *Physics of the Earth and Planetary Interiors*, 102(3-4):201–212.

Redmond, H. L. and King, S. D. (2007). Does mantle convection currently exist on mercury? *Physics of the Earth and Planetary Interiors*, 164:221 – 231.

Reese, C., Solomatov, V., and Moresi, L. (1999). Non-newtonian stagnant lid convection and magmatic resurfacing on venus. *Icarus*, 139(1):67–80.

Reese, C. C., Solomatov, V. S., and Orth, C. P. (2007). Mechanisms for cessation of magmatic resurfacing on venus. *J. Geophys. Res.*, 112(E4).

Regenauer-Lieb, K., Hobbs, B., Yuen, D., Ord, A., Zhang, Y., Mulhaus, H., and Morra, G. (2006). From point defects to plate tectonic faults. *Philos. Mag.*, 86(21-22):3373–3392. Symposium on Instabilities Across the Scales, Cairns, Australia, SEP 14-17, 2004.

Regenauer-Lieb, K. and Kohl, T. (2003). Water solubility and diffusivity in olivine: its role in planetary tectonics. *Mineral. Mag.*, 67(4):697–715.

Regenauer-Lieb, K. and Yuen, D. (2004). Positive feedback of interacting ductile faults from coupling of equation of state, rheology and thermal-mechanics. *Physics of the Earth and Planetary Interiors*, 142(1-2):113–135.

Regenauer-Lieb, K., Yuen, D., and Branlund, J. (2001). The initiation of subduction: Criticality by addition of water? *Science*, 294(5542):578–580.

Richards, M., Yang, W., Baumgardner, J., and Bunge, H. (2001). Role of a low-viscosity zone in stabilizing plate tectonics: Implications for comparative terrestrial planetology. *Geochemistry Geophysics Geosystems*, 2:2000GC00043.

Richter, F. M. and McKenzie, D. P. (1981). On some consequences and possible causes of layered mantle convection. *Journal of Geophysical Research: Solid Earth*, 86(B7):6133–6142.

Ruiz, J. (2011). Giant impacts and the initiation of plate tectonics on terrestrial planets. *Planetary and Space Science*, 59(8):749 – 753.

Sandwell, D. and Schubert, G. (1992). Flexural ridges, trenches, and outer rises around coronae on venus. *J. Geophys. Res.*, 97(E10):16069–16083.

Schmeling, H., Babeyko, A., Enns, A., Faccenna, C., Funiciello, F., Gerya, T., Golabek, G., Grigull, S., Kaus, B., Morra, G., Schmalholz, S., and van Hunen, J. (2008). A benchmark comparison of spontaneous subduction models – towards a free surface. *Physics of the Earth and Planetary Interiors*, 171(1–4):198 – 223. Recent Advances in Computational Geodynamics: Theory, Numerics and Applications.

Schubert, G. and Sandwell, D. (1995). A global survey of possible subduction sites on venus. *Icarus*, 117(1):173–196.

Schubert, G., Solomatov, V., Tackley, P., and Turcotte, D. (1997). Mantle convection and the thermal evolution of venus. In Bougher, S., Hunten, D., and Phillips, R., editors, *Venus II*, pages 1245–1287. University of Arizona Press, Tucson.

Schubert, G., Turcotte, D. L., and Olson, P. (2001). *Mantle convection in the Earth and planets*. Mantle convection in the Earth and planets. Cambridge University Press, Cambridge, Cambridge, United Kingdom (GBR).

Shemenda, A. (1992). Horizontal lithosphere compression and subduction - constraints provided by physical modeling. *J. Geophys. Res.*, 97(B7):11097–11116.

Sleep, N. (1994). Martian plate-tectonics. *J. Geophys. Res.*, 99(E3):5639–5655.

Sleep, N. H. and Windley, B. F. (1982). Archean plate tectonics: constraints and inferences. *Journal of Geology*, 90:363–379.

Smith, D. E., Zuber, M. T., Phillips, R. J., Solomon, S. C., Hauck, S. A., Lemoine, F. G., Mazarico, E., Neumann, G. A., Peale, S. J., Margot, J.-L., Johnson, C. L., Torrence, M. H., Perry, M. E., Rowlands, D. D., Goossens, S., Head, J. W., and Taylor, A. H. (2012). Gravity field and internal structure of mercury from messenger. *Science*, 336(6078):214–217.

Smrekar, S. E., Hoogenboom, T., Stofan, E. R., and Martin, P. (2010). Gravity analysis of parga and hecate chasmata: Implications for rift and corona formation. *Journal of Geophysical Research: Planets*, 115(E7):n/a–n/a. E07010.

Solomatov, V. (1995). Scaling of temperature- and stress-dependent viscosity convection. *Phys. Fluids*, 7(2):266–274.

Solomatov, V. (2012). Localized subcritical convective cells in temperature-dependent viscosity fluids. *Physics of the Earth and Planetary Interiors*, 200-201:63–71.

Solomatov, V. and Moresi, L. (1996). Stagnant lid convection on venus. *Journal of Geophysical Research-Planets*, 101(E2):4737–4753.

Solomatov, V. and Moresi, L. (2000). Scaling of time-dependent stagnant lid convection: Application to small-scale convection on earth and other terrestrial planets. *Journal of Geophysical Research-Solid Earth*, 105(B9):21795–21817.

Solomatov, V. S. (2004a). Correction to initiation of subduction by small-scale convection. *Journal of Geophysical Research: Solid Earth*, 109(B5):n/a–n/a. B05408.

Solomatov, V. S. (2004b). Initiation of subduction by small-scale convection. *Journal of Geophysical Research: Solid Earth*, 109(B1):n/a–n/a. B01412.

Solomatov, V. S. (2015). The terrestrial magma ocean hypothesis. *Gondwana Research*, In press.

Stamenkovic, V. and Breuer, D. (2014). The tectonic mode of rocky planets: Part 1 – driving factors, models and parameters. *Icarus*, 234:174 – 193.

Stamenkovic, V., Breuer, D., and Spohn, T. (2011). Thermal and transport properties of mantle orck at high pressure: Applications to super-earths. *Icarus*, 216(2):572–596.

Stamenkovic, V., Noack, L., Breuer, D., and Spohn, T. (2012). The influence of pressure-dependent viscosity on the thermal evolution of super-earth. *ApJ*, 748:41.

Stegman, D., Richards, M., and Baumgardner, J. (2002). Effects of depth-dependent viscosity and plate motions on maintaining a relatively uniform mid-ocean ridge basalt reservoir in whole mantle flow. *Journal of Geophysical Research-Solid Earth*, 107(B6).

Stein, C., Finnenkotter, A., Lowman, J. P., and Hansen, U. (2011). The pressure-weakening effect in super-earths: Consequences of a decrease in lower mantle viscosity on surface dynamics. *Geophys. Res. Lett.*, 38:L21201.

Stein, C. and Hansen, U. (2008). Plate motions and the viscosity structure of the mantle - insights from numerical modelling. *Earth and Planetary Science Letters*, 272(1-2):29–40.

Stein, C. and Hansen, U. (2013). Arrhenius rheology versus frank-kamenetskii rheology – implications for mantle dynamics. *Geochemistry, Geophysics, Geosystems*, 14(8):2757–2770.

Stein, C., Schmalzl, J., and Hansen, U. (2004). The effect of rheological parameters on plate behaviour in a self-consistent model of mantle convection. *Physics of the Earth and Planetary Interiors*, 142(3-4):225–255.

Stern, R. (2004). Subduction initiation: spontaneous and induced. *Earth Planet. Sci. Lett.*, 226(3-4):275–292.

Stern, R. (2007). When and how did plate tectonics begin? theoretical and empirical considerations. *Chinese Science Bulletin*, 52(5):578–591.

Stern, R. J. and Bloomer, S. H. (1992). Subduction zone infancy: Examples from the eocene izu-bonin-mariana and jurassic california arcs. *Geological Society of America Bulletin*, 104(12):1621–1636.

Stofan, E. R., Brian, A. W., and Guest, J. E. (2005). Resurfacing styles and rates on venus: assessment of 18 venusian quadrangles. *Icarus*, 173(2):312 – 321.

Tachinami, C., Ogawa, M., and Kameyama, M. (2014). Thermal convection of compressible fluid in the mantle of super-earths. *Icarus*, 231:377 – 384.

Tackley, P., Ammann, M., Brodholt, J., Dobson, D., and Valencia, D. (2013). Mantle dynamics in super-earths: Post-perovskite rheology and self-regulation of viscosity. *Icarus*, 225(1):50 – 61.

Tackley, P. J. (2000a). Self-consistent generation of tectonic plates in time-dependent, three-dimensional mantle convection simulations 1. pseudoplastic yielding. *Geochemistry, Geophysics, Geosystems*, 1(8):n/a–n/a. 1021.

Tackley, P. J. (2000b). Self-consistent generation of tectonic plates in time-dependent, three-dimensional mantle convection simulations 2. strain weakening and asthenosphere. *Geochemistry, Geophysics, Geosystems*, 1(8):n/a–n/a. 1026.

Tosi, N., Grott, M., Plesa, A.-C., and Breuer, D. (2013). Thermochemical evolution of mercury's interior. *J. Geophys. Res.-Planets*, 118:2474–2487.

Toth, J. and Gurnis, M. (1998). Dynamics of subduction initiation at preexisting fault zones. *J. Geophys. Res.*, 103(B8):18053–18067.

Trompert, R. and Hansen, U. (1998). Mantle convection simulations with rheologies that generate plate-like behaviour. *Nature*, 395(6703):686–689.

Turcotte, D. (1977). Lithospheric instability. In Talwani, M. and Pitman, W. I., editors, *Island Arcs, Deep Sea Trenches, and Back-Arc Basins, Maurice Ewing Series*, Maurice Ewing, pages 63–69.

Turcotte, D. (1993). An episodic hypothesis for venusian tectonics. *J. Geophys. Res.*, 98(E9):17061–17068.

Turcotte, D. (1995). How does venus lose heat. *J. Geophys. Res.*, 100(E8):16931–16940.

Turcotte, D., Morein, G., Roberts, D., and Malamud, B. (1999). Catastrophic resurfacing and episodic subduction on venus. *Icarus*, 139(1):49–54.

Ueda, K., Gerya, T., and Sobolev, S. V. (2008). Subduction initiation by thermal-chemical plumes: Numerical studies. *Phys. Earth. Planet. Int.*, 171(1-4):296–312.

Valencia, D. and O'Connell, R. J. (2007). Inevitability of plate tectonics on super-earths. *ApJ*, 670:L45–L48.

Valencia, D. and O'Connell, R. J. (2009). Convection scaling and subduction on earth and super-earths. *Earth Planet. Sci. Lett.*, 286(3-4):492–502.

Valencia, D., O'Connell, R. J., and Sasselov, D. D. (2007). Inevitability of plate tectonics on super-earths. *Astrophysical Journal Letters*, 670(1):L45.

van Heck, H. and Tackley, P. (2011). Plate tectonics on super-earths: Equally or more likely than on earth. *Earth Planet Sci Lett*, 310:252–261.

van Hunen, J., Huang, J., and Zhong, S. (2003). The effect of shearing on the onset and vigor of small-scale convection in a newtonian rheology. *Geophysical Research Letters*, 30(19):n/a–n/a. 1991.

Wagner, F., Sohl, F., Hussmann, H., Grott, M., and Rauer, H. (2011). Interior structure models of solid exoplanets using material laws in the infinite pressure limit. *Icarus*, 214(2):366 – 376.

Watters, T. R., Selvans, M. M., Banks, M. E., Hauck, S. A., Becker, K. J., and Robinson, M. S. (2015). Distribution of large-scale contractional tectonic landforms on mercury: Implications for the origin of global stresses. *Geophys. Res. Lett.*, 42(10):3755–3763. 2015GL063570.

Watters, T. R., Solomon, S. C., Robinson, M. S., Head, J. W., Andre, S. L., Hauck, II, S. A., and Murchie, S. L. (2009). The tectonics of mercury: The view after messenger's first flyby. *Earth Planet. Sci. Lett.*, 285(3-4):283–296.

Weinstein, S. (1996). The potential role of non-newtonian rheology in the resurfacing of venus. *Geophys. Res. Lett.*, 23(5):511–514.

Weller, M. B. and Lenardic, A. (2012). Hysteresis in mantle convection: Plate tectonics systems. *Geophys. Res. Lett.*, 39:L10202.

Wong, T. and Solomatov, V. (2015). Towards scaling laws for subduction initiation on terrestrial planets: constraints from two-dimensional steady-state convection simulations. *Progress in Earth and Planetary Science*, 2(1):18.

Wong, T. and Solomatov, V. (In review). Variations in timing of plate tectonics initiation on terrestrial planets due to chaotic nature of mantle convection.

Yin, A. (2012). Structural analysis of the valles marineris fault zone; possible evidence for large-scale strike-slip faulting on mars. *Lithosphere*, 4(4):286–330.

Zhong, S. and Gurnis, M. (1996). Interaction of weak faults and non-newtonian rheology produces plate tectonics in a 3d model of mantle flow. *Nature*, 383(6597):245–247.

Zhong, S., Gurnis, M., and Moresi, L. (1996). Free-surface formulation of mantle convection-i. basic theory and application to plumes. *Geophys. J. Int.*, 127:708–718.

Zhong, S. and Watts, A. B. (2013). Lithospheric deformation induced by loading of the hawaiian islands and its implications for mantle rheology. *Journal of Geophysical Research: Solid Earth*, 118(11):6025–6048. 2013JB010408.